



Martin Thomas Horsch

Molecular dynamics simulation of heterogeneous systems

Scientific Report Series
Volume 19

Martin Thomas Horsch
Molecular Dynamics Simulation of Heterogeneous Systems
Scientific Report Series Volume 19
2016

Scientific Report Series
Laboratory of Engineering Thermodynamics (LTD)
University of Kaiserslautern
P.O. Box 3049
67653 Kaiserslautern
Germany

ISSN 2195-7606
ISBN 978-3-944433-18-9

© LTD all rights reserved

Molecular dynamics simulation of heterogeneous systems

Vom Fachbereich Maschinenbau und Verfahrenstechnik
der Technischen Universität Kaiserslautern
zur Erlangung der Lehrbefähigung für das Fachgebiet

Computational Engineering

genehmigte

Habilitationsschrift

von

Jun. Prof. Dr.-Ing. Martin Thomas Horsch
aus Stuttgart

Dekan: Prof. Dr.-Ing. Jörg Seewig
Gutachter: Prof. Dr.-Ing. Hans Hasse
Prof. Dr. Christian Holm (Universität Stuttgart)
Prof. Dr. George Jackson (Imperial College London)

Tag des Habilitationsvortrags: 29.06.2016

D 386

Science tiens à soudain accident.

François Villon

Acknowledgment

The work leading to the present habilitation has been conducted from 2011 to 2016 at the Laboratory of Engineering Thermodynamics (LTD) within the Department of Mechanical and Process Engineering of the University of Kaiserslautern. Since 2008, the LTD has been very successfully directed by Prof. Dr.-Ing. Hans Hasse who was a major guiding and inspiring force for this work. I also would like to thank Hans, as well as Prof. Dr. Christian Holm and Prof. Dr. George Jackson, for reviewing this thesis, and Prof. Dr.-Ing. Jan Aurich, Dr.-Ing. Mark Hlawitschka, and Prof. Dr.-Ing. Ralf Müller for joining the habilitation committee.

My sincere gratitude goes to Animesh Agarwal, Dr. Reinhold Bader, Stefan Becker, Dr.-Ing. Martin Bernreuther, Prof. Dr. Arndt Bode, Dr. Matthias Brehm, Dr. Martin Buchholz, Prof. Dr. Hans-Joachim Bungartz, Dr. Juan Castillo, Dr.-Ing. Stephan Deublein, Stefan Eckelsbach, Dr. Wolfgang Eckhardt, Dr. Colin Glass, Dr.-Ing. Gabriela Guevara, Dr. Nicolay Hammer, Dr. Alexander Heinecke, Dr. Herbert Huber, Prof. Dr. Karin Jacobs, Dr. Hans-Georg Kleinhenz, Mischa Klos, Andreas Köster, Dr. Sergey Lishchuk, Prof. Dr. Erich Müller, Christoph Niethammer, Dr.-Ing. Steffen Reiser, Dr.-Ing. Gábor Rutkai, Prof. Dr. Alexander Shchekin, Prof. Dr. Herbert Urbassek, Prof. Dr.-Ing. Jadran Vrabec, Amer Wafai, Stephan Werth, and Dr.-Ing. Thorsten Windmann, who are co-authors of publications collected in this work, and to Dr. Carlos Avendaño, Felix Diewald, Dr. Cemal Engin, Dr. Hendrik Frentrup, Dr. Edder García, Simon Geisert, Patrick Gralka, Michaela Heier, Nandit Jain, Dr. Peter Klein, Maximilian Kohns, Martin Lautenschläger, Patrick Leidecker, Dr. Nichola McCann, Dr. Guido Reina, Michael Schappals, Steffen Seckler, Prof. Dr. Jayant Singh, Dr. Rajat Srivastava, Simon Stephan, Dr.-Ing. Katrin Stöbener, and Martin Witzhausen for contributions to joint research, and I would like to acknowledge Dr.-Ing. Kai Langenbach for his valuable ideas.

A productive and collegial spirit has developed at the LTD, for which I thank all colleagues, particularly Jun. Prof. Dr.-Ing. Jakob Burger and Jun. Prof. Dr.-Ing. Erik von Harbou for their uncomplicated collaboration, and Jennifer Bergmann, Caro Hofmann, Monika Reim, and Ilona Stein, to whom we owe much of our success. This complements an environment consisting of IRTG 2057, SFB 926, SkaSim/TaLPas, and the BZS community, all with excellent partners. I also enjoyed the fruitful interactions with the CCP5 community. Finally, many thanks to my family and to all people who have supported me during the last few years.

Martin Horsch, Alsenbrück-Langmeil, August 2016

Abstract

Molecular simulation is a promising area of scientific computing.¹ While Monte Carlo methods are randomized and generate statistics over representative molecular configurations, molecular dynamics simulation follows the system trajectory, i.e. the temporal evolution, by numerically integrating the equations of motion. Relatively few molecules are sufficient to reproduce thermodynamic properties of homogeneous fluids, whereas a scale bridging approach is required for heterogeneous systems, e.g. for fluids at interfaces. The progress of simulation technology in high performance computing, concerning both the hardware and the simulation methods, has led to the emergence of Computational Molecular Engineering as an independent discipline of mathematical modelling and simulation that can deliver a significant contribution to scientific research in thermodynamics.

The state of the art in molecular modelling and simulation is commented and developed here with regard to applications in thermodynamics, where molecular methods have an inherent advantage over empirical correlations of the available data. By selecting a physical model which explicitly accounts for microscopic properties and intermolecular interactions, the choice of adequate model parameters facilitates both an accurate reproduction and a reliable prediction of real fluid properties. Furthermore, the molecular structure of the fluid at a phase boundary is resolved, so that it becomes possible to investigate interfacial phenomena in detail. In many cases, Computational Molecular Engineering yields the same level of accuracy as the underlying experimental data, which is the optimum that can be reached with theoretical methods.

This requires efficient and scalable simulation codes and simulation methods with a rigorous foundation in statistical mechanics. In Chapter 1, molecular methods are introduced and applied to heterogeneous systems. First, in Section 1.1, the present level of development of molecular force field methods is assessed from the point of view of simulation-based engineering, outlining the immediate perspective for further developments. Section 1.2 introduces molecular modelling and molecular dynamics simulation. On this basis, it is discussed how the vapour-liquid surface tension is defined and determined by molecular simulation (Section 1.3) and how the contribution from long-range interactions can be accurately and efficiently taken into account for systems with planar symmetry (Section 1.4).

¹Disclaimer: Large parts of the present work literally reproduce contents from journal articles that were published between 2011 and 2016.

Thermodynamic properties of dispersed phases are hard to measure, but nonetheless, they influence many technically relevant systems where they are present in stable dispersions or emerge as precursors of macroscopic phases. With scale bridging simulations, covering both small and large systems, it becomes possible to quantify how dispersed phases are influenced by their small size and their shape. This is discussed in Chapter 2, where an approach to the curvature dependence of the surface tension in terms of the excess equimolar radius, i.e. the deviation between two effective radii corresponding to a spherical interface, is introduced and applied to small droplets (Section 2.1). In Section 2.2, molecular simulations of thin liquid films are analysed to investigate size effects which are curvature-independent, and Section 2.3 considers bubbles in equilibrium with liquids at negative pressure.

Chapter 3 discusses phenomena at solid surfaces: In Section 3.1, molecular dynamics simulations are used for studying the contact angle of nanoscale sessile droplets on a planar solid wall, using the truncated and shifted Lennard-Jones potential. The entire range between total wetting and dewetting is investigated by varying the solid–fluid dispersive interaction energy, and a correlation is developed for the contact angle as a function of the dispersive interaction, the temperature and the solid density, which is also found to carry over to other similar systems. Self-assembled monolayers are investigated in Section 3.2 by simulating layers of alkylsilanes with different chain lengths, containing 12 and 18 carbon atoms, respectively, chemisorbed on a silica substrate. These simulations lead to conclusions on the relation between thickness, tilt angle, and coverage of the monolayers, which improve our understanding of experimental data, e.g. from electron density measurements. The interpretation of these experiments is often based on strongly simplified models, leading to errors which can be avoided by fruitfully combining experiment and simulation.

In Chapter 4, highly performant molecular simulation codes are presented which were released recently. The *ls1 mardyn* program, which is introduced in Section 4.1, has enabled the application of molecular force fields to length scales which were previously out of scope for molecular dynamics simulation. With dynamic load balancing, it delivers high scalability even for challenging heterogeneous configurations. Code optimizations tailored to the Intel Sandy Bridge processor are outlined in Section 4.2, including vectorization as well as shared-memory parallelization to make use of hyperthreading. On this basis, weak and strong scaling experiments are carried out for up to four trillion molecules on up to 146 016 cores on the SuperMUC cluster, achieving a parallel speedup of 133 000. While *ls1 mardyn* performs best for large heterogeneous systems, the thermodynamic analysis of small homogeneous systems poses different challenges which are addressed by the *ms2* program (Section 4.3).

Conclusions from these developments are formulated in Chapter 5. So far, only part of the way from basic research to systematic applications in fluid process engineering has been gone for scale bridging molecular modelling and simulation. However, it can already be recognized that it will pay off to go the remaining steps.

Zusammenfassung

Die molekulare Simulation ist ein vielversprechendes Gebiet des wissenschaftlichen Rechnens. Während Monte-Carlo-Methoden stochastisch vorgehen, verfolgt die Molekulardynamiksimulation die Trajektorie eines Systems, d.h. seine zeitliche Entwicklung, durch die numerische Integration der Bewegungsgleichungen. Verhältnismäßig wenige Moleküle genügen, um die thermodynamischen Eigenschaften homogener Fluide wiederzugeben, während für heterogene Systeme ein skalenübergreifender Ansatz erforderlich ist. Der Fortschritt der Simulationstechnik im Höchstleistungsrechnen, sowohl hinsichtlich der Hardware als auch der Simulationsmethoden, hat zur Entstehung des Computational Molecular Engineering als eigenständiger Disziplin der mathematischen Modellierung und Simulation geführt, die inzwischen einen wesentlichen Beitrag zur Forschung in der Thermodynamik leistet.

Der Stand der Technik der molekularen Modellierung und Simulation wird hier im Hinblick auf Anwendungen in der Thermodynamik kommentiert und entwickelt. Molekulare Methoden haben wesentliche Vorteile gegenüber empirischen Korrelationen: Indem ein physikalisches Modell vorgegeben wird, das mikroskopische Eigenschaften und intermolekulare Wechselwirkungen explizit berücksichtigt, ermöglicht die Wahl geeigneter Modellparameter sowohl die genaue Wiedergabe als auch die zuverlässige Vorhersage realer Stoffdaten. Zudem wird die molekulare Struktur des Fluids an einer Phasengrenze aufgelöst, sodass Grenzflächeneffekte detailliert untersucht werden können. In vielen Fällen erzielt Computational Molecular Engineering die gleiche Genauigkeit wie die den Stoffdaten zugrunde liegenden Experimente und erreicht somit die bestmögliche Übereinstimmung mit dem Realverhalten.

Dies erfordert effiziente und skalierbare Simulationsprogramme und robuste Simulationstechniken auf Grundlage der statistischen Mechanik. Kapitel 1 gibt eine Einführung in molekulare Methoden und ihre Anwendung auf heterogene Systeme. In Abschnitt 1.1 wird zunächst der aktuelle Stand der Entwicklung molekularer Kraftfelder vom Standpunkt der simulationsgestützten Ingenieurwissenschaften bewertet und eine Perspektive für weitere Entwicklungen skizziert. Eine Einführung in die molekulare Modellierung und die Molekulardynamik findet sich in Abschnitt 1.2. Im Anschluss daran wird diskutiert, wie die Oberflächenspannung zwischen Dampf- und Flüssigphase auf molekularer Ebene zu definieren und zu berechnen ist (Abschnitt 1.3) und wie der Beitrag langreichweiter Wechselwirkungen in planarsymmetrischen Systemen genau und effizient berücksichtigt werden kann (Abschnitt 1.4).

Die thermodynamischen Eigenschaften disperser Phasen sind schwer zu messen und dennoch von großer Bedeutung für viele Anwendungen, bei denen diese in stabilen Dispersionen oder als Vorläufer makroskopischer Phasen auftreten, die durch Nukleation entstehen (Tröpfchen und Gasblasen) oder sich durch dynamische Benetzung ausbreiten (dünne Filme). Durch skalenübergreifende Simulationen sowohl kleiner als auch großer Systeme kann genau ermittelt werden, wie die Größe und Form der dispersen Phasen ihre Eigenschaften beeinflusst. Dies wird in Kapitel 2 diskutiert, wo ein Ansatz vorgestellt und auf Tröpfchen angewandt wird, der die Krümmungsabhängigkeit der Oberflächenspannung über den Exzessäquimolarradius analysiert (Abschnitt 2.1). In Abschnitt 2.2 werden molekulare Simulationen dünner Filme ausgewertet, um krümmungsunabhängige Größeneffekte zu untersuchen, und Abschnitt 2.3 behandelt Gasblasen im Gleichgewicht mit Flüssigphasen bei negativem Druck.

Kapitel 3 befasst sich mit Phänomenen an Festkörperoberflächen. Abschnitt 3.1 untersucht den Kontaktwinkel von Tröpfchen auf ebenen Oberflächen. Hierbei wird das abgeschnittene Lennard-Jones-Potential eingesetzt, wobei die dispersive Wechselwirkungsenergie zwischen Festkörper und Fluid variiert wird. Für den Kontaktwinkel ergibt sich eine Korrelation, die sich auch auf andere ähnliche Systeme übertragen lässt. Durch die Simulation auf einem Siliziumoxidsubstrat chemisorbierter Alkylsilanschichten mit verschiedenen Alkylkettenlängen werden in Abschnitt 3.2 selbstorganisierte Monoschichten untersucht. Aus den Simulationen lassen sich Rückschlüsse über den Zusammenhang zwischen der Schichtdicke, der Orientierung der Substituenten und der Beladung des Substrats ziehen, die insbesondere zu einem besseren Verständnis von Elektronendichtemessungen führen können. Diese Experimente werden oft anhand stark vereinfachter Modelle ausgewertet, was zu Ungenauigkeiten führt, die durch eine Zusammenführung von Experiment und Simulation vermeidbar wären.

In Kapitel 4 werden zwei leistungsfähige Simulationscodes vorgestellt. Der Molekulardynamikcode *ls1 mardyn* (Abschnitt 4.1) hat es den molekularen Kraftfeldmethoden ermöglicht, zu bisher unerreichten Längenskalen vorzustoßen. Mit einem effizienten dynamischen Lastbalancierungsverfahren bleibt es selbst für komplexe und heterogene Szenarien hochskalierbar. Codeoptimierungen für den Sandy-Bridge-Prozessor von Intel, wie etwa die Vektorisierung und die Nutzung des Hyperthreading, werden in Abschnitt 4.2 dargestellt. Auf dieser Grundlage wurden auf dem SuperMUC-Cluster schwache und starke Skalierungsexperimente mit bis zu vier Billionen Teilchen und 141 016 Cores durchgeführt, in denen ein paralleler Speedup von 133 000 erreicht wurde. Während *ls1 mardyn* für große heterogene Systeme am leistungsfähigsten ist, stellt die thermodynamische Analyse kleiner homogener Systeme andere Anforderungen. Für diese wurde das Programm *ms2* entwickelt (Abschnitt 4.3).

Schlussfolgerungen aus diesen Entwicklungen werden in Kapitel 5 formuliert. Der Weg der skalenübergreifenden molekularen Simulation von der Grundlagenforschung bis hin zum systematischen Einsatz in der Fluidverfahrenstechnik ist erst zum Teil zurückgelegt. Es zeichnet sich aber bereits ab, dass es sich lohnen wird, ihn auch weiterhin zu beschreiten.

Contents

1	Introduction	3
1.1	The art of molecular modelling and simulation	3
1.2	Pair potentials and molecular dynamics	7
1.3	The vapour-liquid surface tension	13
1.4	Long-range corrections at planar interfaces	21
2	Finite-size effects for vapour-liquid interfaces	31
2.1	Excess equimolar radius of droplets	31
2.2	Finite thickness of liquid films	39
2.3	Density of dispersed gas bubbles	46
3	Fluids in contact with solid surfaces	57
3.1	Wetting of planar solid surfaces	57
3.2	Morphology of silane self-assembled monolayers	62
4	Scalable molecular simulation software	71
4.1	Large systems in molecular dynamics	71
4.2	Scalable multi-trillion molecule MD simulation	76
4.3	Molecular simulation of thermodynamic properties	84
5	Conclusion	93
	Literature	97

List of symbols

Latin		Greek	
A, \mathbf{A}	surface area	α	polarizability
\mathcal{A}	Helmholtz free energy	β	inverse temperature $\beta = 1/T$
a, b	adjustable parameters	Γ	adsorption or coverage
C	scaled curvature $C = \gamma/R_L$	γ	surface tension
D	dipole moment	$\bar{\gamma}$	effective surface tension
E	energy	δ	Tolman length
e	elementary charge	ϵ	energy parameter
f, \mathbf{f}	force	$\tilde{\epsilon}$	electric constant
G	Gibbs free energy	ζ	reduced interaction energy
g	radial distribution function	η	binary size parameter
H	enthalpy	Θ	interfacial entropy
\mathcal{H}	Hamiltonian	θ	contact angle or tilt angle
h	molar enthalpy	κ	electric conductivity
I, \mathbf{I}	moment or tensor of inertia	Λ	lattice constant
i, j, k	molecules, sites, or components	λ	thermal conductivity
J, \mathbf{J}	flux	μ	chemical potential
k, l	integer numbers or identifiers	$\tilde{\mu}$	normalized residual chemical potential
ℓ	elongation, length, thickness	ν	frequency
M, \mathbf{M}	rotational torque	Ξ	coordinate distortion
m	mass (of a molecule)	ξ	binary energy parameter
N, \mathbf{N}	number of molecules	ρ	density
\mathbb{N}	set of natural numbers	$\tilde{\rho}$	normalized density
n	number of countable objects	σ	size parameter
O	Landau «order of» symbol	τ	thermal critical scaling parameter
p	pressure	ν, χ	adjustable parameters
Q	quadrupole moment	Φ	Massieu potential
q	electric charge	ϕ	orientational angle or quaternion
R	radius	ψ	twist angle
r, \mathbf{r}	distance or radial coordinate	$\omega, \underline{\omega}$	angular velocity
S	entropy		

T	temperature
t	time
u	potential
V	volume
\mathbb{V}	set of linked cells in the vicinity
v, \mathbf{v}	velocity
W	average well depth
$x, y, z; \mathbf{x}$	Cartesian spatial coordinates
\mathcal{Z}	partition function

List of indices

Superscript		Subscript	
B	Bohr	B	Block
b	bins	c	critical
c	cutoff	e	equimolar
E	excess	f	fluid
e	electric	fw	fluid to wall
h	heat	L	Laplace
id	ideal	max	maximal
LJ	Lennard-Jones	min	minimal
LRC	long-range correction	n	normal
p	processes	p	pure
pot	potential	r	distance calculations
res	residual	s	site-to-site
s	saturation	t	tangential
t	tail	w	wall
		x, y, z	spatial directions
Σ	cumulative	δ	integration step
		κ	capillarity approximation
'	liquid phase	0	initial or zero-curvature value
''	vapour phase	1	unit or reference value
		∞	extrapolation to infinity

Abbreviations

ALU	arithmetic-logical unit
AoS	array of structures
AVX	advanced vector extensions
CC	constant curvature
C-C	centre of mass to centre of mass
COM	centre of mass
C-S	centre of mass to interaction site
DTS	dodecyltrichlorosilane
FIFO	first-in first-out
HPC	high performance computing
LJ	Lennard-Jones
LJTS	Lennard-Jones truncated and shifted
LRC	long-range correction
<i>ls1 mardyn</i>	<i>large systems 1: molecular dynamics</i>
MC	Monte Carlo
MD	molecular dynamics
MPI	message passing interface
<i>ms2</i>	<i>molecular simulation: second generation</i>
OTS	octadecyltrichlorosilane
RDF	radial distribution function
SAM	self-assembled monolayer
SoA	structure of arrays
S-S	interaction site to interaction site

1 Introduction

1.1 The art of molecular modelling and simulation

Molecular modelling and simulation is today an established discipline of simulation-based engineering as an application of high-performance computing. It adapts molecular force field methods, which emerged from the soft matter physics and thermodynamics communities [1], to the needs of industrial users in chemical and process engineering.¹ In recent years, highly accurate molecular models have been developed for a wide variety of fluids, and by massive parallelization, molecular simulations of complex nanoscopic systems (approaching the microscale) are feasible with a reasonable computational effort [3, 4].

We witness today the progress of molecular simulation from a set of theoretical academic methods to an arsenal of robust tools for practical use which supplement experimental data and replace experiments that are hazardous or hard to conduct [5]. This follows the general pattern by which engineering increasingly drives scientific development in areas originating from physics, building on substantial basic research efforts, as soon as they have become ripe for technical application.

The degree of sophistication of molecular force field methods and the complexity of the simulated systems varies considerably between the various fields of application. In particular, the interdependence of elementary thermodynamic properties such as pressure, density, temperature, enthalpy, and composition can be reliably investigated by simulating homogeneous systems that contain up to 1 000 molecules [1]. With relatively little additional effort, higher-order derivatives of the free energy (e.g. heat capacities or the speed of sound) are accessible as well [6]; the case is similar for mechanical properties of solid materials [7]. By Grand Equilibrium [8] or Gibbs ensemble simulation [9], vapour-liquid equilibria between homogeneous bulk phases, i.e. without an interface between them, can be efficiently and accurately sampled [5, 10]. Systems where a phase boundary is explicitly present can also be treated. Such simulations require more molecules, so that finite-size effects can be isolated [11], and longer computations (i.e. with more simulation steps) need to be carried out, since fluid interfaces often relax more slowly than the homogeneous bulk fluid and exhibit more significant

¹This section is based on Horsch *et al.* [2].

fluctuations, e.g. capillary waves, on a long time scale. A finite-size scaling analysis can help to capture the critical point and the critical exponents [12].

This facilitates a modelling approach that has been very fruitful in recent years: Thereby, the electrostatic features of a molecular model, i.e. the choice of parameters for point charges, dipoles or quadrupoles, are determined from quantum chemical calculations. United-atom sites interacting by the Lennard-Jones (LJ) potential are employed for the intermolecular repulsion as well as dispersive London forces [1], also known as van der Waals forces. The corresponding potential parameters are adjusted to optimize the overall agreement with experimental data [13]. These models account for the most important types of intermolecular interactions, including hydrogen bonding [4]. Furthermore, they can serve to explain molecular order in fluid systems (local concentrations, radial distribution functions, etc.). This distinguishes them from other approaches for describing fluid properties and explains why such models yield reliable extrapolations in two ways: First, to conditions far beyond those where the experimental data for the parameter fit were determined; second, to a wide variety of fluid properties which were not considered during parameterization at all [14].

Furthermore, transferable pair potentials are available which directly map functional groups to the model parameters of corresponding single-atom or united-atom interaction sites [15–17]. In this way, molecular simulation can deploy its predictive power, on the basis of a physically sound modelling approach, even where the available set of experimental data reaches its limits.

Both Monte Carlo (MC) and molecular dynamics (MD) simulation are suitable for determining most thermophysical properties: MC simulation evaluates an ensemble average by stochastically generating a representative set of configurations, i.e. position and momentum coordinates of the molecules. Thereby, MC simulation uses the Metropolis algorithm (which is randomized), whereas MD simulation computes a trajectory segment by integrating Newton's equations of motion (which are deterministic). If the same molecular force field is used, temporal and ensemble averaging lead to consistent results, since all thermodynamically relevant systems are at least quasi-ergodic [1]. MC simulation does not rely on time and does not require an explicit computation of momentum coordinates, which is advantageous for simulating adsorption [18] and phase equilibria [5]; in these and similar cases, the most effective methods involve grand-canonical or quasi-grand-canonical ensembles with a varying number of molecules [11, 18]. For such methods, where new molecules are inserted into the system, MD simulation has the disadvantage that momentum coordinates have to be determined without introducing an additional perturbation. For more complex properties, however, e.g. regarding non-equilibrium states and the associated relaxation processes, time-dependent phenomena become essential, so that MD is the preferred simulation approach (cf. Fig. 1.1).

Where pure component models are available, the extension to mixtures is straightforward. Combining rules can be used for predicting the unlike interaction parameters [20]. If suitable experimental data are available, adjustable binary parameters can be specified to improve

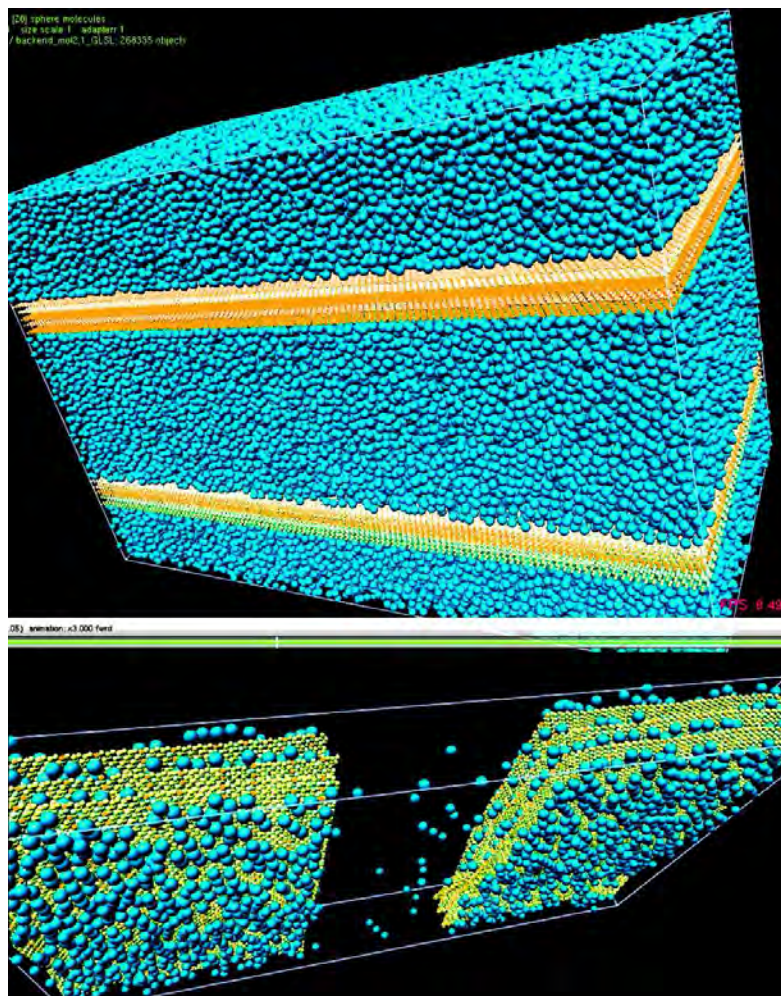


Figure 1.1: Top: MD simulation snapshot for Couette shear flow of methane in a graphite nanopore [19]. Bottom: Entrance effects, adsorption/desorption kinetics, and permeability of fluid methane in nanoporous carbon, employing non-equilibrium MD simulation [19]. The simulations were conducted with *ls1 mardyn*, cf. Section 4.1.

mixture models [20–22]. This concept can also be applied to modelling fluid-wall interactions, cf. Fig. 1.2 and Section 3.1.

Scientifically and technically, all preconditions for the introduction of molecular simulation in an industrial environment are now fulfilled [4]. Organizational aspects relevant for this process include institutional support, the active interest and involvement of both corporate and academic partners, and channelling of the effort to a few selected simulation codes which form a consistent toolkit. In this respect, the development in Great Britain can serve as a positive example, where a community centered around the *Computational Collaboration Project 5* develops and applies the programs *DL_POLY* [23, 24] and *DL_MONTE* [25]. An example for successful collaboration between academia and industry can be found in the United States, where the *Industrial Fluid Properties Simulation Challenge* also attracts international attention and participation [14]. However, the corresponding programming efforts are highly

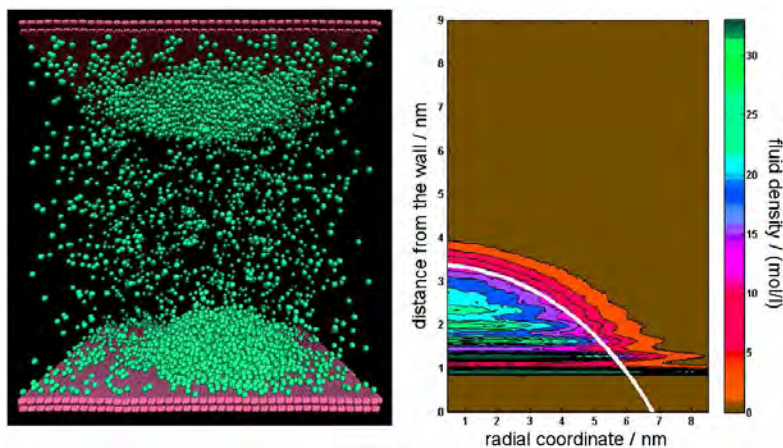


Figure 1.2: MD simulation snapshot (left) and average fluid density contour plot (right) for a sessile droplet on a solid substrate, cf. Section 3.1. The simulation was conducted with *ls1 mardyn*.

fragmented: Parallel developments are attempted based on the *Amber*, *CHARMM*, *LAMMPS*, *NAMD* and *MCCCS Towhee* codes, among many others [16, 26, 27].

In Germany, the strong orientation of the molecular thermodynamics community towards applications in chemical engineering guarantees an effective integration of engineering with high performance computing. It is within this framework that, beside other very successful codes like IMD [28, 29] and ESPResSo [30, 31], a software environment encompassing two major components is developed: The *ms2* program (molecular simulation: second generation), optimized for computing thermophysical properties of bulk fluids, and *ls1 mardyn* (large systems 1: molecular dynamics) for large and heterogeneous systems. These two codes, their functionality, and their performance are discussed in detail in Chapter 4.

From a computational point of view, large MC or MD simulations can better be tackled than MD simulations of processes over a relatively long time span. By far the largest part of the numerical effort is required for evaluating the force field, a task which can be efficiently distributed over multiple processes, as discussed above. In contrast, the temporal evolution along a trajectory through the phase space cannot be parallelized due to its inherently sequential nature. However, large and interesting systems generally also require more simulation time, not only more molecules. From the point of view of thermodynamics and fluid process engineering, the criterion for the computational progress in molecular simulation should not be the number of molecules N , but rather an exponent a such that e.g. within a single day, at least $N = 10^{3a}$ molecules in a condensed state were simulated over at least 10^{a+4} time steps. This would measure a proportional increase of the accessible length and time scales, which is what real applications require.

By pushing this frontier forward, a wide spectrum of novel scale-bridging simulation approaches will become feasible, paving the way to a rigorous investigation of many size-dependent effects, which on the microscale may be qualitatively different from the nanoscale.

Following this route, major breakthroughs will be reached within the coming decade, assuming that a research focus is placed on *processes at interfaces*. By focussing on such applications, cf. Fig. 1.1, an increase in the accessible length and time scale due to massively parallel high-performance computing will lead to particularly significant improvements, opening up both scientifically and technically highly interesting fields such as microfluidics (including turbulent flow), coupled heat and mass transfer, and design of functional surfaces to an investigation on the molecular level.

For industrial use in correlating and predicting homogeneous fluid properties, the development of integrated modelling and simulation frameworks for small systems, ensuring a short response time, is more promising and important than the simulation of large systems. On the other hand, many thermodynamic properties can also be reliably correlated and predicted with molecular equations of state, following the statistical associating fluid theory [32–35]. In combination with classical-mechanical density functional theory, this can even be extended to interfacial properties, at a far smaller computational cost than MC or MD simulation [36–39]. In this context, molecular simulation can best be used for validating the equation of state as well as its incorporation into density functional theory, and for the immediate vicinity of the critical point where scale-bridging simulations are required and the other approaches break down.

The present work discusses the state of the art of molecular modelling and simulation by high performance computing (HPC), highlighting recent contributions to this field and outlining future perspectives. The rest of Chapter 1 introduces fundamental concepts and methods to make the work self-contained. Sections 1.2 and 1.3 contain established material. However, the present brief introduction cannot and does not aim to replace classical textbooks, such as the statistical mechanics volume by Landau and Lifshitz [40], or the available compendia on molecular simulation methods such as the book by Allen and Tildesley [1]. In Section 1.4, a novel planar cutoff correction scheme is introduced. On this basis, subsequent chapters discuss MD simulation of vapour-liquid interfaces in nanosystems (Chapter 2), the contact of a fluid with a solid substrate (Chapter 3), and the highly performant molecular simulation codes *ls1 mardyn* and *ms2* (Chapter 4). Finally, a conclusion is given (Chapter 5), reflecting on the work of the recent years.

1.2 Pair potentials and molecular dynamics

Molecular modelling and simulation relies on a discrete representation of matter, i.e. each molecule is explicitly considered rather than smeared out as in continuum methods. The intermolecular interactions are treated by classical mechanics. Molecular thermodynamics thus occupies a middle position between quantum chemistry and computational fluid dynamics.

Continuum Mechanics	Molecular Simulation	Quantum Chemistry
Continuous matter and energy	Discrete matter, continuous energy	Discrete energy levels, particle-wave duality
Response to gradients (Fick, Fourier, Ohm, ...)	Interactions between molecules	Schrödinger equation
Transport coefficients	Classical-mechanical force field	Wave function

MD simulation can be employed to obtain transport coefficients and to parameterize the boundary conditions of continuum simulations. Conversely, molecular modelling often relies on quantum mechanical calculations, e.g. on the charge distribution within a molecule, for assistance during force-field parameterization.

Treating molecules as discrete classical-mechanical bodies, molecular thermodynamics thus considers the relationship between intermolecular interactions and the thermophysical behaviour of fluid systems [1]. Assuming pairwise additivity, the potential energy is given by a sum over pair potentials

$$E^{\text{pot}}(\mathbf{x}) = \sum_{k=1}^{N-1} \sum_{l=k+1}^N u_{ij}(r_{ij}, \phi_{ij}), \quad (1.1)$$

which depend on the distance between two molecules

$$r_{ij} = |\mathbf{x}_j - \mathbf{x}_i| \quad (1.2)$$

and in certain cases also on their mutual orientation ϕ_{ij} . For many purposes, it is sufficient to employ rigid models, which only consider external degrees of freedom, i.e. the translation and rotation of entire molecules. Following this approach, the vibration and rotation of covalent bonds within a single molecule is not modelled explicitly.

With a periodic boundary condition, a pseudo-infinite system is represented by a grid of identical, finite volumes, which are virtual copies of the microscopic box considered in a molecular simulation, cf. Fig. 1.3. According to the minimum image convention, the pair potential is only taken into account for the nearest periodic images of two molecules i and j .

Intermolecular interactions are by convention separated into short-range contributions, which decay fast in terms of the distance r_{ij} , and electrostatic long-range interactions, which follow Coulomb's law [41, 42]

$$u_{ij} = \frac{q_i q_j}{4\pi\tilde{\epsilon}r_{ij}}, \quad (1.3)$$

where q_i and q_j are two interacting electric charges and $\tilde{\epsilon} = 0.005\,526 \text{ eV } \text{Å}$ is the electric constant, i.e. the permittivity of a vacuum. For molecular simulations, atomic units based on

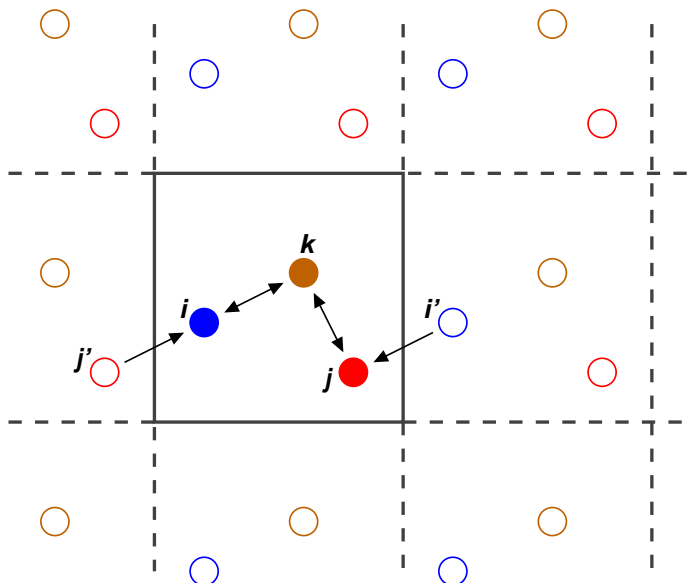


Figure 1.3: Illustration of the periodic boundary condition and the minimum image convention. In a molecular simulation following this approach, the interaction between the molecules i and j is not explicitly considered. Instead, i interacts with j' (periodic image of j), while j interacts with i' (periodic image of i), because they are closer.

the convention

$$\tilde{\epsilon} = \frac{1}{4\pi} \quad (1.4)$$

are usually employed to simplify the electrostatic terms. Higher-order electrostatic contributions are defined by the multipole expansion (charge, dipole, quadrupole, octopole, ...). In practice, however, only the lower-order multipole moments up to the quadrupole are actually considered, since the interaction due to higher-order moments decays very fast.

Short-range interactions also derive from the Coulomb equation. At very close intermolecular distances, these are predominantly repulsive. This is due to the interaction between the orbitals of neighbouring molecules

- by interpenetration, which increases E^{pot} due to a large local electron density, and
- by displacement, raising the two interacting orbitals to higher energy levels.

Furthermore, temporary and oscillating dipole moments are caused by fluctuations of the charge distribution, i.e. by dispersion. A first-order approximation, considering that temporary dipoles do not have a preferred orientation, cf. Fig. 1.4, does not yield any contribution of the dispersion to the potential energy.

If it is taken into account that energetically favourable orientations of two temporary dipoles towards each other are preferred, cf. Fig. 1.5, the dispersive interaction is found to be attractive

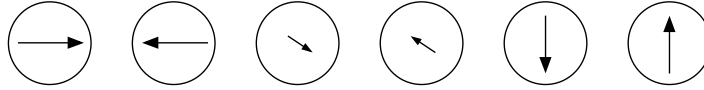


Figure 1.4: Opposite orientations of temporary dipoles caused by dispersion are equally probable.

due to the presence of induced dipoles. Following London [43], this contribution is given by

$$u_{ij}^{\text{disp}}(r_{ij}) = -\frac{3\alpha_i\alpha_j}{2(\nu_i^{-1} + \nu_j^{-1})} r_{ij}^{-6} + \mathcal{O}(r_{ij}^{-7}), \quad (1.5)$$

where α_i and α_j are the polarizabilities of the interacting molecules, characterized by the frequencies ν_i and ν_j , respectively.

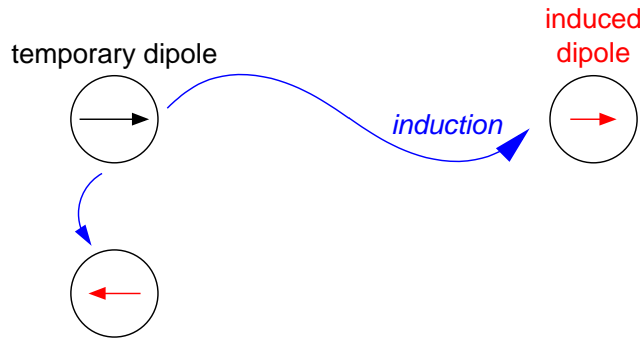


Figure 1.5: Temporary dipoles tend to induce a dipole moment with an energetically favourable orientation in neighbouring molecules. This causes the dispersive interaction to be attractive on average.

The LJ potential [44]

$$u_{ij}^{\text{LJ}}(r_{ij}) = 4\epsilon \left(\left[\frac{\sigma}{r_{ij}} \right]^{12} - \left[\frac{\sigma}{r_{ij}} \right]^6 \right), \quad (1.6)$$

with the size parameter σ and the energy parameter ϵ , contains both an attractive term, corresponding to the r^{-6} term of the dispersive interaction, cf. Eq. (1.5), as well as a repulsive term. It is a suitable model for the short-range pairwise interactions between fluid molecules. Two LJ interaction sites repulse each other for $r_{ij} < 2^{1/6} \sigma$, whereas for $r_{ij} > 2^{1/6} \sigma$, the LJ potential is predominantly attractive, cf. Fig. 1.6.

The molecular model for a mixture containing several components i, j, k, \dots , consists of pair potentials describing

- *like* interactions $i \leftrightarrow i, j \leftrightarrow j, k \leftrightarrow k, \dots$, i.e. interactions between equal molecules,
- and *unlike* interactions $i \leftrightarrow j, i \leftrightarrow k, j \leftrightarrow k, \dots$, between unlike molecules.

For point charges and multipoles, Coulomb's law applies to the unlike as it does to the like interaction, and a further parameterization to mixture properties is neither required nor desirable. For dispersion and repulsion, modelled by the LJ potential, various combining rules

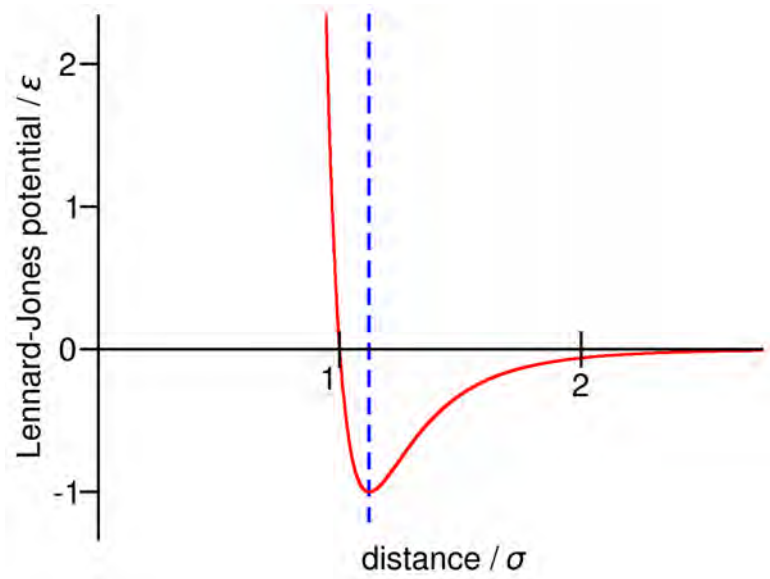


Figure 1.6: LJ potential (solid line) and distance $r = 2^{1/6} \sigma$ corresponding to the potential minimum (dashed line). Repulsive forces dominate left of the dashed line, and attractive forces due to dispersion dominate for larger distances between the interaction sites.

exist, none of which are strictly rigorous or universally valid [20]. However, the modified Lorentz combining rule for the size parameter

$$\sigma_{ij} = \frac{\eta}{2}(\sigma_i + \sigma_j) \quad (1.7)$$

and the modified Berthelot combining rule for the energy parameter

$$\epsilon_{ij} = \xi \sqrt{\epsilon_i \epsilon_j}, \quad (1.8)$$

can usually be employed with binary interaction parameters η and ξ close to 1. Following this approach, few experimental data for mixtures are sufficient to parameterize the unlike pair potential in a reliable way [21, 45].

For large numbers of molecules N it becomes computationally inefficient to evaluate Eq. (1.1) and related expressions by computing the entire sum over $N(N - 1)/2$ pairwise interactions. Instead, the near field is usually separated from the far field, and a cutoff radius r^c is introduced as an upper limit of the distances which are explicitly considered by pair potentials.

In the far field, the approximation of a continuous density distribution (e.g. constant density) can usually be justified. On this basis, interactions beyond the cutoff radius, i.e. with $r_{ij} \geq r^c$, are taken into account implicitly by a long-range correction (LRC). In a homogeneous system,² the LRC contribution of the LJ potential to the internal energy can thus be approximated

²The case of heterogeneous systems, e.g. at a phase boundary, is discussed in Section 1.4.

by

$$E^{\text{LRC}} = \frac{1}{2} \sum_{i=1}^N \int_{r^c}^{\infty} \rho u^{\text{LJ}}(r) 4\pi r^2 dr = -\frac{8\pi}{3} \frac{\epsilon \sigma^6}{[r^c]^3} \rho N + \mathcal{O}\left(\left[\frac{\sigma}{r^c}\right]^9\right). \quad (1.9)$$

Various approaches exist for computing the LRC for electrostatic interactions. In many cases, the reaction-field method [46, 47] can be employed, which assumes that the far field acts as a dielectric continuum, leading to relatively straightforward correction terms.

However, the reaction-field method breaks down in presence of an external electric field. Furthermore, it assumes that the near field is uncharged, which is not generally the case when ions are present. In such cases, e.g. for molecular simulation of electrolyte solutions, more elaborate correction schemes have to be used [48, 49]. These include several variants of Ewald summation based on the fast Fourier transform [50], such as particle-mesh Ewald [51, 52] and particle-particle particle-mesh Ewald summation, as well as the fast multipole method [53], which is carried out in Cartesian space rather than in Fourier space.

In a MD simulation, the trajectory of a system is followed by numerically integrating the classical-mechanical equations of motion, e.g. by the Verlet algorithm [54]

$$\begin{aligned} x_k(t + \Delta t) - x_k(t) &= x_k(t) - x_k(t - \Delta t) + \Delta t^2 \ddot{x}_k, \\ x_k(t + \Delta t) &= 2x_k(t) - x_k(t - \Delta t) - \frac{\Delta t^2}{m} \frac{\partial \mathcal{H}}{\partial x_k}. \end{aligned} \quad (1.10)$$

The acceleration

$$\ddot{x}_k = \frac{f_k}{m} = -\frac{\partial \mathcal{H}}{m \partial x_k} \quad (1.11)$$

is then given by the overall force f_k and the mass m associated with the respective degree of freedom k .

Following the leapfrog scheme, spatial coordinates and forces are computed at full time steps, whereas velocities and momenta are obtained at half time steps, i.e. in the middle of an integration interval. Accordingly, a time step is then given by an iteration of a loop containing the following operations:

1. Computation of positions $x_k(t) = x_k(t - \Delta t) + \Delta t \dot{x}_k(t - \Delta t/2)$,
2. Computation of forces $f_k(t) = -\partial \mathcal{H} / \partial x_k$,
3. Computation of velocities $\dot{x}_k(t + \Delta t/2) = \dot{x}_k(t - \Delta t/2) + \Delta t \ddot{x}_k(t)$.

For MD simulations including solids or dense liquids, an integration time step of $\Delta t \approx 1$ fs is usually chosen, but depending on the considered system, up to $\Delta t \approx 10$ fs can be viable for fluids. Beside the pair potentials and forces, the virial

$$\Pi = \sum_{i=1}^{N-1} \sum_{j=i+1}^N \Pi_{ij}, \quad (1.12)$$

is computed in a molecular simulation as a sum of pairwise contributions

$$\Pi_{ij} = -\mathbf{r}_{ij}\mathbf{f}_{ij} = -\frac{du_{ij}}{dr_{ij}} r_{ij}, \quad (1.13)$$

on the basis of the force exerted by the molecule j on the molecule i

$$\mathbf{f}_{ij} = \frac{du_{ij}}{dr_{ij}} \frac{\mathbf{r}_{ij}}{r_{ij}}, \quad (1.14)$$

in terms of the distance vector $\mathbf{r}_{ij} = \mathbf{x}_j - \mathbf{x}_i$. In the canonical, microcanonical, and grand canonical ensembles, the ensemble average $\langle \Pi \rangle$ of the virial is immediately related to the pressure

$$p = \rho T - \frac{1}{3V} \left\langle \sum_{\{i,j\}} r_{ij} \frac{du_{ij}}{dr_{ij}} \right\rangle = \rho T + \frac{\langle \Pi \rangle}{3V}. \quad (1.15)$$

Due to its relation to the mechanical pressure tensor, the virial can also be employed to compute the surface tension at a planar phase boundary, cf. Section 1.3.

1.3 The vapour-liquid surface tension

The tension of a planar fluid interface can be defined in different ways, following a thermodynamic or a mechanical approach.³ Thermodynamically, the surface tension γ can be expressed by the partial derivative of the free energy \mathcal{A} over the surface area A

$$\gamma = \left(\frac{\partial \mathcal{A}}{\partial A} \right)_{\mathbf{N}, V', V'', T}, \quad (1.16)$$

at constant number of molecules \mathbf{N} (of all components), constant volume V' and V'' of the coexisting phases, and constant temperature. By molecular simulation, the thermodynamic surface tension can be computed from the test area method [57], while grand canonical Monte Carlo simulation can be employed to obtain the excess Landau free energy corresponding to the respective density [58, 59].

For a mechanical definition, the surface tension is treated as causing a force f_t acting in tangential direction (with respect to the interface), i.e. a tendency of the interface to contract. The mechanical surface tension

$$\gamma = \frac{f_t}{\ell} \quad (1.17)$$

relates the magnitude of this force to the length of the contact line ℓ between the interface and the surface of a mechanical object, e.g. a confining wall, on which the force f_t acts.

³This section is based on the Introduction from Horsch *et al.* [55] as well as Section II from Horsch *et al.* [56].

In a cuboid box with the extension $V = \ell_x \times \ell_y \times \ell_z$, which contains a planar interface normal to the y axis, the interface and the two faces of the box which are normal to the x axis have contact lines with an elongation of ℓ_z , cf. Fig. 1.7. Each of these faces has an area of $A_{yz} = \ell_y \ell_z$. The tangential force $f_t = f_x = \gamma \ell_z$ constitutes a negative (contracting) contribution to the pressure, acting in tangential direction, i.e. in x -direction here.

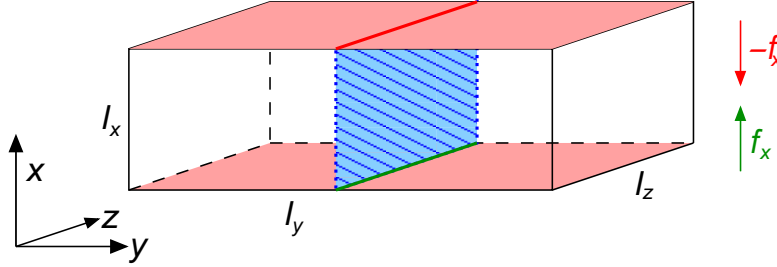


Figure 1.7: Diagram illustrating the mechanical definition of the surface tension. The two faces of the box with an orientation perpendicular to the x axis experience forces in opposite directions, expressing the tendency of an interface situated in the centre of the box to contract. The magnitude of the force f_x is proportional to the surface tension γ and the length of the contact line ℓ_z .

The surface tension can thus be obtained from the deviation between the tangential and normal eigenvalues p_t and p_n of the pressure tensor [60]

$$p_t - p_n = -\frac{\gamma \ell_z}{A_{yz}} = -\frac{\gamma}{\ell_y}. \quad (1.18)$$

In the example discussed above, the tangential pressure $p_t = p_x = p_y$ acts in the x and z directions parallel to the interface, while the normal pressure acts in y direction perpendicular to the interface. It is well known that for planar fluid phase boundaries, the thermodynamic and mechanical definitions of γ coincide [61]. In molecular simulations, where the pressure tensor is computed from the virial, an approach referred to as the virial route relies on Eq. (1.18) to obtain the surface tension [62, 63].

While the methodology for computing the vapour-liquid surface tension is both clear and simple in the case where a planar interface is simulated, the same problem becomes highly intricate for curved interfaces, i.e. for bubbles and droplets on the nanometre length scale. The methods available in the literature are all under dispute as regards their theoretical validity and accuracy. At a curved interface, moreover, the mechanical and thermodynamic surface tensions are not identical. Instead, the respective methods yield contradicting results, and for a virial route which is consistent with statistical mechanics, a second-order virial, based on the second derivative of the pair potential, needs to be introduced [64].

Furthermore, nano-scale liquid droplets or gas bubbles cannot be characterized sufficiently by a single effective radius. Instead, the Laplace radius R_L (also called «surface of tension»

radius) is distinct from the equimolar radius R_e , which is also known as the Gibbs adsorption radius. For a single-component droplet, the latter is defined by the zero excess density criterion

$$\int_0^{R_e} r^2 [\rho(r) - \rho'(\mu, T)] dr + \int_{R_e}^{\infty} r^2 [\rho(r) - \rho''(\mu, T)] dr = 0, \quad (1.19)$$

by comparing the radial density profile $\rho(r)$ with a step function based on the bulk liquid and vapour densities ρ' and ρ'' (as functions of μ and T). Therein, r denotes the distance from the centre of mass of the liquid droplet.

The Laplace radius is defined by the Laplace equation [65]

$$R_L = \frac{2\gamma}{\Delta p}, \quad (1.20)$$

in terms of the pressure difference Δp between both phases and the surface tension of the curved interface. This radius can be related to the surface area and the volume of the droplet

$$R_L dA = 2 dV. \quad (1.21)$$

Modified versions of the Laplace equation, which allow for the use of different effective radii in an analogous way, were developed by Buff [66, 67] and Kondo [68].

For spherical interfaces, the mechanical route to the surface tension is based on the Bakker-Buff equation [60, 67, 69, 70]

$$\gamma = R_L^{-2} \int_0^{\infty} [p_n(r) - p_t(r)] r^2 dr, \quad (1.22)$$

in terms of the normal component $p_n(r)$ and the two (equal) tangential components $p_t(r)$ of the diagonalized pressure tensor, where the integration starts from the centre of the droplet, i.e. from $r = 0$. This expresses the work required for a reversible isothermal deformation of the system that leads to an infinitesimal increase of the surface area at constant volume. It is sufficient to compute either the normal or the tangential pressure profile, since at a spherical interface, both are related by [70, 71]

$$\frac{dp_n}{d \ln r} = 2(p_t - p_n). \quad (1.23)$$

At mechanical equilibrium, Eq. (1.22) thus transforms to [70]

$$\gamma^3 = -\frac{\Delta p^2}{8} \int_{r=0}^{r=\infty} r^3 dp_n(r), \quad (1.24)$$

a term in which R_L no longer appears. The Laplace radius R_L can then be obtained from Eq. (1.20).

The most widespread implementation of this approach in terms of intermolecular pair potentials makes use of the Irving-Kirkwood (IK) pressure tensor [72], which was applied to spherical interfaces by Buff [67]. It underlies the simulation studies of Vrabec *et al.* [63] as well as those of van Giessen and Blokhuis [73]. The normal component of the IK pressure tensor is given by [70, 72]

$$p_n(r) = T\rho(r) + \sum_{\{i,j\} \in \mathbf{A}} -\frac{du_{ij}}{dr_{ij}} \frac{|\mathbf{r} \times \mathbf{r}_{ij}|}{4\pi r^3 r_{ij}}, \quad (1.25)$$

wherein \mathbf{A} contains all pairs of molecules i and j which are connected by a line that intersects the sphere of radius r around the centre of mass of the liquid droplet. The intersection coordinates (relative to the centre of mass) are represented by \mathbf{r} and the distance between the molecules by $\mathbf{r}_{ij} = \mathbf{x}_j - \mathbf{x}_i$, while du_{ij}/dr_{ij} is the force acting between i and j , cf. Eqs. (1.12) – (1.15).

However, several observations indicate that the accuracy of the mechanical route to the surface tension of curved interfaces may be limited:

- Irving and Kirkwood [72] originally proposed their expression for the special case of «a single component, single phase system». Its derivation relies on truncating an expansion in terms of derivatives of the pair density $\rho^{(2)}$ after the first term, thereby disregarding the density gradient completely. For a liquid droplet, this can lead to inaccuracies: «at a boundary or interface . . . neglecting terms beyond the first may not be justified» [72]. Nonetheless, Blokhuis and Bedeaux [74] have found that the IK tensor leads to the correct outcome for Δp (to third order in terms of equimolar curvature).
- By construction, the mechanical route cannot be separated from the assumption of a mechanical equilibrium, e.g. as expressed by Eqs. (1.22) to (1.24). For nanoscopic liquid droplets, however, the contribution to the partition function due to configurations that deviate from the equilibrium shape cannot be neglected, and it is not clear to what extent the spherical average of the pressure tensor succeeds in accounting for the free energy contribution of capillary waves, i.e. the excited vibrational modi of the interface [58, 75].
- The non-unique nature of the pressure tensor, which for a planar interface does not have a consequence on the computed value of the surface tension [62], leads to an inconsistent description for a curved interface [76–78]. The Harasima pressure tensor [69], where the set \mathbf{A} is defined differently and the tangential pressure profile $p_t(r)$ is computed instead of the normal component $p_n(r)$, has been found to agree rather well with the IK tensor [62, 63, 79]. However, as proven by Lau *et al.* [64], a second-order virial expression needs to be taken into account for spherically curved interfaces. Neither the IK pressure tensor nor others can therefore lead to an accurate outcome.

The test-area route to the surface tension is based on Bennett's [80] approach for molecular simulation of free energies and entropic quantities. In the canonical ensemble, the free energy difference $\Delta\mathcal{A} = \mathcal{A}_1 - \mathcal{A}_0$ between two states with equal N , V and T is given by the quotient of the respective canonical partition functions \mathcal{Z}_0 and \mathcal{Z}_1 , which can be evaluated from ensemble averages [80]

$$\exp\left(\frac{\Delta\mathcal{A}}{T}\right) = \frac{\mathcal{Z}_0}{\mathcal{Z}_1} = \frac{\langle \min(\exp(\Delta E/T), 1) \rangle_1}{\langle \min(\exp(-\Delta E/T), 1) \rangle_0}, \quad (1.26)$$

in terms of the internal energy difference $\Delta E = E_1 - E_0$. The index of the angular brackets denotes the system over which an ensemble average is taken. Bennett proposed the determination of these energy differences from «separately-generated samples» [80] for E_0 and E_1 . If the two systems differ in the area of a phase boundary, then the free energy difference can be related to the surface tension, assuming that all other deviations between them are accurately taken into account.

Gloor *et al.* [81] introduced a version of this approach where differences between the two states are obtained from a single simulation run for an unperturbed system with the partition function \mathcal{Z}_0 . Corresponding configurations of the second, perturbed system are generated by performing small affine transformations, keeping the volume and the number of molecules in both phases constant. In the limit of an infinitesimal distortion of the system, Eq. (1.26) can be simplified as [81, 82]

$$\frac{\Delta\mathcal{A}}{T} = -\ln \left\langle \exp\left(\frac{-\Delta E}{T}\right) \right\rangle_0, \quad (1.27)$$

as the probability distribution functions of the ensembles corresponding to the unperturbed and the perturbed system converge, so that a separate sampling is no longer required. A third-order expansion in the inverse temperature [82]

$$\frac{\Delta\mathcal{A}}{T} = \frac{\langle \Delta E \rangle}{T} - \frac{\langle \Delta E^2 \rangle - \langle \Delta E \rangle^2}{2T^2} + \frac{\langle \Delta E^3 \rangle - 3\langle \Delta E^2 \rangle \langle \Delta E \rangle + 2\langle \Delta E \rangle^3}{6T^3}, \quad (1.28)$$

can be used to increase the precision of the simulation results [64, 81, 83]. The surface tension is then immediately obtained from $\Delta\mathcal{A}/\Delta A$, since the distortion of the interface itself (as opposed to its increase in area) makes a negligible contribution to the free energy difference [84].

In the adaptation of the test-area method to curved interfaces developed by Sampayo *et al.* [83], an affine transformation scales one of the Cartesian axes by the factor $1/(1 + \varepsilon)$ and the remaining ones by $(1 + \varepsilon)^{1/2}$. For $\varepsilon > 0$, this creates an oblate shape and the area of the surface of tension is accordingly increased [85]. It can be shown that the first-order term in Eq. (1.28) is equivalent to the Kirkwood-Buff [86] mechanical route expression for the surface tension [87]. The higher-order terms therefore presumably capture the deviation between the mechanical and free-energy difference routes due to fluctuations or, equivalently,

the contribution of non-equilibrium configurations and the second-order virial to γ . Thus, the higher-order contribution to Eq. (1.28) may be related to the closed expression derived by Percus *et al.* [88] for the deviation between the grand potential and a volume integral over the local pressure.

From this point of view, the following aspects of the method merit further consideration:

- While finite differences of higher order are taken into account for the energy, no such terms are considered for the surface area here. Clearly, the variance of ΔE is partly caused by the variance of ΔA . The use of R_e for estimating ΔA may lead to further deviations.
- The variance of ΔE accounts for surface oscillations such as long wave-length capillary waves, which directly relate to equilibrium properties of the interface and therefore do not depend on the statistical-mechanical ensemble [77]. However, it can also be influenced by fluctuations regarding ρ' (at constant V') or V' (at constant ρ'). These modi are ensemble dependent, since they are coupled to the density of the vapour phase. Canonically, their amplitude increases with the total volume and is ill-defined in the thermodynamic limit $V \rightarrow \infty$. Therefore, the surface tension from the free-energy difference route may depend on the constraints imposed on the system by the ensemble.
- Although the volume associated with each of the phases is invariant for test-area transformations, there is still a distortion of the sample with respect to the equilibrium conformation. The method is therefore limited to isotropic phases, since shearing an anisotropic phase will induce an elastic contribution to $\Delta \mathcal{A}$ from the bulk region as well.

Following the approach of Gibbs [89], the Helmholtz free energy of a system containing two phases coexisting at an interface is decomposed into

$$\mathcal{A} = \mathcal{A}' + \mathcal{A}'' + \mathcal{A}^E, \quad (1.29)$$

where \mathcal{A}' is the free energy of the homogeneous bulk liquid with N' molecules, the volume V' , and the temperature T . Analogously, \mathcal{A}'' is the free energy of the homogeneous bulk vapour at N'' , V'' , and T . The excess term \mathcal{A}^E then describes the deviation of the free energy of the actual system, containing both phases and the interface, from sum of the free energies of the two homogeneous reference systems.

In this way, excess contributions are ascribed to the interface in all extensive quantities with the exception of the volume

$$V = V' + V'', \quad (1.30)$$

since in the Gibbs formalism, the dividing surface is assumed to be a strictly two-dimensional object without its own excess volume, i.e. $V^E = 0$. Neglecting interfacial adsorption as well

as finite-size effects on γ , the surface excess free energy is often approximated by

$$\mathcal{A}^E \approx \gamma A. \quad (1.31)$$

While such a simplification is justified for macroscopic systems, if an equimolar (zero-adsorption) dividing surface is used, this is not rigorous for small systems [90], where, in general, significant finite-size effects can be present even for planar phase boundaries [91]. The size dependence of the surface tension is further discussed in Chapter 2, proving that γ is far from constant for dispersed fluid phases. Nonetheless, thermodynamic relations containing interfacial excess quantities apply, even if the magnitude of these quantities may be size-dependent and hard to predict or to correlate phenomenologically.

Furthermore, since finite-size effects are much less pronounced for homogeneous than for heterogeneous systems, it can be assumed that general thermodynamic relations which do not include interfacial properties remain accurate for bulk fluid systems down to the nanoscale. This includes the following identity for the Gibbs free energy of a homogeneous system

$$G = \mathcal{A} + pV = \sum_i \mu_i N_i, \quad (1.32)$$

by which Eq. (1.29) transforms to

$$\mathcal{A} = \sum_i \mu_i (N'_i + N''_i) - p'V' - p''V'' + \mathcal{A}^E, \quad (1.33)$$

assuming that the two coexisting phases are in equilibrium thermally ($T' = T''$) and chemically ($\mu'_i = \mu''_i$). Therein, the first term can be rewritten as

$$\mu_i (N'_i + N''_i) = \mu_i (N_i - N_i^E), \quad (1.34)$$

for each component i , in terms of the surface excess number of molecules N_i^E , based on the identity

$$N_i = N'_i + N''_i + N_i^E. \quad (1.35)$$

By differentiation

$$\begin{aligned} d\mathcal{A} = & \sum_i \left[\mu_i (dN_i - dN_i^E) + (N_i - N_i^E) d\mu_i \right] \\ & - p' dV' - V' dp' - p'' dV'' - V'' dp'' + d\mathcal{A}^E, \end{aligned} \quad (1.36)$$

is then obtained, which can be compared with the total differential for \mathcal{A}

$$d\mathcal{A} = \sum_i \mu_i dN_i - p' dV' - p'' dV'' - S dT + \gamma dA, \quad (1.37)$$

as a function of \mathbf{N} , V' , V'' , T , and A , where S is the total entropy of the system. The subtraction (1.37) – (1.36) yields

$$0 = \sum_i \left[\mu_i dN_i^E + (N_i^E - N_i) d\mu_i \right] + V' dp' + V'' dp'' - S dT + \gamma dA - d\mathcal{A}^E \quad (1.38)$$

for the whole system, and

$$0 = - \sum_i N_i' d\mu_i + V' dp' - S' dT, \quad (1.39)$$

$$0 = - \sum_i N_i'' d\mu_i + V'' dp'' - S'' dT, \quad (1.40)$$

for the two homogeneous reference systems without an interface, where all surface excess terms are absent. By subtracting the reference systems from the whole system, i.e. (1.38) – (1.39) – (1.40), a general thermodynamic relation between the characteristic surface excess terms is obtained

$$0 = \sum_i \mu_i dN_i^E - S^E dT + \gamma dA - d\mathcal{A}^E, \quad (1.41)$$

where $S^E = S - S' - S''$ is the surface excess entropy. The excess free energy of the surface contains contributions of the adsorption and the surface tension

$$\mathcal{A}^E = \sum_i \mu_i N_i^E + \bar{\gamma} A, \quad (1.42)$$

$$d\mathcal{A}^E = \sum_i \left(\mu_i dN_i^E + N_i^E d\mu_i \right) + \bar{\gamma} dA + A d\bar{\gamma}, \quad (1.43)$$

which defines an effective tension $\bar{\gamma}$. Based on this decomposition, Eq. (1.41) transforms into a thermodynamically rigorous version of the Gibbs adsorption equation

$$A d\bar{\gamma} + (\bar{\gamma} - \gamma) dA = -S^E dT - \sum_i N_i^E d\mu_i, \quad (1.44)$$

which holds for arbitrary two-phase equilibria, even for dispersed phases on the nanometre length scale.

The effective tension $\bar{\gamma}$, defined by Eq. (1.42), may deviate from the thermodynamically accurate value of the surface tension γ , defined by Eq. (1.16). For macroscopic systems, based on the assumption $\bar{\gamma} \approx \gamma$, Eq. (1.44) can be simplified to [92]

$$d\gamma = -\Theta dT - \sum_i \Gamma_i d\mu_i \quad (1.45)$$

which is the better known form of the Gibbs adsorption equation. Therein, $\Theta = S^E/A$ is the interfacial entropy and $\Gamma_i = N_i^E/A$ is the adsorption of component i at the interface. This sim-

plified adsorption equation applies when finite-size effects on the surface tension are absent. In all other cases, the thermodynamically accurate adsorption equation must be employed, which is given by Eq. (1.44).

1.4 Long-range corrections at planar interfaces

In MD simulations, as discussed in Section 1.2, intermolecular interactions are usually evaluated explicitly up to a specified cutoff radius r^c , beyond which the interactions are covered by a LRC, following a mean-field approach [1, 17], which compensates the cutoff.⁴ In homogeneous simulations, the LRC is typically only considered for the energy and the virial [46, 94], while in inhomogeneous systems also the force has to be corrected appropriately [48, 95, 96]. If a small cutoff radius is used without a LRC, the surface tension and other thermodynamic properties are known to deviate significantly from the correct values [63, 97].

For homogeneous systems, typical correction strategies are straightforward, making the approximation that the radial distribution function (RDF) is unity beyond the cutoff radius. They may rely on a site-site correction [1] or on centre-of-mass (COM) correction approaches, employing angle averaging [98] or the reaction field method [47, 99]. For inhomogeneous configurations, fast multipole methods [53, 100], slab-based LRC [95, 101–103], mean M -body methods [104–106], or Ewald summation techniques [50, 107, 108] are used. Recent implementations of the slab-based and Ewald summation techniques yield very similar results for planar interfaces [95, 109].

In addition to the LRC approach, the cutoff scheme plays an important role. A site-site cutoff scheme consumes a much larger amount of computing time, because every site-site distance has to be evaluated and compared to the cutoff radius. Hence, a COM cutoff scheme should be generally preferred. However, the LRC has to be consistent with the chosen scheme [98, 110]. It is explained here how the slab-based LRC for inhomogeneous systems, which was introduced by Janeček [95], can be combined with the COM cutoff method by Lustig [98], which is based on angle averaging. Thereby, the potential energy of molecule i , given by

$$E_i^{\text{pot}} = \sum_{r_{ij} < r^c} u_{ij} + E_i^{\text{LRC}}, \quad (1.46)$$

is separated into an explicitly computed contribution and the LRC contribution. For systems with planar symmetry, such as a planar liquid film surrounded by vapour, it is sufficient to compute the LRC in terms of the coordinate normal to the interface, employing a slab-based approach [95, 103]. Here, the interface is assumed to be normal to the y axis. The correction

⁴This section is based on Werth *et al.* [93].

term E_i^{LRC} is then a sum over n^b slab-shaped bins with respect to the interactions between molecule i and the molecules from bin k

$$E_i^{\text{LRC}} = \sum_{k=1}^{n^b} E_{ik}^{\text{LRC}}. \quad (1.47)$$

Following Janeček [95], the correction term E_{ik}^{LRC} is obtained by integration over the bin volume

$$E_{ik}^{\text{LRC}} = 2\pi\rho(y_k)\Delta y \int_{r'}^{\infty} dr u(r) \sqrt{r^2 - r_{ik}^2}, \quad (1.48)$$

where Δy is the bin thickness, r_{ik} is the distance between the molecule i and the bin k , and $\rho(y_k)$ denotes the mean density within the bin k , cf. Fig. 1.8. As usual, it is assumed by Janeček [95] that within each of the slab-shaped bins, $g(r) \approx 1$ holds for the RDF beyond the cutoff radius.

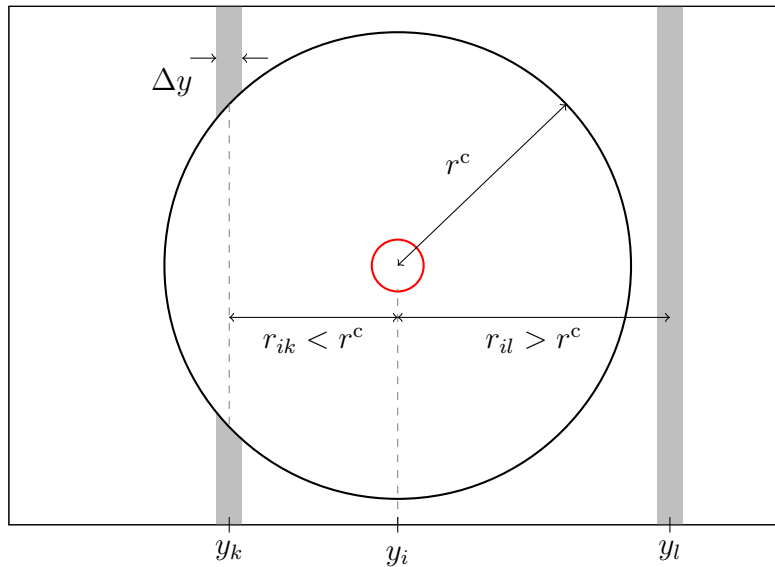


Figure 1.8: Relevant distances for the LRC approach by Janeček [95], cf. Eqs. (1.48) and (1.49).

As discussed by Siperstein *et al.* [111], the lower bound r' of the integration has to be selected appropriately, as shown in Fig. 1.8. If r_{ik} is smaller than the cutoff radius, r^c has to be used as the lower integration bound, otherwise it is r_{ik} [95, 111]

$$r' = \begin{cases} r_{ik}, & \text{if } r_{ik} > r^c, \\ r^c, & \text{otherwise.} \end{cases} \quad (1.49)$$

This definition of r' has to be employed in Eq. (1.48) as well as the analogous expressions for the force and the virial.

Janeček's approach yields results that are hardly dependent on the cutoff radius for the single-site LJ fluid, down to $r^c = 2.5 \sigma$ [95], cf. Section 2.2. It is also directly suitable for multi-site models if the molecular simulation code is based on a site-site cutoff scheme.

However, for molecules consisting of several LJ sites, a COM cutoff scheme is more efficient, because only the distances between the centres of mass have to be evaluated during the neighbourhood search. In this case, angle averaging as proposed by Lustig [98] is required for the LRC, because the orientation of the molecules cannot be considered explicitly by the LRC. The present study introduces such an approach and applies it to the LJ potential in terms of the distance r_s between two interaction sites, which may deviate from the distance r between the centres (of mass) of the molecules.

Three cases have to be distinguished here, cf. Fig. 1.9. For a given inter-centre distance r , only the centre-to-centre (C–C) distance is uniquely known, whereas the centre-to-site (C–S) and site-to-site (S–S) distances depend on the mutual orientation of the molecules. The term r_s thus has to be an average over all molecular orientations with the same C–C distance r [98].

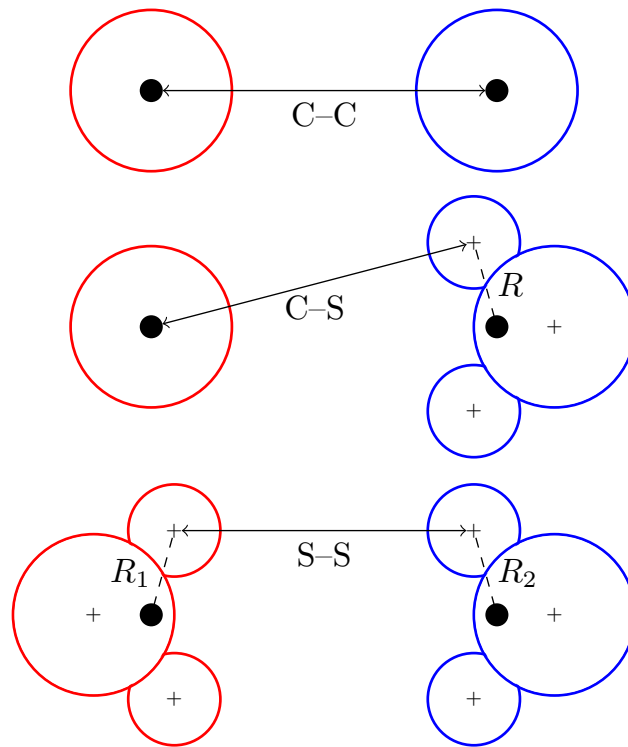


Figure 1.9: Illustration of the three different cases discussed here. Sites in the COM interact with each other by a C–C interaction (top), as opposed to the C–S interaction (middle) and the S–S interaction (bottom). The distance of the sites from the COM of their molecule is denoted by R . The dots indicate the COM, while the crosses denote the site positions.

In the C–C case, i.e. for the interaction between LJ sites superimposed with the molecular COM, the distance r_s is equal to the C–C distance r , and no angle averaging is required. For the C–C case, the reader is referred to Janeček [95] who derived correction terms for the potential energy, virial and force, following the approach outlined above. In the present section, Janeček’s approach is generalized such that the COM cutoff scheme can be applied to C–S and S–S interactions with a similar accuracy.

In the C–S case, one of the sites is not in the molecular COM, i.e. it is situated at a distance R from the COM. The C–S case does not exist on its own, because C–C and S–S interactions are also always present in such a scenario. The angle-averaged value of r_s^{-2l} , with $l \in \mathbb{N}$, is given by [98]

$$r_s^{-2l} = \frac{(r+R)^{2-2l} - (r-R)^{2-2l}}{4rR(1-l)}, \quad (1.50)$$

where $l = 3$ or 6 , respectively, for the dispersive or repulsive contributions to the LJ potential. The correction term for the potential energy is then a combination of Eqs. (1.48) and (1.50)

$$\begin{aligned} E_{ik}^{\text{LRC}} &= 2\pi\rho(y_k)\Delta y \int_{r'}^{\infty} 4\epsilon r \left[\sigma^{12} r_s^{-12} - \sigma^6 r_s^{-6} \right] dr \\ &= \frac{2\pi\epsilon\rho(y_k)\Delta y}{R} \int_{r'}^{\infty} \left[\frac{(r-R)^{-10} - (r+R)^{-10}}{5\sigma^{-12}} - \frac{(r-R)^{-4} - (r+R)^{-4}}{2\sigma^{-6}} \right] dr \\ &= \frac{2\pi\epsilon\rho(y_k)\Delta y\sigma^3}{3R} \left[\frac{(r'-R)^{-9} - (r'+R)^{-9}}{15\sigma^{-9}} - \frac{(r'-R)^{-3} - (r'+R)^{-3}}{2\sigma^{-3}} \right]. \end{aligned} \quad (1.51)$$

The correction term for the force is obtained in a similar manner

$$\begin{aligned} f_{ik}^{\text{LRC}} &= -2\pi\rho(y_k)\Delta y \int_{r'}^{\infty} \frac{\partial u}{\partial r_s} r_{ik} dr \\ &= \frac{2\pi\epsilon\rho(y_k)\Delta y\sigma^2 r_{ik}}{Rr'} \left[\frac{(r'-R)^{-10} - (r'+R)^{-10}}{5\sigma^{-10}} \right. \\ &\quad \left. - \frac{(r'-R)^{-4} - (r'+R)^{-4}}{2\sigma^{-4}} \right]. \end{aligned} \quad (1.52)$$

The correction term for the virial is separated into its normal and tangential contributions. The normal contribution (perpendicular to the interface) corresponds to the y direction here, and the tangential contribution corresponds to the x and z directions. The term for the virial in normal direction

$$\begin{aligned} \Pi_{ik,n}^{\text{LRC}} &= -\pi\rho(y_k)\Delta y \int_{r'}^{\infty} \frac{\partial u}{\partial r_s} r_{ik}^2 dr \\ &= \frac{\pi\epsilon\rho(y_k)\Delta y\sigma^2 r_{ik}^2}{Rr'} \left[\frac{(r'-R)^{-10} - (r'+R)^{-10}}{5\sigma^{-10}} \right. \\ &\quad \left. - \frac{(r'-R)^{-4} - (r'+R)^{-4}}{2\sigma^{-4}} \right], \end{aligned} \quad (1.53)$$

is analogous to the force, while the LRC expression for the tangential virial

$$\begin{aligned} \Pi_{ik,t}^{\text{LRC}} &= -\frac{1}{2}\pi\rho(y_k)\Delta y \int_{r'}^{\infty} \frac{\partial u}{\partial r_s} (r^2 - r_{ik}^2) dr \\ &= \frac{\pi\epsilon\rho(y_k)\Delta y\sigma^2}{2Rr'} \left[\frac{(r'-R)^{-10} - (r'+R)^{-10}}{5\sigma^{-10}} - \frac{(r'-R)^{-4} - (r'+R)^{-4}}{2\sigma^{-4}} \right] (r^2 - r_{ik}^2) \\ &\quad + \frac{\pi\epsilon\rho(y_k)\Delta y\sigma^3}{3R} \left[\frac{(r'-R)^{-9} - (r'+R)^{-9}}{15\sigma^{-9}} - \frac{(r'-R)^{-3} - (r'+R)^{-3}}{2\sigma^{-3}} \right], \end{aligned} \quad (1.54)$$

is slightly more complicated. In the S–S case, the correction terms are of similar form. Both sites are not in the COM of their molecule, i.e. they are separated from it by the distances R_1 and R_2 , respectively. The corresponding expression for r_s^{-2l} has also been derived by Lustig [98]

$$r_s^{-2l} = \frac{(r + R_+)^{3-2l} - (r + R_-)^{3-2l} - (r - R_-)^{3-2l} + (r - R_+)^{3-2l}}{8rR_1R_2(1-l)(3-2l)}, \quad (1.55)$$

with $R_+ = R_1 + R_2$ and $R_- = R_1 - R_2$. The correction terms for the potential energy and the force are calculated in the same way as for the C–S case

$$E_{ik}^{\text{LRC}} = \frac{\pi\epsilon\rho(y_k)\Delta y\sigma^4}{12R_1R_2} \left[\frac{(r' + R_+)^{-8} - (r' + R_-)^{-8} - (r' - R_-)^{-8} + (r' - R_+)^{-8}}{30\sigma^{-8}} - \frac{(r' + R_+)^{-2} - (r' + R_-)^{-2} - (r' - R_-)^{-2} + (r' - R_+)^{-2}}{\sigma^{-2}} \right], \quad (1.56)$$

$$f_{ik}^{\text{LRC}} = \frac{\pi\epsilon\rho(y_k)\Delta y\sigma^3 r_{ik}}{3R_1R_2 r'} \left[\frac{(r' + R_+)^{-9} - (r' + R_-)^{-9} - (r' - R_-)^{-9} + (r' - R_+)^{-9}}{15\sigma^{-9}} - \frac{(r' + R_+)^{-3} - (r' + R_-)^{-3} - (r' - R_-)^{-3} + (r' - R_+)^{-3}}{2\sigma^{-3}} \right], \quad (1.57)$$

and the LRC contribution to the normal virial in the C–S case is given by

$$\Pi_{ik,n}^{\text{LRC}} = \frac{\pi\epsilon\rho(y_k)\Delta y\sigma^3 \rho_{ik}^2}{6R_1R_2 r'} \left[\frac{(r' + R_+)^{-9} + (r' - R_+)^{-9}}{15\sigma^{-9}} - \frac{(r' + R_-)^{-9} + (r' - R_-)^{-9}}{15\sigma^{-9}} - \frac{(r' + R_+)^{-3} + (r' - R_+)^{-3}}{2\sigma^{-3}} + \frac{(r' + R_-)^{-3} + (r' - R_-)^{-3}}{2\sigma^{-3}} \right], \quad (1.58)$$

while the corresponding tangential expression is

$$\Pi_{ik,t}^{\text{LRC}} = \frac{\pi\epsilon\rho(y_k)\Delta y\sigma^3}{12R_1R_2 r'} \left[\frac{(r' + R_+)^{-9} + (r' - R_+)^{-9}}{15\sigma^{-9}} - \frac{(r' + R_-)^{-9} + (r' - R_-)^{-9}}{15\sigma^{-9}} - \frac{(r' + R_+)^{-3} + (r' - R_+)^{-3}}{2\sigma^{-3}} + \frac{(r' + R_-)^{-3} + (r' - R_-)^{-3}}{2\sigma^{-3}} \right] \left([r']^2 - r_{ik}^2 \right) + \frac{E_{ik}^{\text{LRC}}}{2}. \quad (1.59)$$

The corrections for the normal and tangential virial are used for the pressure calculation. The surface tension γ can be obtained from the deviation between the respective contributions Π_n and Π_t to the virial, which is equivalent to an integral over the differential pressure $p_n - p_t$

$$\gamma = \frac{1}{2A} (\Pi_n - \Pi_t) = \frac{1}{2} \int_{-\infty}^{\infty} (p_n - p_t) dy, \quad (1.60)$$

cf. Eq. (1.18), where $2A$ denotes the surface area of the two dividing surfaces [62, 95].

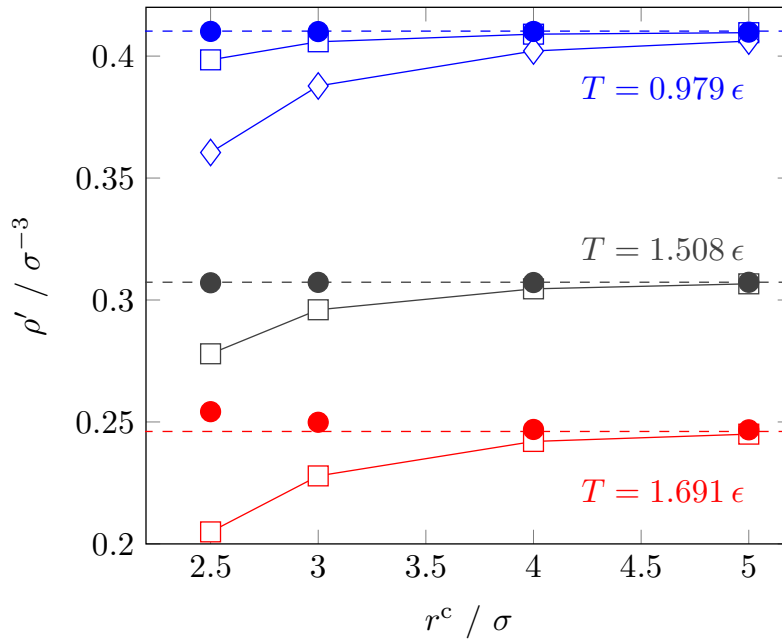


Figure 1.10: Saturated liquid density over the cutoff radius for the two-centre LJ model fluid. Comparison between simulations without LRC (diamonds), the site-based approach (squares), the present approach (bullets), and the reference values (dashed lines), cf. Stoll *et al.* [112].

The above correction terms were implemented in the molecular dynamics code *ls1 mardyn*, cf. Section 4.1. For an assessment of the present combination of the methods by Janeček [95] and Lustig [98], the two-centre LJ model fluid and literature models for two real fluids were considered: Carbon dioxide was described by the rigid three-site LJ model plus point quadrupole model of Merker *et al.* [113], and cyclohexane was modelled by six LJ interaction sites, also following Merker *et al.* [114]. Carbon dioxide is particularly relevant as a test case, since it combines C–C, C–S, and S–S interactions. The point quadrupole was assumed to have no preferred orientation beyond the cutoff radius, which yields a vanishing LRC contribution to all properties, including the potential energy.

The equations of motion were solved with a time step of $\Delta t = 0.001 \sigma \sqrt{m/\epsilon}$ for the two-centre LJ model fluid and $\Delta t = 1$ fs for CO₂ and cyclohexane, and the simulations were conducted in the canonical ensemble with $N = 16\,000$ molecules. The liquid phase was in the centre of the simulation volume, surrounded by vapour phases on both sides. The elongation of the simulation volume normal to the interface was between 60 and 80σ to limit the influence of finite size effects [115], which may be significant for thin liquid films, cf. Section 2.2. The thickness of the slab-shaped bins for the LRC computation was $\Delta y \approx 0.1 \sigma$ in all cases. The spatial extension of the simulation volume in the other directions was at least 20σ to properly account for the presence of capillary waves [116]. For scaling tests, the length of the simulation volume in y direction was varied. The equilibration was conducted for $200\,000$ time steps and the production runs for $800\,000$ time steps. The statistical errors were estimated

to be three times the standard deviation of four block averages, each over 200 000 time steps.

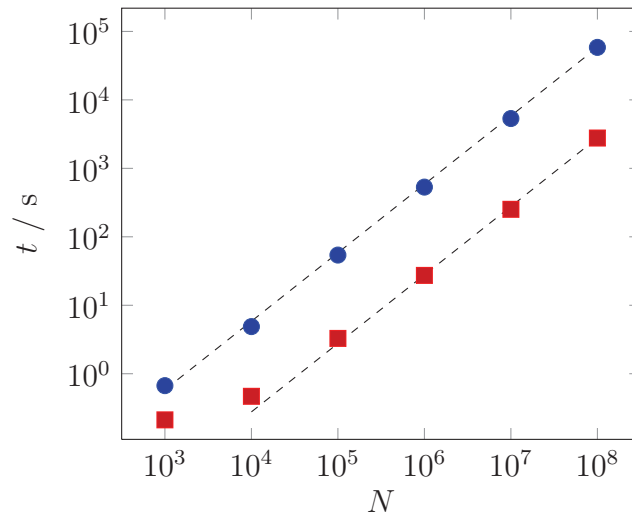


Figure 1.11: Computing time for 100 time steps with a single processing unit over the molecule number N . The bullets correspond to the computing time for the explicitly evaluated interactions. The computing time for the LRC (squares) is considerably smaller.

In Fig. 1.10, the results for the two-centre LJ model fluid are compared with data from Stoll *et al.* [112], who employed the Grand Equilibrium method, where interfaces are absent, with a cutoff radius of $r^c = 5\sigma$. In addition, simulation results without any LRC are included here, representing the extreme case where long-range interactions are completely neglected. To underline the necessity of angle averaging, Janeček’s original approach [110] was also applied here with a COM cutoff scheme (although it was designed for a site-site cutoff scheme) for purposes of comparing the numerical accuracy. This is referred to as the site-based approach in the following.

The results for the saturated liquid density that were determined with the present LRC approach hardly show any dependence on the cutoff radius for the lower two temperatures, while the site-based approach and the simulations without LRC show significant deviations from the reference saturated liquid density. Simulations without LRC were only performed for comparison near the triple point. At the highest temperature, both LRC approaches exhibit deviations from the reference case for small cutoff radii.

Furthermore, a simulation series on a single processing unit (Intel Xeon E5-2670) with a varying number of two-centre LJ molecules (elongation $\ell = \sigma$) was carried out. The chosen temperature ($T = 0.979\epsilon$) is close to the triple point of this fluid [112]. Figure 1.11 shows the computing time for 100 time steps in the canonical ensemble. Due to the underlying linked-cell algorithm [117], the computing time for the explicitly evaluated interactions scales almost perfectly with the molecule number N . Only for small systems ($N < 10\,000$), the LRC does not perfectly scale with the molecule number. However, even in this case, the computational

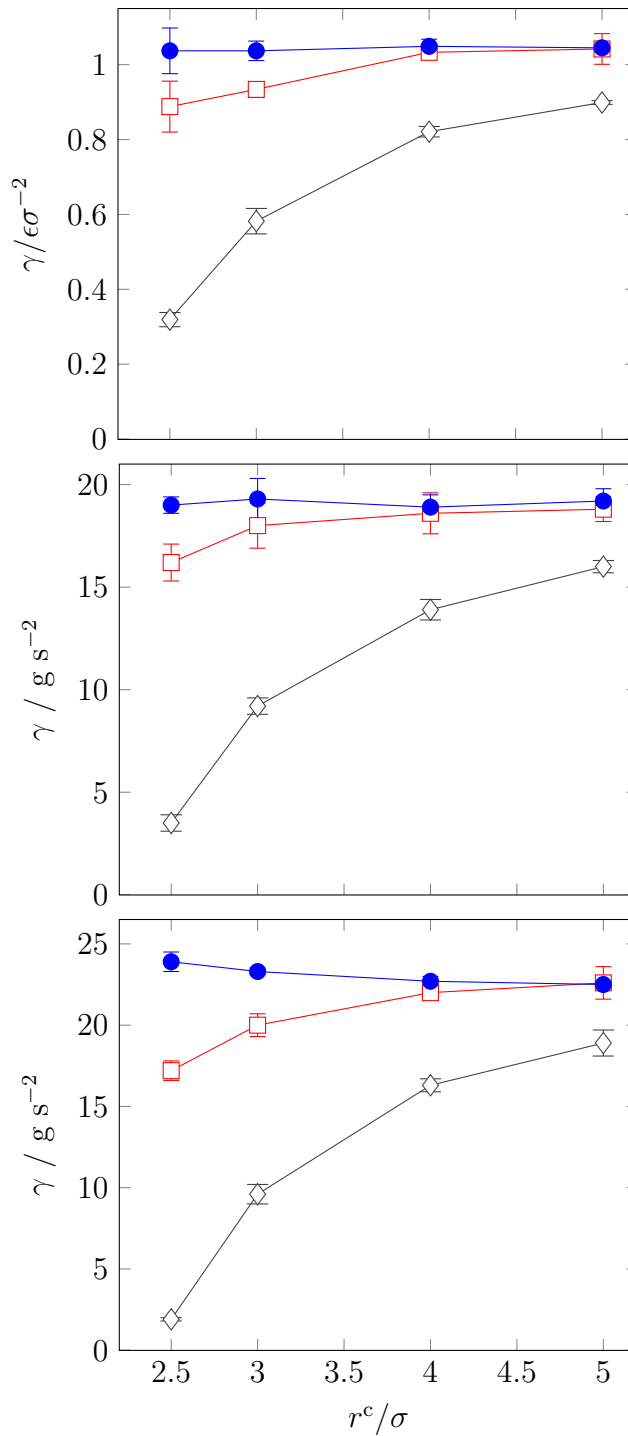


Figure 1.12: Surface tension over the cutoff radius for the two-centre LJ model fluid, carbon dioxide and cyclohexane. Comparison between simulations without LRC (diamonds), the site-based approach (squares) and the present approach (bullets). The temperature was $T = 0.979 \epsilon$ for the two-centre LJ model fluid (top), 220 K for carbon dioxide (centre) and 330 K for cyclohexane (bottom).

effort for the LRC is more than one order of magnitude smaller than that for the explicitly evaluated interactions.

For molecular modelling and simulation of fluids at interfaces, it is crucial to capture the vapour-liquid surface tension correctly. At the lowest temperature considered for each of the fluids, the surface tension was determined here by the three different approaches. Figure 1.12 shows the surface tension over the cutoff radius for the two-centre LJ model fluid as well as carbon dioxide and cyclohexane. The number of time steps was enlarged to four million to reduce statistical uncertainties and to better identify systematic deviations. Since cyclohexane is a much larger molecule than the others considered in this work, where all sites have a distance of approximately 0.52 to 0.54 σ from the molecular COM, a cutoff radius of 2.5 σ is insufficient. Nonetheless, even simulations with a cutoff radius of 3 σ yield a satisfactory level of accuracy. Only for a temperature of about 0.9 T_c , a larger cutoff needs to be specified to obtain the right value for the surface tension.

The present LRC approach thus yields very good results for saturated liquid density and the surface tension, showing only a weak dependence on the cutoff radius. It is numerically efficient, consumes only a small amount of computing time, and scales well for systems with very large numbers of molecules.

2 Finite-size effects for vapour-liquid interfaces

2.1 Excess equimolar radius of droplets

The macroscopic capillarity approximation consists in neglecting the curvature dependence of the surface tension γ of a spherical liquid droplet.¹ Accordingly, the surface tension of a curved interface in equilibrium is approximated by the value γ_0 in the zero-curvature limit, i.e. for a planar vapour-liquid interface. The Young-Laplace equation [65, 118] for spherical interfaces relates the macroscopic surface tension to a characteristic radius of the liquid droplet

$$R_\kappa = \frac{2\gamma_0}{p' - p''} = \frac{\gamma_0}{C}, \quad (2.1)$$

which will be referred to as the capillarity radius here; the notation $C = (p' - p'')/2$ for half of the difference between the liquid pressure p' and the vapour pressure p'' is introduced for convenience. Both the droplet radius and the pressure difference characterize the extent by which the surface is curved. The surface tension γ_0 of the planar vapour-liquid phase boundary, which is relatively easy to access experimentally, couples $1/R_\kappa$ and C , i.e. two measures of curvature, as a proportionality constant.

For curved interfaces in equilibrium, the chemical potential μ deviates from its saturated value $\mu^s(T)$ for a flat vapour-liquid interface at the same temperature T . In case of a droplet, both phases are supersaturated, cf. Section 1.3. In combination with an equation of state for the bulk fluid, microscopic properties such as the radius of a small liquid droplet can be deduced from the macroscopic state of the surrounding vapour, i.e. from its supersaturation ratio, and vice versa.

For nanodroplets, the deviation between the capillarity radius R_κ , cf. Eq. (2.1), the equimolar radius R_e , cf. Eq. (1.19), and the Laplace (surface of tension) radius R_L , cf. Eq. (1.20), cannot be simply neglected. As Tolman [84, 119, 120], following Gibbs, suggested on the basis of interfacial thermodynamics, one of these deviations, now commonly referred to as the Tolman

¹This section is based on Horsch *et al.* [56].

length

$$\delta = R_e - R_L, \quad (2.2)$$

characterizes the curvature dependence of the surface tension [120]

$$\frac{d \ln R_L}{d \ln \gamma} = 1 + \frac{1}{2} \left(\frac{\delta}{R_L} + \left[\frac{\delta}{R_L} \right]^2 + \frac{1}{3} \left[\frac{\delta}{R_L} \right]^3 \right)^{-1}. \quad (2.3)$$

This relation is often transformed into a polynomial expansion for γ_0/γ , which contains an infinite number of terms and has to be truncated, e.g. after the second-order contribution in terms of curvature [121]

$$\frac{\gamma_0}{\gamma} = 1 + \frac{2\delta_0}{R_L} + 2 \left(\frac{\ell_B}{R_L} \right)^2 + O(R_L^{-3}). \quad (2.4)$$

Here, δ_0 is the Tolman length in the limit of an infinite radius (i.e. zero curvature). The Block length ℓ_B characterizes the effect of Gaussian curvature [121, 122], which becomes predominant when δ_0 is very small or for systems where, due to an inherent symmetry, $\delta_0 = 0$ holds by construction. In practice, one of the major problems of the Tolman equation is that it analyses the surface tension in terms of the radii R_e and R_L , cf. Eqs. (1.19) and (1.20). While R_e can be immediately obtained from the density profile, R_L is by definition related to γ itself. If the surface tension of the curved interface is not known precisely, the surface of tension radius R_L is correspondingly uncertain.

To resolve this issue, Tolman's theory is reformulated here in terms of R_κ and R_e . This leads to greater transparency, since the capillarity radius R_κ can be obtained on the basis of the surface tension in the planar limit γ_0 , which is experimentally accessible, in combination with bulk fluid properties.² All information on the molecular structure of the curved interface can thus be captured by a single undisputed quantity here, namely the equimolar radius R_e . For this approach, the excess equimolar radius, defined by

$$R^E = R_e - R_\kappa, \quad (2.5)$$

plays a role similar to the Tolman length, and the macroscopic quantity C is used instead of R_L^{-1} as a measure of the influence of curvature on the thermophysical properties of the interface and the bulk phases. In this way, thermodynamics of liquid droplets is discussed by following a new route that relies on easily accessible properties only.

The present approach is similar to the «direct determination» of δ_0 proposed by Nijmeijer *et al.* [123], which was implemented by van Giessen and Blokhuis [73] on the basis of a

²The pressure difference between the coexisting phases in equilibrium is a bulk property, since it can be determined from μ and T with an equation of state for the fluid or by conducting grand canonical simulations.

representation of CR_e over $1/R_e$ with

$$-\delta_0 = \frac{1}{\gamma_0} \left(\lim_{R_e \rightarrow \infty} \frac{d}{d(1/R_e)} CR_e \right). \quad (2.6)$$

Applying the definitions of the capillarity radius and the excess equimolar radius, this transforms to

$$-\delta_0 = \lim_{R_e \rightarrow \infty} \frac{d(R_e/R_\kappa)}{d(1/R_e)} = \lim_{R_e \rightarrow \infty} \frac{d(R^E/R_\kappa)}{d(1/R_e)}, \quad (2.7)$$

facilitating an analysis of interface properties in terms of the radii R_κ and R_e as well as the deviation R^E between them. From the Tolman equation in its form as a polynomial expansion, cf. Eq. (2.4), the excess equimolar radius R^E can be related to the Tolman length δ by

$$R^E = (\delta + R_L) - R_\kappa = \delta + R_L \left(1 - \left[1 + \frac{2\delta_0}{R_L} + O(R_L^{-2}) \right] \right) = -\delta + O(R_L^{-1}), \quad (2.8)$$

so that its magnitude in the zero-curvature limit is obtained as

$$R_0^E = -\delta_0, \quad (2.9)$$

which expresses the same relationship as Eq. (2.7). Both in the planar limit and in the presence of curvature effects, it is therefore possible to rewrite the Tolman relations in terms of the easily accessible quantities R^E and C , rather than δ and R_L^{-1} . From the Young-Laplace equation, it follows that

$$\frac{dR_L}{dC} = \frac{1}{C} \frac{d\gamma}{dC} - \frac{\gamma}{C^2}, \quad (2.10)$$

while the reduced length scale appearing in the Tolman equation can be transformed to

$$\frac{\delta}{R_L} = \frac{R^E C + \gamma_0}{\gamma} - 1, \quad (2.11)$$

by using Eqs. (1.20), (2.1), (2.2) and (2.5). The full Tolman relation can be converted to

$$\frac{d\gamma}{dC} = -\frac{2\gamma}{C} \left(\frac{\delta}{R_L} + \left[\frac{\delta}{R_L} \right]^2 + \frac{1}{3} \left[\frac{\delta}{R_L} \right]^3 \right) = \frac{2\gamma}{3C} \left(1 - \left[\frac{R^E C + \gamma_0}{\gamma} \right]^3 \right). \quad (2.12)$$

This representation of the Tolman result is entirely equivalent to Eq. (2.3). For $C \rightarrow 0$, the curvature dependence of γ as specified by Eq. (2.12) is only self-consistent for

$$\lim_{C \rightarrow 0} \frac{dR^E}{dC} = -\frac{(R_0^E)^2}{\gamma_0}, \quad (2.13)$$

which thus constitutes a necessary boundary condition for the Tolman approach in terms of R^E and C . An expansion of the transformed Tolman equation as power series, analogous to

Eq. (2.4), is given by

$$\gamma = \gamma_0 + 2R_0^E C - \frac{2(R_0^E)^2}{\gamma_0} C^2 + \mathcal{O}(C^3). \quad (2.14)$$

Away from the planar limit, Eq. (2.12) applies without any further condition, since the boundary condition for the slope of R^E is only relevant for $C \rightarrow 0$.

Numerically, the LJTS model is an adequate basis for investigating bulk and interfacial properties of simple spherical conformal fluids (e.g. noble gases and methane) on the molecular level [63]. On account of this, numerous studies on nanoscopic liquid droplets have been reported [63, 121, 124, 125]. The LJTS fluid can thus be regarded as a key benchmark for theoretical and simulation approaches to the problem of curved vapour-liquid interfaces. To evaluate the present approach, the canonical ensemble is considered here for small systems, corresponding to equilibrium conditions for nanoscopic liquid droplets surrounded by super-saturated vapours, using the *lsI mardyn* program as well as the LJTS pair potential.

Liquid droplets are investigated at reduced temperatures between $T = 0.65$ and 0.95ϵ , covering most of the range between the triple point temperature (which is $\approx 0.55 \epsilon$ according to Bolhuis and Chandler [126], $\approx 0.618 \epsilon$ as determined by Toxværd [127] and $\approx 0.65 \epsilon$ according to van Meel *et al.* [124]) and the critical temperature which several independent studies have consistently obtained as 1.08ϵ for the LJTS fluid, cf. Vrabec *et al.* [63]. The Verlet leapfrog algorithm is employed to solve the classical equations of motion numerically with an integration time step of 0.002 in LJ time units, i.e. $\sigma \sqrt{m/\epsilon}$, where m is the mass of a molecule.

Cubic simulation volumes with 290 to 126 000 molecules, applying the periodic boundary condition, are equilibrated for at least 2 000 time units. Subsequently, spherically averaged density profiles $\rho(r)$, with their origin ($r = 0$) at the centre of mass of the whole system, are constructed with a binning scheme based on equal volume concentric spheres using sampling intervals between 1 000 and 40 000 time units, depending on the (expected) total simulation time, to gather multiple samples for each system. Examples of the density profiles obtained according to this method are shown in Fig. 2.1.

The density profiles of LJTS vapour-liquid interfaces are known to agree well with an expression based on two hyperbolic tangent terms, to which $\rho(r)$ has been successfully correlated for liquid droplets by Vrabec *et al.* [63]. The present method merely requires the bulk densities ρ' and ρ'' corresponding to a certain value of μ or C , which are determined here by correlating the outer parts of the density profile and extrapolating them to regions far from the interface. The densities of the coexisting fluid phases are thus deduced from simulation results by correlating the exponential terms

$$\begin{aligned} \rho' &= \rho(r) + a' \exp(b'[r - r']), \\ \rho'' &= \rho(r) - a'' \exp(b''[r'' - r]), \end{aligned} \quad (2.15)$$

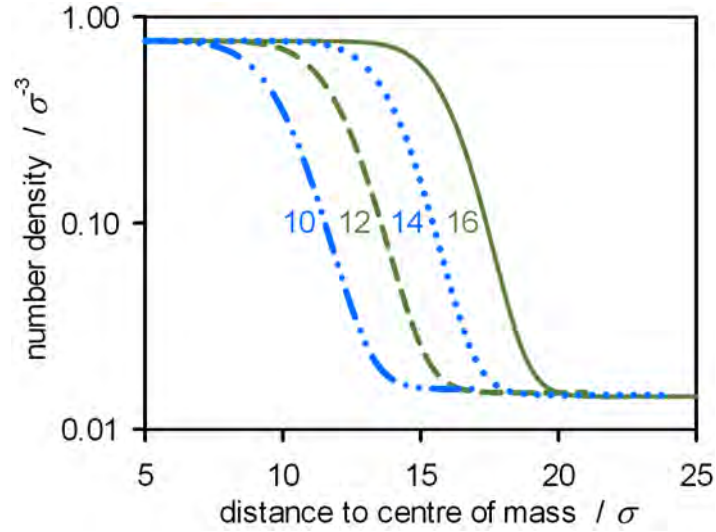


Figure 2.1: Density profiles from canonical MD simulations of LJTS liquid droplets at $T = 0.75 \epsilon$ with equimolar radii of $R_e = 9.977 \pm 0.001$ ($\cdot - \cdot$), 12.029 ± 0.003 ($- -$), $13.974 \pm 0.002 \sigma$ ($\cdot \cdot \cdot$) and $15.967 \pm 0.001 \sigma$ ($-$).

to the data for the inner- and outermost spherical bins of the density profiles, respectively, cf. Fig. 2.2. From the liquid and vapour densities ρ' and ρ'' of the fit to Eq. (2.15), the equimolar radius R_e is calculated according to Eq. (1.19). The respective margins of error are obtained as standard deviations from the profiles belonging to different sampling intervals of the same MD simulation, of which there are at least three in all cases. The corresponding pressures p' and p'' are computed by canonical MD simulation of the bulk fluid at the respective densities.

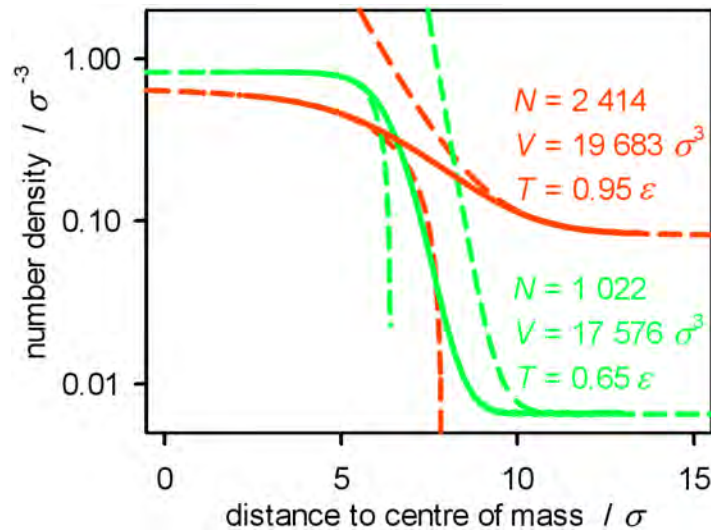


Figure 2.2: Density profiles from canonical MD simulations of LJTS liquid droplets at the temperatures $T = 0.65$ and 0.95ϵ , showing the average densities from simulation (\bullet) and exponential approximants ($- -$). The steeper profile corresponds to the lower temperature.

For the surface tension in the zero-curvature limit, as a function of temperature, the values

$$\begin{aligned}
 \gamma_0(0.65 \epsilon) &= (0.680 \pm 0.009) \epsilon \sigma^{-2}, \\
 \gamma_0(0.75 \epsilon) &= (0.493 \pm 0.008) \epsilon \sigma^{-2}, \\
 \gamma_0(0.85 \epsilon) &= (0.317 \pm 0.007) \epsilon \sigma^{-2}, \\
 \gamma_0(0.95 \epsilon) &= (0.158 \pm 0.006) \epsilon \sigma^{-2},
 \end{aligned} \tag{2.16}$$

are taken from the correlation of Vrabec *et al.* [63]; the error corresponds to the individual data points for γ_0 from the same source. In case of $T = 0.9 \epsilon$, the higher precision of the computations of van Giessen and Blokhuis [73] is exploited, using the value

$$\gamma_0(0.9 \epsilon) = (0.227 \pm 0.002) \epsilon \sigma^{-2}. \tag{2.17}$$

Combining these quantities leads to the capillarity radius R_κ and the excess equimolar radius R^E . A full summary of the simulation results where R^E could be determined with error bars smaller than 1σ is given in Tabs. 2.1 and 2.2. Thereby, the margin of error for R^E contains contributions due to the precision of γ_0 and the MD simulations of the liquid droplet itself as well as those of the homogeneous vapour and liquid phases.

To achieve full consistency with the Tolman approach, the bulk densities ρ' and ρ'' from Eq. (2.15) have to match those of the bulk fluid at the same temperature and chemical potential as the two-phase system. Regarding liquid droplets with $R_e > 8 \sigma$, this is certainly the case, since constant density regions coexisting with the interface are actually present, cf. Figure 2.1. The values determined for the smallest droplets here, however, rely on the validity of the correlation given by Eq. (2.15) and can be considered valid only as far as this expression itself does not introduce any major deviations.

Previous authors have made qualitatively contradictory claims on the magnitude of the Tolman length as well as its sign: Tolman himself expected δ to be positive and smaller than the length scale of the dispersive interaction [120], a conjecture that Kirkwood and Buff [86] affirmed, based on a mechanical approach. Subsequent studies, however, have also found δ to be negligible or even equal to zero [128, 129], positive and larger than σ [63, 130], or negative with $-\sigma < \delta < 0$ [83, 122, 131, 132], whereas others have claimed that the sign of δ is curvature dependent [133, 134]. Thereby, they have proven the mutual inconsistency of their assumptions and methods.

The present approach relies on the fact that $\delta_0 = -R_0^E$ holds in the planar limit. From the values for R^E reported in Table 2.2, for equimolar radii $R_e > 8 \sigma$, the excess equimolar radius for liquid is unequivocally shown to be smaller in magnitude than 0.5σ , while it remains unclear whether it is positive, negative, of both signs (depending on the curvature) or equal to zero. No definite conclusion can be drawn regarding the dependence of R^E on curvature.

N	$V [\sigma^3]$	$T [\epsilon]$	$\rho' [\sigma^{-3}]$	$\rho'' [\sigma^{-3}]$	$p' [\epsilon\sigma^{-3}]$	$p'' [\epsilon\sigma^{-3}]$
291	8 999	0.65	0.857(5)	0.0090(2)	0.65(8)	0.0054(1)
1 022	17 576	0.65	0.830(1)	0.00651(7)	0.22(2)	0.00397(4)
497	10 648	0.75	0.81(1)	0.0214(6)	0.6(1)	0.0135(4)
1 418	21 952	0.75	0.777(1)	0.0173(1)	0.16(1)	0.01136(5)
3 762	39 304	0.75	0.7721(2)	0.01566(6)	0.113(2)	0.01042(4)
5 161	54 872	0.75	0.7703(2)	0.0156(2)	0.096(3)	0.0104(1)
6 619	74 088	0.75	0.7697(2)	0.01506(4)	0.090(2)	0.01007(2)
10 241	110 592	0.75	0.7685(1)	0.01469(3)	0.080(2)	0.00985(2)
12 651	140 608	0.75	0.7679(2)	0.01451(7)	0.075(2)	0.00974(4)
15 237	166 375	0.75	0.7673(2)	0.01442(2)	0.070(2)	0.00969(1)
1 119	14 172	0.85	0.733(7)	0.0421(5)	0.23(5)	0.0273(2)
3 357	32 768	0.85	0.7135(8)	0.0371(5)	0.097(5)	0.0249(2)
2 031	21 952	0.9	0.687(3)	0.0573(8)	0.13(1)	0.0369(3)
4 273	29 791	0.9	0.6773(9)	0.0532(2)	0.082(4)	0.03516(7)
11 548	85 184	0.9	0.6738(1)	0.0504(2)	0.0672(6)	0.03396(8)
2 414	19 683	0.95	0.662(2)	0.0825(2)	0.169(7)	0.05032(8)

Table 2.1: Number of molecules N , simulation volume V , and temperature T of the present canonical simulations of LJTS liquid droplets surrounded by vapour, followed by the main immediate simulation results, i.e. the densities ρ' and ρ'' from the spherical density profiles. For droplet radii above 8σ , these values can be reliably regarded as identical with those corresponding to the present theoretical approach. In case of smaller radii, inaccuracies may be present due to the application of exponential approximants, cf. Eq. (2.15). Results from MD simulation of the bulk fluid were evaluated to obtain the corresponding pressures p' and p'' . All values are given in LJ units, and the error in terms of the last digit is specified in parentheses. The margin of error specified for the pressure values contains a contribution due to the uncertainty of the density.

Since this means that at the present level of accuracy, no significant dependence of γ on the radius of the liquid droplet could be detected, the statement of Mareschal *et al.* [135] regarding cylindrical interfaces also applies here: Considering «the large fluctuations in the bulk liquid phase, we tentatively conclude that the surface tension is independent of the curvature of the liquid-vapor interface or else that this dependence is very weak.»

For extremely small dispersed phases confined by a spherical interface, Wilhelmssen *et al.* [122] suggest (on the basis of a density gradient theory) that a «constant curvature (CC) region» exists, where the equimolar radius of the droplets (or bubbles) is almost constant, while the Laplace radius may vary significantly. In the CC region, the surface tension decreases (compared to larger nuclei and the planar interface), but this is not caused by any curvature effect at all, since the curvature is approximately constant. Instead, this change is driven by the density in the centre of the nucleus, which increasingly deviates from the bulk-like state and approaches the density of the surrounding phase. As Wilhelmssen *et al.* [122] point out, this might be an artifact of the density gradient theory, which is known to become inaccurate

N	$V [\sigma^3]$	$T [\epsilon]$	$R_\kappa [\sigma]$	$R_e [\sigma]$	$R^E [\sigma]$
291	8 999	0.65	2.1(3)	3.90(1)	1.8(3)
1 022	17 576	0.65	6.3(6)	6.407(2)	0.1(6)
497	10 648	0.75	1.8(5)	4.33(5)	2.5(5)
1 418	21 952	0.75	6.5(6)	6.883(3)	0.4(6)
3 762	39 304	0.75	9.7(4)	9.977(1)	0.3(4)
5 161	54 872	0.75	11.5(5)	11.089(4)	-0.5(6)
6 619	74 088	0.75	12.3(5)	12.029(3)	-0.2(5)
10 241	110 592	0.75	14.1(5)	13.974(2)	-0.1(5)
12 651	140 608	0.75	15.2(8)	14.981(6)	-0.2(8)
15 237	166 375	0.75	16.5(8)	15.967(1)	-0.5(8)
1 119	14 172	0.85	3.1(9)	6.79(6)	2.5(9)
3 357	32 768	0.85	8.8(8)	9.11(1)	0.4(9)
2 031	21 952	0.9	5.1(8)	6.79(6)	1.7(9)
4 273	29 791	0.9	9.7(9)	10.086(9)	0.4(9)
11 548	85 184	0.9	13.7(4)	14.054(8)	0.4(4)
2 414	19 683	0.95	2.7(3)	6.86(3)	4.2(3)

Table 2.2: Number of molecules N , simulation volume V , and temperature T of the present canonical simulations of LJTS liquid droplets surrounded by vapour, followed by the capillarity radius R_κ , the equimolar radius R_e and the excess equimolar radius R^E , determined from the simulation results given in Tab. 2.1. All values are given in LJ units, and the error in terms of the last digit is specified in parentheses.

in the spinodal limit. However, this might as well be a genuine observation, which would fit well into the general picture from recent work, cf. Sections 2.2 and 2.3.

A notion that can be definitely dismissed is that of a large and positive Tolman length, which has been obtained by following the mechanical route to the surface tension employing the IK pressure tensor [63, 130]. A similar deviation between the mechanical route (leading to large positive values for δ) and a thermodynamic approach (leading to $\delta < 0.5 \sigma$) was found by Haye and Bruin [136]. As Fig. 2.3 shows, the previous simulation results of Vrabec *et al.* [63] are actually consistent with those from the present study if they are interpreted in terms of the radii R_κ and R_e . Thereby, applying the approach of Maruyama *et al.* [137], only the density profile and the pressure in the homogeneous regions inside and outside the liquid droplet are taken into account, whereas the normal pressure along the interface is not considered at all.

Since the deviation between present and previous data disappears in such a representation, the disagreement must be caused by the inadequacy of the pressure-tensor (mechanical) route, as pointed out by Henderson [77]. Possible sources of error for this approach are discussed in Section 1.3. More detailed methodological investigations have also been carried out by Lau *et al.* [64], suggesting that a rigorous mechanical route to γ would need to take a contribution of the second-order virial into account.

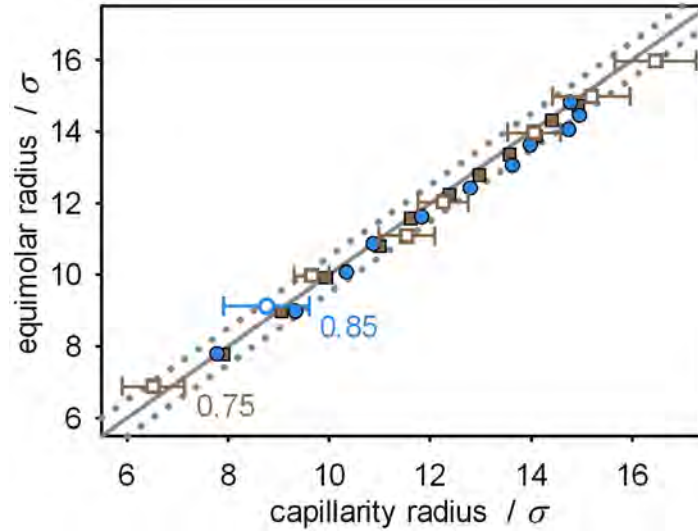


Figure 2.3: Equimolar radius R_e over the capillarity radius R_k for LJTS liquid droplets, from density profiles and bulk pressures determined with canonical MD simulations at the temperatures $T = 0.75$ (\square) and 0.85 (\circ), in comparison with results from previous work of Vrabec *et al.* [63] at $T = 0.75$ (\blacksquare) and 0.85 (\bullet), using pressure differences based on evaluating the Irving-Kirkwood pressure tensor in the homogeneous regions inside and outside the liquid droplet. The continuous diagonal line is defined by $R_e = R_k$ and thus corresponds to an excess equimolar radius of $R^E = 0$, while the dotted lines correspond to $R^E = \pm 0.5 \sigma$.

2.2 Finite thickness of liquid films

For a fluid interface, there are at least three different aspects in which its size can be varied, each of which may affect the interfacial tension:

- Curvature effects, depending on the local characteristic radii of curvature,
- capillary wave effects, depending on the range of wavelengths permitted by the morphology and size of the interface,
- confinement effects, which arise due to spatial restrictions imposed on a fluid phase by one or several interfaces or walls.³

According to Tolman's approach [120], cf. Section 2.1, the interfacial tension of a nanodroplet deviates from that of a planar interface due to its extremely curved shape [136, 139]. However, it should be noted that all three phenomena are present when the size of a droplet is varied: Smaller droplets have a higher curvature, a smaller range of capillary wavelengths, and a more significant deviation from bulk-like behaviour due to confinement. In addition to curvature, the other effects might therefore also have a significant influence on the formation of droplets in a supersaturated vapour [140, 141]. A similar case is cavitation, where bubbles emerge in a liquid phase [142].

³This section is based on Werth *et al.* [138].

Spherically curved interfaces of droplets were already investigated by molecular simulation in the early 1970s [143]. Nonetheless, while curvature effects are relatively well-studied, the other size effects have not received the same attention, even though they are even present in the case of planar interfaces. Several previous works address the influence of small simulation volumes [116, 144], which is usually discussed in terms of capillary wave theory [116, 145]. The present study considers the influence of the liquid film thickness, due to confinement of the liquid phase by two parallel planar vapour-liquid interfaces which are close to each other. This effect was previously investigated by Weng *et al.* [146], who did not find any systematic influence of the film thickness.

The computation of interfacial properties is always done in a single simulation volume containing both phases, the liquid and the vapour phase, separated by the interface. Thereby, the surface tension can be computed for example via the virial route or via the surface free energy [70, 147, 148], cf. Section 1.3. The virial route is directly related to the common approach for calculating the pressure in a molecular simulation [135, 149], and it is known that the pressure in dependence of the density exhibits a van der Waals loop in the two phase region [150].

At interfaces, the long-range contribution to the interaction potential plays an important role for all thermodynamic properties [151]. Nonetheless, there are also simulations applying a truncated and shifted potential, which neglects the long-range contribution entirely [73, 126]. When dealing with a homogeneous system, long-range corrections are only needed for energy and pressure [94], while in an inhomogeneous configuration, also the dynamics of the systems needs to be appropriately corrected [95, 101], cf. Section 1.4, unless a truncated potential is used.

In the present section, the influence of the liquid film thickness on thermodynamic properties is discussed. For this purpose, MD simulations were conducted using the full (i.e. not truncated) LJ potential and employing the Janeček [95] long-range correction beyond the cutoff radius $r^c = 3 \sigma$. As discussed in Section 1.4, the potential energy, the forces acting on the molecules, and the virial are thereby split into an explicitly computed part and a long-range correction. The calculation of the correction terms was conducted at every tenth time step.

The interfacial tension γ of a planar vapour-liquid interface, which is oriented normally to the y axis, is given by the difference between the diagonal components of the virial tensor $\Pi_n - \Pi_t$ as expressed by Eq. (1.60), cf. the discussion from Section 1.3. Half of the virial contribution from each pairwise interaction is assigned to each of the coordinates of the two involved molecules. This localization of the pressure tensor deviates from other definitions, since there is no single unique definition of local pressure [62]. However, all localizations of the virial which do not alter its volume integral, including the present implementation, lead to the correct outcome for the overall surface tension in the case of systems with planar symmetry [62, 144].

Following this approach, MD simulations were conducted in the canonical ensemble with $N = 16\,000$ molecules. The equimolar thickness of the liquid film ℓ_e was varied between 12σ and the minimum stable configuration. The equimolar thickness was determined using the saturated densities ρ' and ρ'' for the given temperature, the simulation volume V , and the number of molecules N by

$$\ell_e = \frac{N - \rho''V}{(\rho' - \rho'')A}, \quad (2.18)$$

so that ℓ_e only depends on the boundary conditions applied to the molecular simulation within the canonical ensemble, not on the outcome of the simulation, and it does not vary over simulation time. The temperature was kept constant by a velocity scaling thermostat. The elongation of the simulation volume in y direction, i.e. normal to the interface, was $\ell_y = 50\sigma$.

For the simulation of a reference case, the number of molecules N was increased to $300\,000$, the elongation in y direction was $\ell_y = 100\sigma$, and a film thickness of $\ell_e = 40\sigma$ was used. The temperature T was varied between 0.7 and 1.25ϵ , i.e. from the triple point temperature up to 95% of the critical temperature. The simulations were carried out using the *ls1 mardyn* molecular dynamics code, cf. Section 4.1. The equation of motion was solved by a leapfrog integrator [152], whereby a time step of $t_\delta = 0.002\sigma\sqrt{m/\epsilon}$ was used. The equilibration was conducted for at least $120\,000$ time steps, followed by a production run over $840\,000$ time steps. The statistical errors given in the present section are triple standard deviations computed from seven block averages, each over $120\,000$ time steps.

The simulations of large liquid films (with $\ell_e = 40\sigma$) were carried out to approximate bulk phase behaviour. The resulting surface tension values are shown in Fig. 2.4. The regression

$$\gamma = 2.94\epsilon\sigma^{-2} \left(1 - \frac{T}{T_c}\right)^{1.23} \quad (2.19)$$

is obtained on this basis, with the critical temperature $T_c = 1.3126\epsilon$ determined by Pérez Pellitero *et al.* [153]. The type of correlation is the same as proposed by Vrabec *et al.* [63] whose scaling exponent for the LJTS fluid (i.e. 1.21) is very similar to the present one.

Moreover, simulations were also performed for thinner films ($\ell_e \leq 12\sigma$). Thereby, MD runs were conducted with successively smaller values of ℓ_e , until a minimum stable thickness was reached for the given temperature. In Fig. 2.5, representative density and differential pressure profiles are plotted over the y coordinate. It can be seen that for $\ell_e = 7$ and 12σ (at $T = 0.7\epsilon$), the density at the centre of the film almost matches the bulk liquid density at saturation, while it decreases slightly for $\ell_e = 4.3\sigma$. In the differential pressure, the deviation between the three simulations is more significant. The differential pressure at the centre of the film ($y = 0$) almost reaches the zero line for $\ell_e = 12\sigma$, while for $\ell_e = 4.3$ and 7σ , the pressure tensor is anisotropic throughout the film. The differential pressure can be seen as an indicator for the fluid to be isotropic or homogeneous.

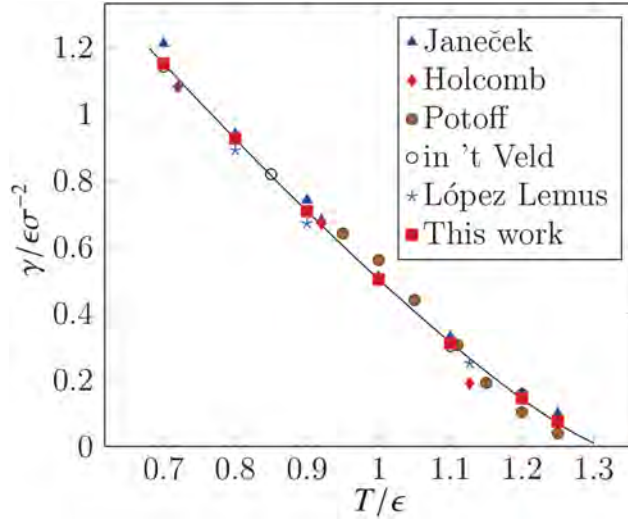


Figure 2.4: Surface tension γ over the temperature for LJ liquid films which are large enough to make finite-size effects insignificant (i.e. $\ell_e = 40 \sigma$). Comparison between this work (red squares) with the results of Janeček [95] (blue triangles), Holcomb *et al.* [154] (red diamonds), Potoff and Panagiotopoulos [155] (brown circles), in 't Veld *et al.* [107] (black circles), López Lemus and Alexandre [156] (blue stars) as well as the present correlation expression (solid line), cf. Eq. (2.19).

In Fig. 2.6, the differential pressure is shown over the density, corresponding directly to the profiles displayed in Fig. 2.5. Additionally, results at $T = 1 \epsilon$ are shown. All of the plots in Fig. 2.6 exhibit van der Waals loops, cf. the discussion by Imre *et al.* [150]. The red squares and green stars correspond to a large liquid film, while the blue circles and brown triangles show the result of the smallest stable liquid film. It can be seen that the differential pressure does not reach zero when finite-size effects become significant. The resulting surface tensions are shown in Tab. 2.3. For all temperatures, the surface tension decreases when the liquid film thickness decreases.

The maximum density in the liquid film, i.e. the density at the centre, is shown in Tabs. 2.4 and 2.5. For the largest simulated film thickness, this value agrees with the density of the saturated bulk liquid. For thin films, however, a significant deviation from the bulk density is found.

In Fig. 2.7, the surface tension, normalized by the surface tension obtained for a large system with $\ell_e = 40 \sigma$, is displayed over the film thickness for different temperatures. It can be seen that confinement between two planar vapour-liquid interfaces reduces the surface tension, and the numerical data suggest that this effect is proportional to ℓ_e^{-3} . In Fig. 2.8, the normalized density (reduced by the bulk liquid density at saturation) is shown. The relative density also decreases for thin films and, as for the surface tension, this effect is approximately proportional to ℓ_e^{-3} and becomes more significant at high temperatures.

For a film thickness $\ell_e > 12 \sigma$, the dependence of the surface tension on the film thickness becomes insignificant (taking the simulation uncertainty into account). For a fluid described by

T/ϵ	N	ℓ_y/σ	ℓ_t/σ	ℓ_e/σ	$\gamma/\epsilon\sigma^{-2}$
0.7	300 000	100	94.2	40.0	1.150(4)
	16 000	50	39.7	12.0	1.14(7)
	16 000	50	45.8	9.0	1.14(6)
	16 000	50	51.8	7.0	1.13(3)
	16 000	50	61.1	5.0	1.10(2)
	16 000	50	64.3	4.5	1.08(1)
	16 000	50	65.7	4.3	1.06(2)
0.8	300 000	100	96.4	40.0	0.93(1)
	16 000	50	40.3	12.0	0.92(6)
	16 000	50	46.4	9.0	0.92(3)
	16 000	50	52.3	7.0	0.91(3)
	16 000	50	61.2	5.0	0.87(3)
	16 000	50	63.9	4.55	0.85(2)
	0.9	300 000	100	98.2	40.0
16 000		50	40.8	12.0	0.71(5)
16 000		50	46.5	9.0	0.70(4)
16 000		50	51.9	7.0	0.69(3)
16 000		50	55.4	6.0	0.68(2)
16 000		50	58.1	5.4	0.66(3)
1.0		300 000	100	100	40.0
	16 000	50	40.1	12.0	0.50(6)
	16 000	50	46.1	9.0	0.50(2)
	16 000	50	50.8	7.0	0.48(5)
	16 000	50	53.0	6.2	0.5(1)
	1.1	300 000	100	102	40.0
16 000		50	40.9	12.0	0.31(4)
16 000		50	45.3	9.0	0.30(3)
16 000		50	48.6	7.25	0.28(4)
16 000		50	50.2	6.5	0.26(3)
1.2		300 000	100	101	40.0
	16 000	50	38.2	12.0	0.14(5)
	16 000	50	40.8	9.0	0.14(4)
	16 000	50	42.4	7.5	0.13(4)
	1.25	300 000	100	101	40.0
16 000		50	37.2	12.0	0.08(5)
16 000		50	39.2	9.0	0.06(2)
16 000		50	39.9	8.0	0.06(4)

Table 2.3: Surface tension γ in dependence of the liquid film thickness ℓ_e . The total elongation of the simulation box is indicated by ℓ_y in the direction perpendicular to the vapour-liquid interfaces and by ℓ_t ($= \ell_y = \ell_z$) in the tangential directions. The statistical error is given in parentheses, in terms of the magnitude corresponding to the final digit.

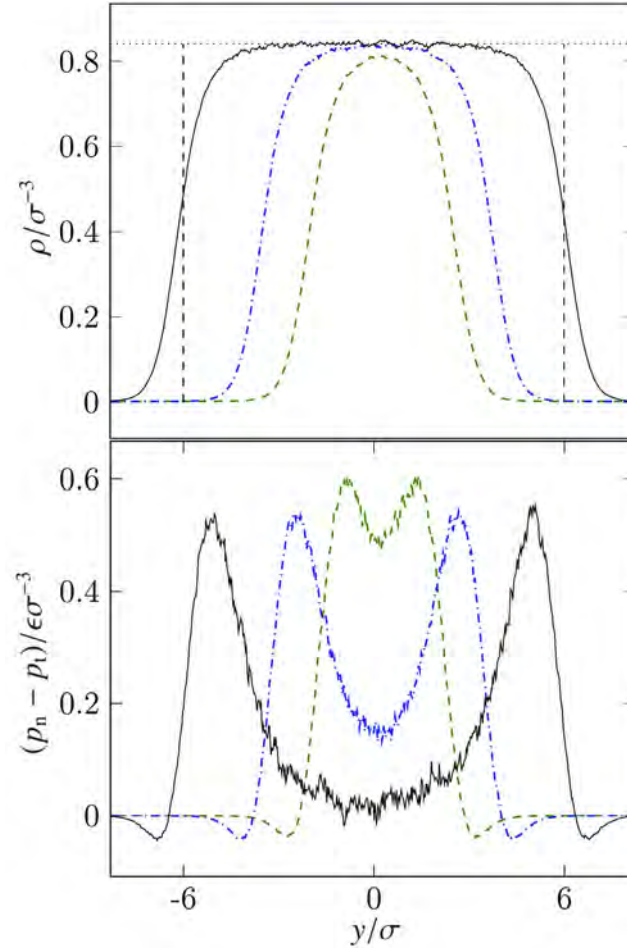


Figure 2.5: Density ρ (top) and differential pressure $p_n - p_t$ (bottom) over the y coordinate, i.e. the direction perpendicular to the interface. The temperature is $T = 0.7 \epsilon$. The blue dashed line corresponds to the minimum stable configuration which is $\ell_e = 4.3 \sigma$ for this temperature, while the red dash dotted one corresponds to $\ell_e = 7 \sigma$ and the black solid one to $\ell_e = 12 \sigma$. The dotted line in the upper picture represents the bulk liquid density and the difference between the vertical dashed lines in the upper picture represent the equimolar film thickness.

the LJ potential, e.g. methane [157], this means that the present finite-size effect is significant for liquid films which are thinner than five nanometres. At high temperatures, the deviation of the density at the centre of the liquid film from the bulk value increases.

The present results suggest that the reduction of the density and the surface tension due to confinement are two manifestations of the same effect, since both deviations scale with the inverse cube of the film thickness. The surface tension decreases with decreasing film thickness, and so does the density at the centre of the film. The differential pressure does not reach zero for liquid films with a thickness below 12σ , proving that under such conditions a bulk-like region is absent.

In particular, this contradicts the work by Weng *et al.* [146], who did not find a systematic correlation between the film thickness and the surface tension. For a LJ system at $T = 0.818 \epsilon$,

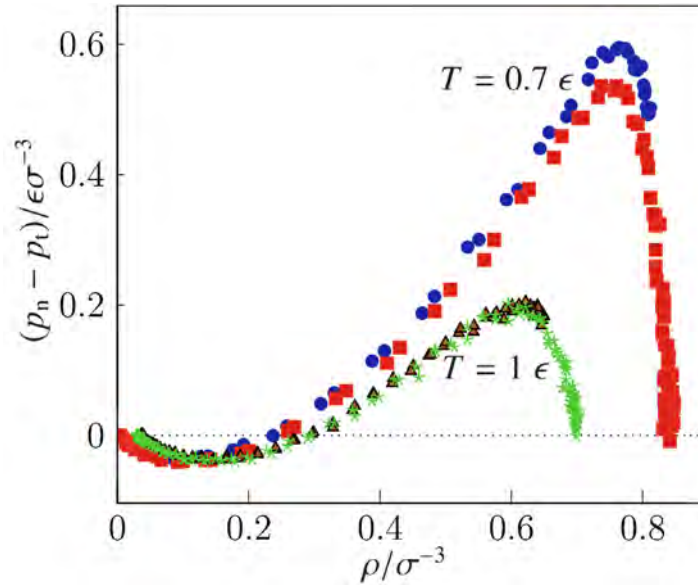


Figure 2.6: Differential pressure $p_n - p_t$ over the density, across an interface, for the temperatures $T = 0.7$ and 1ϵ . The blue circles ($\ell_e = 4.3 \sigma$) and brown triangles ($\ell_e = 6.2 \sigma$) correspond to the thinnest stable film at the respective conditions, while the red squares and green stars correspond to $\ell_e = 12 \sigma$. The dotted line represents the zero line, i.e. $p_n = p_t$ as in a bulk-like region where the pressure is isotropic.

Weng *et al.* [146] detected minor fluctuations around a constant value ($\gamma = 0.78 \pm 0.02 \epsilon \sigma^{-2}$), without a clear tendency, for a range of film thicknesses between $\ell_e = 5$ and 9σ . A juxtaposition with the present numerical data, cf. Tab. 2.3 and Fig. 2.7, according to which varying the liquid film thickness to such an extent has a significant influence on γ , clearly shows that the present simulation results do not confirm the postulate of Weng *et al.* that «with film thickness ... surface tension values and density profiles show little variation» [146]. The simulations by Weng *et al.* [146], however, were only carried out over 120 000 time steps, as opposed to a million time steps for the present series of simulations. Since systems with an interface relax more slowly than the homogeneous bulk fluid, the extremely short simulation time could constitute a serious limitation, affecting the accuracy of the results obtained by Weng *et al.* [146] to a significant extent.

The comparison with results from a recent study by Malijevský and Jackson [158] suggests that the present results on confinement by two parallel planar vapour-liquid interfaces might also carry over qualitatively to confinement by the opposite sides of the single spherical interface that surrounds a small droplet. Therein, Malijevský and Jackson [158] come to the conclusion that for liquid droplets, the size dependence of the surface tension is best described by two distinct, additive terms: The conventional Tolman term, representing curvature, which increases the surface tension (i.e. the Tolman length is found to be negative), as well as «an additional curvature dependence of the $1/R^3$ form» which causes an eventual decrease of the surface tension «for smaller drops» [158]. Furthermore, Malijevský and Jackson observe that

ℓ_e/σ	T			
	0.7ϵ	0.8ϵ	0.9ϵ	1ϵ
40	0.8410(2)	0.7974(3)	0.7507(6)	0.699(1)
12	0.84(3)	0.80(2)	0.75(1)	0.70(1)
9	0.84(1)	0.80(1)	0.75(1)	0.69(2)
7	0.83(1)	0.79(1)	0.74(2)	0.68(2)
6.2	n/a	n/a	n/a	0.66(5)
6	n/a	n/a	0.73(2)	★
5.4	n/a	n/a	0.72(1)	★
5	0.82(1)	0.77(1)	★	★
4.55	n/a	0.76(3)	★	★
4.5	0.81(1)	★	★	★
4.3	0.81(1)	★	★	★

Table 2.4: Density ρ' at the centre of the liquid film, in dependence of the temperature and the equimolar film thickness ℓ_e , for low temperatures; n/a: no simulation was carried out; asterisks: the liquid film was found to be unstable. The statistical error is given in parentheses, in terms of the magnitude corresponding to the final digit.

the characteristic droplet radius, below which this negative corrective term becomes dominant, «increases with increasing r^c » and conjecture that «such a crossover occurs when ... no “bulk” region can be assigned inside the drop. In this case even particles in the centre of the drop “feel” the interface» [158].

The present results lend further plausibility to this conjecture of Malijevský and Jackson [158]. There could be a relation between their $1/R^3$ term and the $1/\ell_e^3$ confinement effect from the present study. According to such a hypothesis, these contributions would both represent the deviation from bulk-like behaviour of the liquid phase due to confinement.

2.3 Density of dispersed gas bubbles

The present section illustrates the contribution that molecular modelling and simulation can make to the discussion of nano-dispersed gas bubbles in equilibrium with a liquid at negative pressure.⁴ This case is both of fundamental scientific interest and technically important, e.g. for cavitation. Neglecting size effects on γ , the surface free energy is often approximated by $\mathcal{A}^E \approx \gamma A$, cf. Eq. (1.31). While such a simplification is justified for macroscopic systems, it may violate the thermodynamics of small systems [90], cf. Section 2.1, where significant finite size effects can be present even for planar phase boundaries [91], cf. Section 2.2.

At the curved interface of a bubble or a droplet, the mechanical equilibrium condition is characterized by the Laplace equation, cf. Eq. (1.20), which holds for the Laplace (or surface

⁴This section is based on Horsch *et al.* [55].

ℓ_e/σ	T		
	1.1 ϵ	1.2 ϵ	1.25 ϵ
40	0.6393(4)	0.564(2)	0.515(7)
12	0.63(3)	0.56(3)	0.49(10)
9	0.62(2)	0.54(3)	0.46(4)
8	n/a	n/a	0.43(15)
7.5	n/a	0.51(7)	★
7.25	0.59(3)	★	★
6.5	0.57(8)	★	★

Table 2.5: Density ρ' at the centre of the liquid film, in dependence of the temperature and the equimolar film thickness ℓ_e , for high temperatures; n/a: no simulation was carried out; asterisks: the liquid film was found to be unstable. The statistical error is given in parentheses, in terms of the magnitude corresponding to the final digit.

of tension) radius R_L . The interface tends to contract, compressing the dispersed phase which is situated inside, and the surface tension γ couples this compressing effect with its cause, the curvature of the interface. By convention, the radius R_L is positive in case of a droplet (with $p' > p''$) and negative in case of a bubble (with $p' < p''$). Within the thermodynamic approach of Gibbs [89], the position of the formal dividing surface is arbitrary at first. Thus, a further condition, such as Eq. (1.20), is needed to define a radius.

Thereby, the values of p' and p'' are thermodynamic rather than mechanical quantities. They do not necessarily agree with the actual mechanical pressures on the two sides of the interface. Instead, they are obtained by combining the Laplace equation with the chemical and thermal equilibrium conditions, i.e. equal chemical potential $\mu_i' = \mu_i''$ for all components i and equal temperature $T' = T''$. The relation between the values of μ_i , p , and T is given by the equation of state for the bulk phases.

For the case of a pure fluid below the critical temperature, a $\mu - p$ diagram [159] visualizes the impact of curvature, by means of a vapour-liquid equilibrium condition with a pressure difference between both phases, as expressed by Eq. (1.20), on other thermodynamic properties such as the density of the coexisting fluid phases and the chemical potential, cf. Fig. 2.9. The normalized residual chemical potential $\tilde{\mu}$ is defined by the deviation of the chemical potential μ from its ideal temperature-dependent (i.e. density-independent) contribution μ^{id} , reduced by temperature [8]

$$\tilde{\mu}(\rho, T) = \frac{\mu(\rho, T) - \mu^{\text{id}}(T)}{T}. \quad (2.20)$$

At low densities, it can be approximated by

$$\tilde{\mu} \approx \ln \rho, \quad (2.21)$$

so that the vapour parts of the three isotherms shown in Fig. 2.9 coincide roughly. Its derivative

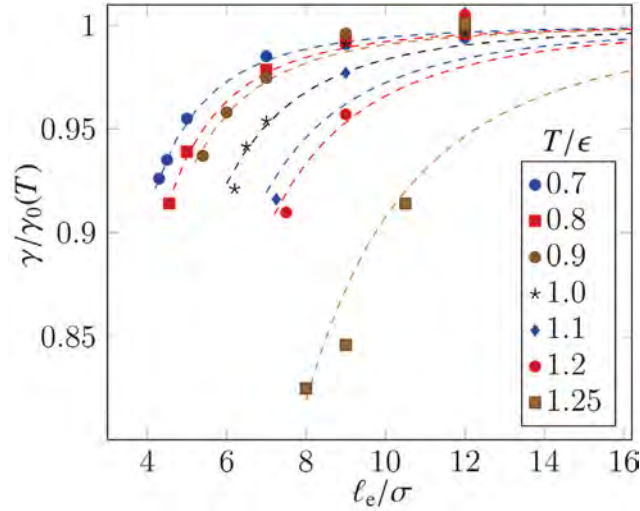


Figure 2.7: Normalized surface tension, reduced by the macroscopic vapour-liquid surface tension, over the film thickness ℓ_e for different temperatures. The dashed lines represent the expression $1 - a(T)\ell_e^{-3}$, where temperature-dependent coefficients were adjusted to simulation results, yielding $a(0.7 \epsilon) = 5.8 \sigma^3$, $a(0.8 \epsilon) = 7.9 \sigma^3$, $a(0.9 \epsilon) = 9.3 \sigma^3$, $a(1 \epsilon) = 16 \sigma^3$, $a(1.1 \epsilon) = 28 \sigma^3$, $a(1.2 \epsilon) = 34 \sigma^3$, and $a(1.25 \epsilon) = 93 \sigma^3$.

with respect to pressure at constant temperature is given by

$$\left(\frac{\tilde{\mu}}{p}\right)_T = \frac{1}{\rho T}. \quad (2.22)$$

Hence, proceeding (at increasing density) from stable vapour to metastable vapour, to the unstable part of the isotherm, the metastable and finally the stable liquid, the slope of the curves in the $\mu - p$ diagram decreases successively. In Fig. 2.9, it can be seen how $\Delta p = p' - p'' > 0$, corresponding to a droplet, induces a vapour-liquid equilibrium at a supersaturated chemical potential with $\mu > \mu^s$, where μ^s is the chemical potential at saturation in a macroscopic system over a planar interface at the same temperature. Obversely, in case of a bubble, the pressure is higher in the gas phase, i.e. $\Delta p < 0$, so that the coexisting phases become subsaturated ($\mu < \mu^s$).

For nano-dispersed fluid phases, where an isotropic bulk-like region may be completely absent, thermodynamic and mechanical definitions of γ deviate from each other, as discussed above. In particular, mechanical approaches (following the virial route), have found the surface tension of nanodroplets to be significantly smaller than that of the planar vapour-liquid interface [63, 70], whereas thermodynamic routes, e.g. the test area method [83] and grand canonical Monte Carlo simulation [121], do not confirm this and find the curvature effect on γ to be much weaker or even of opposite sign.

An explanation of this disagreement between mechanical and thermodynamic expressions for the surface tension is possibly to be found in the observation of Percus *et al.* [88] that in

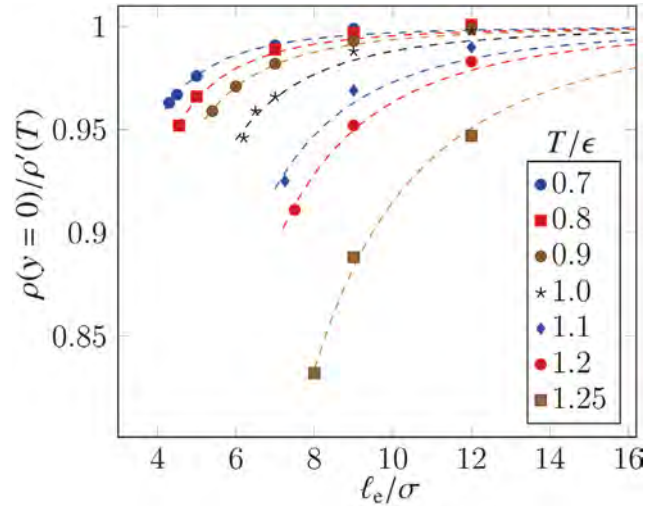


Figure 2.8: Normalized density at the centre of the liquid film, reduced by the saturated bulk liquid density, over the film thickness ℓ_e for different temperatures. The dashed lines represent the expression $1 - b(T)\ell_e^{-3}$, where temperature-dependent coefficients were adjusted to simulation results, yielding $b(0.7 \epsilon) = 3.0 \sigma^3$, $b(0.8 \epsilon) = 4.4 \sigma^3$, $b(0.9 \epsilon) = 6.3 \sigma^3$, $b(1 \epsilon) = 12 \sigma^3$, $b(1.1 \epsilon) = 27 \sigma^3$, $b(1.2 \epsilon) = 37 \sigma^3$, and $b(1.25 \epsilon) = 85 \sigma^3$.

general, the Landau free energy deviates from the volume integral over the local pressure for inhomogeneous fluid systems. Furthermore, it was proven by Lau *et al.* [64] that in case of spherical interfaces, the definition of the surface tension as the differential excess free energy of the interface can only be recovered by a mechanical approach if the contribution from the second-order virial is also considered.

The Laplace radius R_L has the disadvantage of being defined by the surface tension of the curved interface, which is thermodynamically well-defined, but hard to determine. In consequence, it is difficult to evaluate how many molecules are inside a bubble or a droplet with the Laplace radius R_L (which would be precisely known if an equimolar radius was specified), or which chemical potential and pressure difference correspond to a particular value of R_L . Hence, considering that the dependence of the surface tension on curvature is under dispute at present, Eq. (1.20) contains two unknowns and the Laplace radius is ill-defined at first. For this reason, the theory of curved interfaces in terms of the capillarity radius R_κ is employed here, cf. Section 2.1, considering nanoscopic gas bubbles.

Building on the results for the excess equimolar radius of liquid droplets from Section 2.1, a series of MD simulations was conducted, using the *ls1 mardyn* program, for volumes containing a LJTS gas bubble in equilibrium with a subsaturated liquid. The simulations were carried out in the canonical ensemble with a periodic boundary condition. The initial conditions were chosen such that a single bubble existed in the centre of the simulation box. The size of that bubble was controlled by choosing the number of molecules and the simulation volume appropriately. As pointed out by Fisher and Wortis [161] as well as Reguera *et al.* [162],

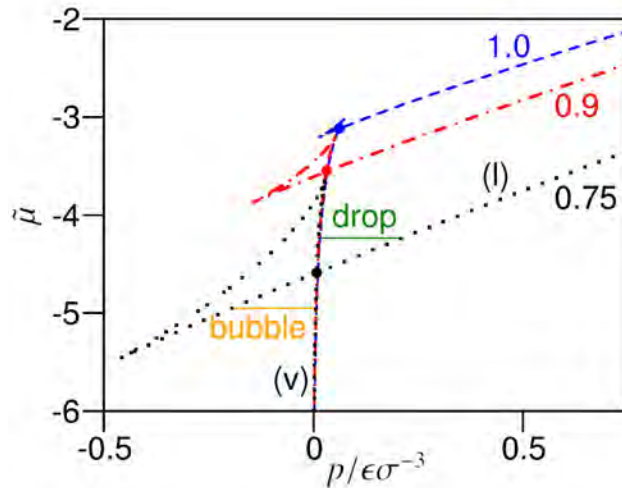


Figure 2.9: Isothermal dependence of the normalized residual chemical potential $\tilde{\mu}$, cf. Eq. (2.20), on the pressure p from a virial expansion [160] for the LJTS potential at temperatures of 0.75 (\cdots), 0.9 ($\cdot - \cdot$), and 1ϵ ($- -$). The plot extends over the whole range of vapour (v) and liquid (l) densities including stable, metastable and unstable states. Self-intersections of the isotherms (\bullet) correspond to the phase equilibrium condition at a planar interface, i.e. $\mu' = \mu'' = \mu^s(T)$ and $p' = p'' = p^s(T)$. Solid horizontal lines: Vapour-liquid equilibrium at a curved interface characterized by the Laplace equation, cf. Eq. (1.20), where the temperature is 0.75ϵ and the pressure is smaller outside than for the dispersed phase, which is confined by the interface, with a pressure difference of $p' - p'' = \pm 0.2 \epsilon \sigma^{-3}$.

such equilibria can be thermodynamically stable, even if the phase (here, the subsaturated liquid) which surrounds the dispersed phase (here, the gas bubble) would be metastable in a corresponding homogeneous state. In such a case, the simulation volume has to be relatively small – the precise conditions depend on the equation of state of the fluid – for configurations containing a single gas bubble.

The present MD simulations are therefore concerned with the scenario where a single gas bubble is surrounded by a subsaturated liquid phase, under equilibrium conditions for the pure LJTS fluid. To evaluate the equations of motion numerically, a Verlet leapfrog integrator was used, with an integration time step of $0.003 \sigma \sqrt{m/\epsilon}$. The total momentum of the system was neutralized every 16 000 time steps, by subtracting equal fractions of it from all molecules, and the system of coordinates was continuously shifted, following the random motion of the bubble to keep its centre in the origin. The temperature was specified to be $T = 0.75 \epsilon$, i.e. about 70 % of the critical temperature [63], and controlled by a velocity rescaling thermostat (also known as an isokinetic thermostat). A novel shading approach for the visualization of point-based datasets, which makes it easier to analyse the morphology of an interface on the molecular level [163], was applied to individual configurations, cf. Fig. 2.10.

The number of molecules N and the simulation volume $V = \ell^3$ were varied as indicated in Tab. 2.6. An equilibration was conducted for at least 400 000 time steps. Subsequent-

N	V/σ^3	ρ'_∞/σ^{-3}	ρ'_0/σ^{-3}	$p'/\epsilon\sigma^{-3}$	$p''/\epsilon\sigma^{-3}$	$-R_e/\sigma$	$-R_\kappa/\sigma$
7 303	10 648	0.736(2)	0.023(3)	-0.16	0.0061	5.6	6.1
9 551	13 824	0.7365(3)	0.0145(8)	-0.15	0.0061	5.9	6.2
20 514	29 791	0.745(1)	0.02(1)	-0.101	0.0068	8.1	9.2
18 107	27 000	0.746(1)	0.008(3)	-0.093	0.0069	8.7	9.9
42 474	64 000	0.7493(3)	0.010(1)	-0.068	0.0072	12.1	13.1
34 944	54 872	0.751(3)	0.009(2)	-0.058	0.0074	12.6	15.1
75 794	117 649	0.7521(5)	0.011(1)	-0.048	0.0075	16.0	17.7
122 232	195 112	0.7538(2)	0.0113(3)	-0.035	0.0077	20.0	23.0
263 163	438 976	0.7556(4)	0.0117(5)	-0.022	0.0079	28.0	32.8

Table 2.6: Number of molecules N and simulation volume V for a series of canonical ensemble MD simulations of LJTS bubbles in equilibrium (at $T = 0.75 \sigma$). The density ρ'_∞ of the liquid phase was also determined by following an approximation for the outer part of the the density profiles, cf. Eq. (2.15), to an infinite distance from the centre of the bubble. It is subsaturated with respect to the saturated liquid density of the bulk fluid, i.e. $0.7594 \pm 0.0003 \sigma^{-3}$ [63]. The gas density ρ'_0 was determined in a region closer than 1.5σ to the centre of the bubble. (Errors for the density, with a magnitude corresponding to that of the final digit, are given in parentheses.) The liquid and vapour pressures p' and p'' to be used within the Gibbs approach, respectively, were both computed from the extrapolated liquid density by a fifth-order virial expansion [160]; they may deviate from the mechanical pressure. From the equimolar and capillarity radii R_e and R_κ , respectively, which are negative by the convention employed here, the excess equimolar radius $R^E = R_e - R_\kappa$ can be obtained; the value of R^E is found to be positive (and of the order of 1σ).

ly, density profiles were determined by binning over several averaging intervals of at least 200 000 time steps until the profiles of were found to converge. In one of the cases (with $N = 20 514$ and $V = 29 791 \sigma^3$), bubble configurations were found to alternate with homogeneous subsaturated liquid configurations, cf. Fig. 2.11. This simulation was also evaluated, taking only such density profiles into account where a bubble was actually present.

From these density profiles, cf. Figs. 2.11 and 2.12, all quantities were determined which are relevant to the theoretical approach discussed in Section 2.1. For this purpose, an extrapolated liquid density ρ'_∞ was determined from the limit to which an exponential approximant, cf. Eq. (2.15), adjusted to the outer part of the density profile $\rho(r)$, converges at $r \rightarrow \infty$ in terms of the distance r from the centre of the bubble. An analogous term was also adjusted to the inner part of the density profile. Standard deviations on the basis of different density profiles, collected from the same simulation during successive time intervals, were calculated to estimate the simulation error. The criterion from Eq. (1.19) was then applied to the density profile, i.e. to the actual profile $\rho(r)$, not the correlation, to obtain the equimolar radius R_e . The pressure p'' inside the gas bubble, and thereby the capillarity radius

$$R_\kappa = \frac{2\gamma_0}{p' - p''}, \quad (2.23)$$

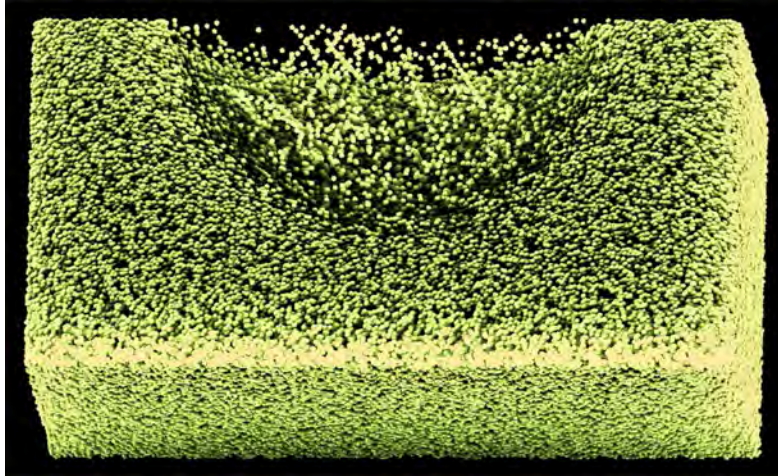


Figure 2.10: Visualization of a configuration containing a nanobubble surrounded by liquid, using the novel PointAO shading algorithm, cf. Eichelbaum *et al.* [163].

was not determined here from the density profile on the vapour side, as it was done in Section 2.1 to analyse liquid droplets. Instead, exploiting the fact that the liquid phase can be sampled very accurately here, the density of the subsaturated liquid surrounding the bubble was used.

The density in the centre of the bubble should be expected to approach the saturated vapour density, i.e. $\rho''(T) = 0.0124 \sigma^{-3}$ for $T = 0.75 \epsilon$ [63], in the limit of an infinitely large bubble ($R_L \rightarrow -\infty$), which corresponds to the transition to a planar interface. The present simulation results confirm this, cf. Tab. 2.6 and the results for $R_e = -28 \sigma$ shown therein. Moreover, deviations of the vapour density in the centre of the bubble from the saturated vapour density are observed for small bubbles, cf. Fig. 2.13. These deviations exhibit two qualitatively distinct effects:

1. For relatively large bubbles, the density in the centre decreases as the size of the bubble becomes smaller. The minimal gas density observed in the present series of simulations, which is significantly below $0.01 \sigma^{-3}$, is found in the centre of a bubble with $R_e = -8.7 \sigma$.
2. For even smaller bubbles, the density in the centre increases again. In the smallest case considered here, i.e. $R_e = -5.6 \sigma$, the gas phase is found to be much denser than that which coexists with the liquid at a planar interface, cf. Figs. 2.12 and 2.13.

The density of the liquid phase surrounding the gas bubble was found to be significantly subsaturated: In all cases, the deviation between the saturated liquid density and the actual liquid density was over four times larger than the accumulated error for both quantities.

In Tab. 2.6, further numerical results are shown that were obtained from these simulations based on the liquid densities extracted from the present density profiles. In particular, smaller bubbles consistently correspond to smaller liquid densities here, in agreement with capillary theory. The excess equimolar radius $R^E = R_e - R_x$ was found to be positive, indicating a

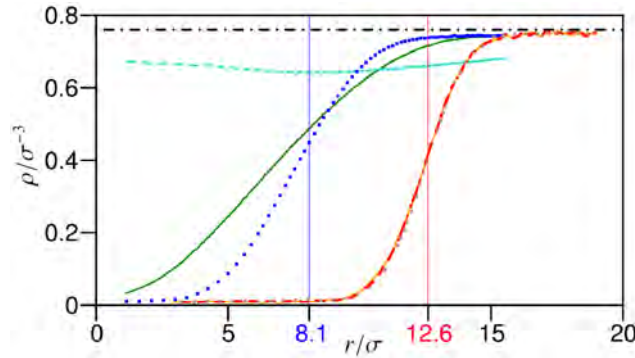


Figure 2.11: Density profiles of LJTS bubbles surrounded by liquid, collected during different sampling intervals from two MD simulation runs, both in the canonical ensemble at $T = 0.75 \epsilon$. The density profiles on the right side correspond to sampling intervals from 45 000 to 60 000 (—), 60 000 to 70 000 (– –), and 70 000 to 80 000 time steps ($\cdot \cdot \cdot$) after simulation onset, with $N = 34\,944$ and $V = (38 \sigma)^3$, exhibiting fast convergence and negligible fluctuations. The density profiles on the left side, corresponding to $N = 20\,514$ and $V = (31 \sigma)^3$ with sampling intervals from 14 to 16 (—), 24 to 26 (– –), and 34 to 36 million time steps ($\cdot \cdot \cdot$) after simulation onset, alternate between configurations where a bubble is present and homogeneous subsaturated liquid configurations. Horizontal dash-dotted line: Density of the bulk liquid at saturation; Vertical lines: Equimolar radii of the bubbles.

deviation from the capillarity approximation where, to first order in $1/R$, the surface tension of a droplet is larger and the surface tension of a bubble is smaller than that of the planar vapour-liquid interface.

For the vapour phase, nanobubbles with radii above 7 or 8 σ , roughly corresponding to diameters above 6 nm for the LJTS fluid [63], were found to have a smaller density than the saturated bulk vapour, cf. Fig. 2.12. This is the behaviour which should be expected from capillary theory, based on Gibbs' thermodynamic interpretation of the Laplace equation.

On the other hand, the vapour density in the centre of the bubble was found to increase again for smaller bubbles, eventually even exceeding the dew density. This is not paralleled by an increase, but rather by a further decrease of the liquid density, which shows that in terms of the chemical potential, these extremely small bubbles are still subsaturated. This suggests that both phases, vapour and liquid, tend to become subsaturated due to interfacial curvature, cf. Fig. 2.9. The density in the centre of the bubble, however, experiences an additional obverse influence due to a size-dependent phenomenon which is distinct from curvature.

The density profiles, cf. Fig. 2.12, help to isolate this effect: The density of the gas phase is increased not due to curvature, which tends to reduce μ and thereby also ρ'' , but because there is not enough space available in radial direction for the density profile to converge to the bulk density that would correspond to the respective value of μ . This second effect should be ascribed to the extremely small size of the nanobubbles rather than to their curvature.

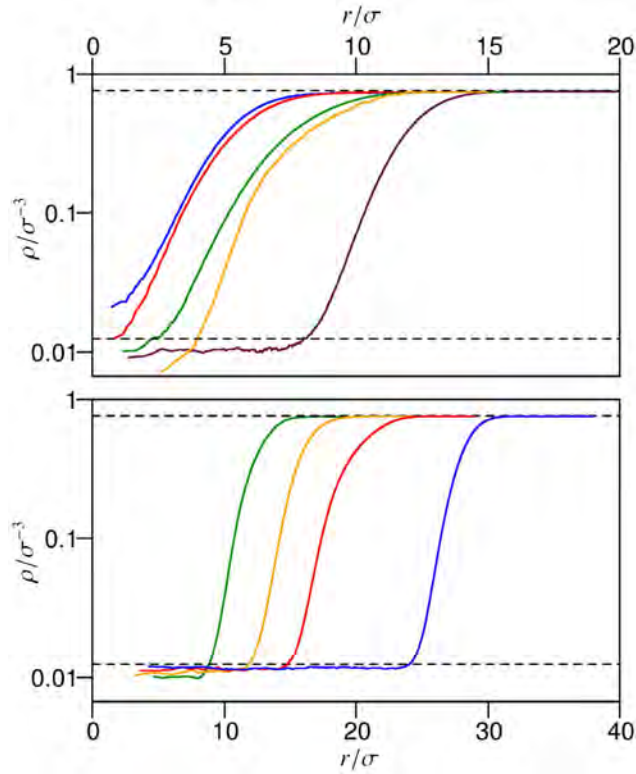


Figure 2.12: Density profiles of bubbles in equilibrium with a subsaturated liquid phase from MD simulation of the LJTS fluid in the canonical ensemble (—) in comparison with the vapour and liquid densities at saturation (---), for a temperature of $T = 0.75 \epsilon$. Top: Results for five relatively small bubbles with equimolar radii $R_e = -5.6, -5.9, -8.1, -8.7,$ and -12.1σ (from left to right); Bottom: Results for four relatively large bubbles with $R_e = -12.6, -16.0, -20.0,$ and -28.0σ (from left to right).

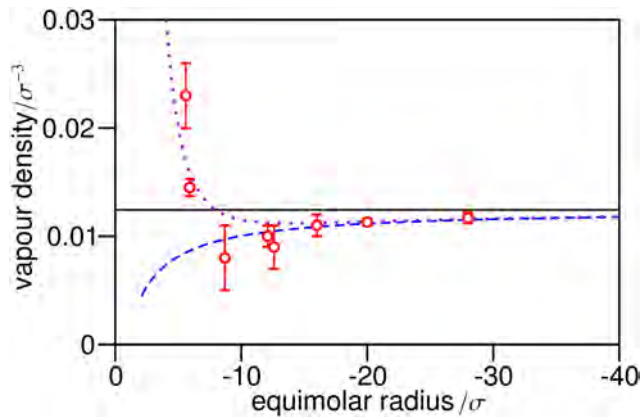


Figure 2.13: Density in the centre over the equimolar radius of gas bubbles, which is negative here by convention, from present MD simulations of the LJTS fluid in the canonical ensemble at $T = 0.75 \sigma$ (\circ) in comparison with the vapour density at saturation (—) and a thermodynamic prediction from the capillarity approximation (---), considering curvature effects only and assuming $\gamma = \gamma_0$ (and hence $R_L = R_k = R_e$), as well as a correlation (\cdots) which accounts for the deviation from capillarity by an excess vapour density of $\Delta\rho = -1.5/R_\rho^{-3}$, proportional to the inverse cube of the radius.

Regarding the thermodynamic properties of nano-dispersed fluid phases, Tröster and Binder [164] have recently pointed out that for small droplets, there is a significant deviation from the planar surface tension, but this effect does not consistently agree with the Tolman equation. Therefore, «neither the capillarity approximation nor the Tolman parametrization [. . .] should be employed in any serious quantitative work» [164]. The present analysis supports this conclusion. Instead of the Tolman equation, a new theoretical framework needs to be developed to describe the various size-dependent effects related to the curvature, the diameter, and possibly the circumference as well as the volume, which controls the magnitude of fluctuations, in a coherent way.

3 Fluids in contact with solid surfaces

3.1 Wetting of planar solid surfaces

Equilibrium wetting behaviour is typically classified according to the contact angle $0^\circ \leq \theta \leq 180^\circ$ of a sessile droplet.¹ The contact angle depends on the interaction between the particles, namely the fluid–fluid and the solid–fluid interactions. These can be explicitly described with force fields and, hence, the force fields yield the contact angle. There is a significant body of literature on predicting the contact angle with force fields, both for droplets [166–172] and liquid cylinders [173]. However, most of that work is restricted to particular material combinations, such as water on graphene.

In the present section, the dispersive fluid–wall interaction is varied systematically for a LJTS model system, consisting of a single sessile droplet on a planar wall. In this way, the influence of the unlike interaction on the contact angle in a model system is characterized. The LJTS potential is used here for the fluid particle (f), wall particle (w), and fluid–wall (fw) interactions, and both the fluid–wall interaction and the temperature are varied. The size parameter σ_w of the wall particle interaction is also varied to obtain substrates of different densities, and the fluid interaction parameters σ_f and σ_w serve as the basis to define the LJ system of units. The results are correlated and discussed in the context of previous studies on the wetting behaviour of LJ fluids [171, 174–176].

The wall is represented here by particles arranged in a face-centered cubic lattice with the (100) surface exposed to the fluid. To maintain the wall in the solid state, the LJTS energy parameter of the wall is related to that of the fluid by $\epsilon_w = 100 \epsilon_f$. In terms of the LJTS size parameter for the wall σ_w , this yields a lattice constant of $\Lambda = 1.55 \sigma_w$ and a wall density of $\rho_w = 1.07 \sigma_w^{-3}$. The cutoff radius for the LJTS fluid, i.e. $r^c = 2.5 \sigma_f$, yields practically the same lattice constant as would have been obtained for $r^c \rightarrow \infty$, i.e. for the full LJ potential.

Unless stated otherwise, the size parameters of the solid and the fluid are the same in the present study, i.e. $\sigma_w = \sigma_f$. However, for a series of simulations in which the influence of the solid density is studied, σ_w is varied as well. By scaling down σ_w , the lattice constant of the solid is decreased and, hence, the density is increased: For the size parameters $\sigma_w = 0.8$ and

¹This section is based on Becker *et al.* [165].

$0.646 \sigma_f$, the wall density is $\rho_w = 2.10$ and $4.02 \sigma_f^{-3}$, respectively. The interaction between the fluid and the wall is also described by the LJTS potential, where the unlike size parameter is $\sigma_{fw} = \sigma_f$, even in the cases where the size parameter σ_w of the solid substrate is varied. The LJTS energy parameter of the fluid-wall interaction is given by

$$\epsilon_{fw} = \zeta \epsilon_f, \quad (3.1)$$

wherein ζ is the reduced fluid-wall interaction energy. Its influence on the contact angle is studied systematically in the present section. The ζ parameter is related to the coefficient ξ from the modified Berthelot rule, cf. Eq. (1.8), by $\zeta = 10 \xi$.

Periodic boundary conditions are applied in all directions, leaving a channel for the fluid between the wall and its periodic image. The height of the channel exceeds $30 \sigma_f$ in all cases, avoiding artefacts which would be caused by finite-size effects in much smaller channels [177]. Furthermore, the wall thickness (i.e. 2.5 crystal unit cells here) exceeds the cutoff radius of the fluid, so that fluid molecules adsorbed on opposite sides do not interact with each other.

The interaction of a fluid particle with the wall is the cumulative interaction of that fluid particle with all wall particles. This cumulative fluid-wall potential u^Σ depends on the density of the wall and the distance y between the particle and the wall; insofar as the wall is not perfectly smooth, it also depends on the lateral position above the wall, which is given by x and z . For any lateral position (x, z) , variation of the y coordinate yields a minimum $u_{\min}^\Sigma(x, z)$ of the cumulative potential, corresponding to a local well depth of the fluid-wall interaction. The average well depth

$$W = -\left\langle u_{\min}^\Sigma(x, z) \right\rangle_{(x,z)}, \quad (3.2)$$

is defined by averaging these minima over the (x, z) plane. The average well depth W is used here to compare different expressions for the fluid-wall interaction in terms of a single scalar value [18]. Since the LJTS potential is only positive in the extremely repulsive region with $r_{ij} < \sigma_{fw}$, the minimum of the cumulative fluid-wall interaction $u_{\min}^\Sigma(x, z)$ is negative here, and W is a positive quantity. For the present systems, the average well depth is given by

$$\begin{aligned} W &= 3.32 \epsilon_{fw} & \text{for } \sigma_w &= \sigma_f, \\ W &= 5.21 \epsilon_{fw} & \text{for } \sigma_w &= 0.8 \sigma_f, \\ W &= 8.70 \epsilon_{fw} & \text{for } \sigma_w &= 0.646 \sigma_f. \end{aligned} \quad (3.3)$$

A single sessile droplet on a planar solid wall is considered here, cf. Fig. 3.1, so that there is no droplet on the opposite side of the periodic image of the wall. In the entire regime of partial wetting ($0^\circ < \theta < 180^\circ$), this – rather than two smaller droplets on both sides – is the thermodynamically stable configuration [178]. The wall is located in the (x, z) plane, so that

y represents the vertical distance from the centres of the atoms of the top wall layer.

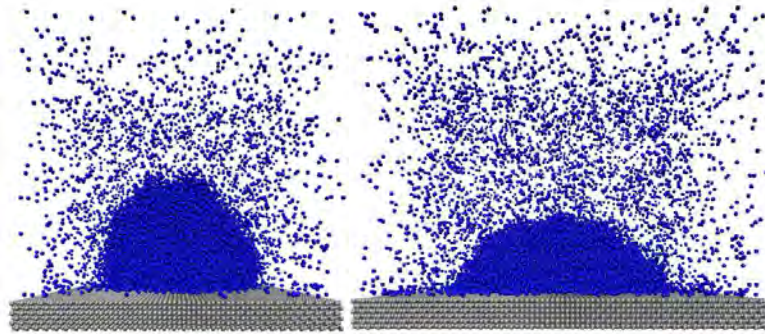


Figure 3.1: Simulation snapshots, taken with VMD [179], at a temperature of $T = 0.8 \epsilon_f$. The reduced fluid-wall interaction energy is $\zeta = 0.25$ (left) and 0.65 (right), respectively, resulting in different contact angles.

For this system, MD simulations are carried out in the canonical ensemble, using the *ls1mardyn* program, to obtain the contact angle dependence on the temperature and the reduced fluid-wall interaction energy. The number of fluid molecules is 15 000, and the number of wall particles varies according to the box dimensions. Newton's equations of motion are integrated via the Verlet leapfrog algorithm with a time step of $5 \times 10^{-4} \sigma_f \sqrt{m/\epsilon_f}$. The equilibration time is at least 2.5 million time steps, followed by 3.5 million time steps of production.

The position of the vapour-liquid interface is defined by the place where the arithmetic mean of the saturated bulk vapour and liquid densities is reached. A sphere is fitted to this interface, excluding the region of immediate contact with the wall (which is dominated by adsorption), and the intersection of the sphere with the wall ($y = 0$) is used to determine the contact angle, cf. Fig. 3.2. The mean contact angle is determined from the density profile averaged over the entire production period, and the simulation uncertainty is estimated by blockwise averaging over 500 000 time steps.

In a series of MD simulations with $\sigma_w = \sigma_f$, reduced fluid-wall interaction energies are systematically varied for temperatures between 0.7 and $1.0 \epsilon_f$. The simulation results, which can be correlated by

$$\cos \theta(\tau, \zeta) = \chi(1 + \tau^\nu)(\zeta - \zeta_0), \quad (3.4)$$

are shown in Fig. 3.3. Therein, $\tau = (1 - T/T_c)$ is the thermal critical scaling parameter, reduced by the critical temperature of the LJTS fluid $T_c = 1.078 \epsilon_f$, cf. Vrabec *et al.* [63], while $\chi = 1.03$, $\nu = -0.69$, and $\zeta_0 = 0.514$ are the adjustable parameters of the correlation expression.

The contact angle $\theta = 90^\circ$ (i.e. $\cos \theta = 0$) occurs at $\zeta = \zeta_0$ and thus at a well depth of $W_0 = 1.71 \epsilon_f$. The value of ζ_0 , and hence that of W_0 , is found to be independent of temperature, corroborating previous work [180]. Large values of W correspond to a strong attraction between the fluid and the wall, and as expected, a higher attraction between the fluid and the

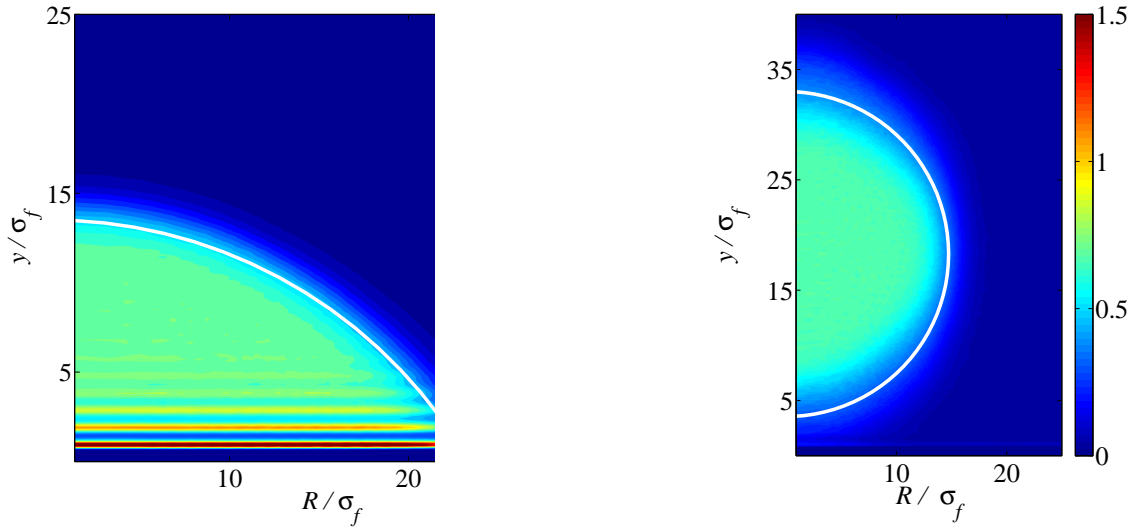


Figure 3.2: Density profiles of liquid droplets, where the local density (in units of σ_f^{-3}) is represented by colour as described in the legend (right). For $T = 0.8 \epsilon_f$ and $\zeta = 0.65$ (left), an adsorbed fluid phase can be observed next to the droplet. A simulation at $T = 0.9 \epsilon_f$ with $\zeta = 0.25$ (right) yields complete dewetting.

wall leads to a smaller contact angle. In particular, Eq. (3.4) agrees with the symmetry relation [178, 180, 181]

$$\cos \theta(T, \zeta_0 + \Delta\zeta) = -\cos \theta(T, \zeta_0 - \Delta\zeta). \quad (3.5)$$

To study the influence of the wall density on the contact angle, simulations are also carried out for walls with densities of $\rho_w = 2.10$ and $4.02 \sigma_f^{-3}$, i.e. using the size parameters $\sigma_w = 0.8$ and $0.646 \sigma_f$, respectively, for the wall potential. The simulation results for the contact angle can be correlated by Eq. (3.4) using the same value for ν as given above, combined with newly adjusted values for ζ_0 (and thus for W_0) and the gradient $\bar{\chi}$. In particular, if the correlation is expressed in terms of the well depth, i.e. by

$$\cos \theta(\tau, W, \rho_w) = \bar{\chi} (1 + \tau^\nu) \frac{W - W_0}{T_c}, \quad (3.6)$$

with a constant value of $\nu = -0.69$, both adjustable parameters $W_0(\rho_w)$ and $\bar{\chi}(\rho_w)$ are found to depend linearly on the wall density

$$\frac{W_0}{T_c} = 1.1 + 0.36 \frac{\rho_w}{\sigma_f^{-3}}, \quad (3.7)$$

$$\bar{\chi} = 0.38 - 0.04 \frac{\rho_w}{\sigma_f^{-3}}. \quad (3.8)$$

Therein, T_c always refers to the critical temperature of the fluid.

Contact angles in LJ systems have been studied by different authors before. Tab. 3.1 gives an overview which also includes the boundary conditions from the present study. While Shahrz

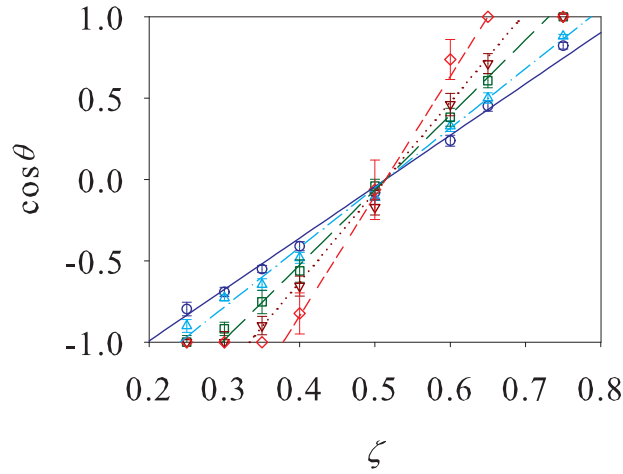


Figure 3.3: Simulation results (symbols) and correlation (lines), cf. Eq. (3.4), for the contact angle as a function of the reduced fluid-wall interaction energy at temperatures of $T = 0.7$ (\circ , —), 0.8 (\triangle , $\cdot\cdot\cdot$), 0.9 (\square , — —), 0.95 (∇ , - - -) and 1.0 ϵ_f (\diamond , - - -). The size parameter of the wall potential is $\sigma_w = \sigma_f$, yielding a wall density of $\rho_w = 1.07 \sigma_f^{-3}$.

et al. [182] consider a simulation setup where they investigate the contact angle of an infinitely long cylindrical LJ droplet, all other studies mentioned here consider spherical droplets.

source	ρ_w/σ_f^{-3}	r_{fw}^c/σ_f	T/ϵ_f	$W/\zeta T_c$
Ingebrigtsen and Toxvaerd [176]	0.60	∞	0.75	1.32
Shahraz <i>et al.</i> [182]	3.0	∞	0.7	3.61
Grzelak <i>et al.</i> [171]	0.58	5.0	0.7	3.0
Tang and Harris [175]	0.62	2.75	0.9	2.62
Nijmeijer <i>et al.</i> [174]	1.78	2.21	0.9	3.61
Nijmeijer <i>et al.</i> [168]	1.78	2.35	0.9	4.03
This work	1.07	2.5	0.8	3.08
	2.10	2.5	0.8	4.83
	4.02	2.5	0.8	8.07

Table 3.1: LJ model systems used for studies on wetting. The fluid-wall potentials of Ingebrigtsen and Toxvaerd [176] as well as Shahraz *et al.* [182] are continuous LJ-9-3 models, all other potentials are particulate LJ-12-6 models. The relation between W and ζ was obtained from the literature sources either directly or by analysing the respective wall model.

A direct comparison between present results, literature data, and the present universal correlation for LJ systems is given in Fig. 3.4. In most cases, the contact angles from the literature studies are accurately predicted by Eqs. (3.6) – (3.8), using only the information on the temperature and the solid density given in the literature sources, as well as the average fluid-wall well depth corresponding to the considered model surface. There are noticeable deviations from the results of Nijmeijer *et al.* [168], who apply a long-range correction to the forces

acting on fluid particles at distances $y > r^c$ from the wall, but neglect long-range forces completely for $y \leq r^c$. However, both short-range and long-range forces are actually strongest close to the wall. The combined potential of Nijmeijer *et al.* [168] is therefore defined inconsistently, which may explain the deviation between their work and the rest of the literature as well as the present correlation.

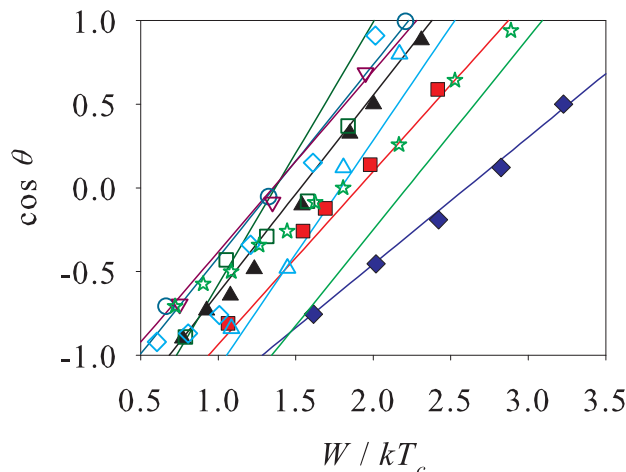


Figure 3.4: Contact angle cosine over the average well depth. The lines represent the correlation given by Eqs. (3.6) – (3.8), and the symbols are simulation results. This work at a temperature of $T = 0.8 \epsilon_f$: $\rho_w = 1.07 \sigma_f$ (\blacktriangle), $\rho_w = 2.10 \sigma_f$ (\blacksquare), $\rho_w = 4.02 \sigma_f$ (\blacklozenge). Ingebrigtsen and Toxvaerd [176], $T = 0.75 \epsilon_f$, (\circ); Shahraz *et al.* [182], $T = 0.7 \epsilon_f$, (\star); Grzelak *et al.* [171], $T = 0.7 \epsilon_f$, (∇); Tang and Harris [175], $T = 0.9 \epsilon_f$, (\square); Nijmeijer *et al.* [174], $T = 0.9 \epsilon_f$, (\triangle); Nijmeijer *et al.* [168], $T = 0.9 \epsilon_f$, (\diamond). The simulation results and the corresponding lines have identical colours.

3.2 Morphology of silane self-assembled monolayers

Silane self-assembled monolayers (silane SAMs) are widely used for modifying substrate surfaces.² Bigelow *et al.* [184] first reported on self-assembled monolayers on a substrate in the late 1940s. The covalent binding of the silane molecule to a suitable substrate and the self-assembly process leads to a very dense and robust monolayer. A large variety of surfaces can be modified by chemisorption of silane molecules, as for instance silicon [185], glass [186], or polydimethylsiloxane [187]. Depending on its end group, the silane transforms those substrates into highly hydrophobic or hydrophilic materials. Silane SAMs on silicon wafers are a common model system because of their highly controllable properties. The silane monolayer forms an extraordinarily homogeneous surface, both chemically and topographically. By choosing the end group of the silane, the surface wettability can be tuned.

²This section is based on Castillo *et al.* [183].

Lessel *et al.* [185] recently developed a recipe for a wet chemical production process for silanizing silicon wafers with methyl-terminated molecules such as dodecyltrichlorosilane (DTS) and octadecyltrichlorosilane (OTS). Although they provide insights into the surface parameters of the prepared silane SAMs, it is not clear how the silane molecules arrange on the substrate. In a recent study, Gutfreund *et al.* [188] developed a model for the molecular arrangement of the alkylsilanes based on X-ray scattering experiments. They employed an empirical three-film model to relate their experimental results to the molecular structure of the silane SAM, and found that the actual height of the silane layer is lower than the theoretical length of an elongated silane molecule, from which they concluded that the silane chains are tilted with respect to the substrate. However, the main property that can be measured with X-ray scattering is the electron density, which does not provide any direct information on molecular arrangement.

The geometrical characteristics of silane SAMs on the nanometre scale determine their macroscopic properties. Different simulation studies have been performed to analyse these monolayers. Mainly, self-assembled monolayers are characterized by the coverage Γ , i.e. the number of chemisorbed substituents per surface area. In many cases, both chemisorption and physisorption may occur, having separate contributions to Γ ; to the SAMs discussed in the present section, however, only chemisorption is of interest.

The coverage is usually invariant during a molecular simulation and has to be specified in advance. For example, Barriga *et al.* [189] ran MD simulations of OTS SAMs on silica at high coverage, varying the substitution pattern, molecular orientation, and temperature, finding that the OTS molecules were always aligned nearly vertically and thus highly ordered even far from the substrate. On the other hand, Barlow *et al.* [190] observed that the bonded OTS layer on silica is essentially crystalline near the substrate, but disordered and fluid-like far from it.

The present work resolves this apparent contradiction by systematically simulating silane SAMs on silica, varying the coverage, the substituent length (DTS as opposed to OTS), and the dispersive interaction energy between the substituents and the substrate. It is thereby established under which conditions the self-assembled monolayer is highly ordered and how the tilt angle and the other geometric properties relate to each other. In the future, this approach could replace the oversimplified models which are today commonly used for that purpose.

To evaluate the morphology of the silane SAMs, MD simulations were performed in the isothermal-isobaric ensemble at $T = 298$ K and $p = 1$ bar, using the *GROMACS 4* simulation package [191]. The supporting substrate was modeled as a flat β -cristobalite (1 0 1) surface, normal to the y axis, with the dimensions 11.5×11.1 nm² and a thickness of about 2.3 nm. The cristobalite crystal structure is well suitable as a model for the substrate surface of functionalized silica, since the superficial hexagonal arrangement of oxygen atoms and the superficial oxygen-oxygen distance in cristobalite are known to be similar to amorphous silica

[192]. The density of surface reactive groups, i.e. silanols, is 5.52 nm^{-2} , which is therefore also the maximal coverage here.

To simulate alkylsilane SAMs with a coverage between 1.0 and 5.52 nm^{-2} , the corresponding number of DTS or OTS molecules was bonded to randomly selected oxygen atoms on the top side of the substrate. In Fig. 3.5, the DTS substituent positions are highlighted for the case of a coverage of $\Gamma = 4.5 \text{ nm}^{-2}$. The large grafting densities obtained experimentally indicate that there are few, if any, multiple bonds of each molecule with the substrate, and a low number of cross-linking bonds between silane molecules. Therefore, the study was limited to the simplest case: A single covalent bond per substituent, where the chlorine atoms are substituted by OH groups, and no cross-linking. Periodic boundary conditions were used in all directions, and the height of the simulation box (in y direction) was 10 nm , which is sufficient to avoid interactions of the monolayer with the opposite side of the periodic image of the substrate.

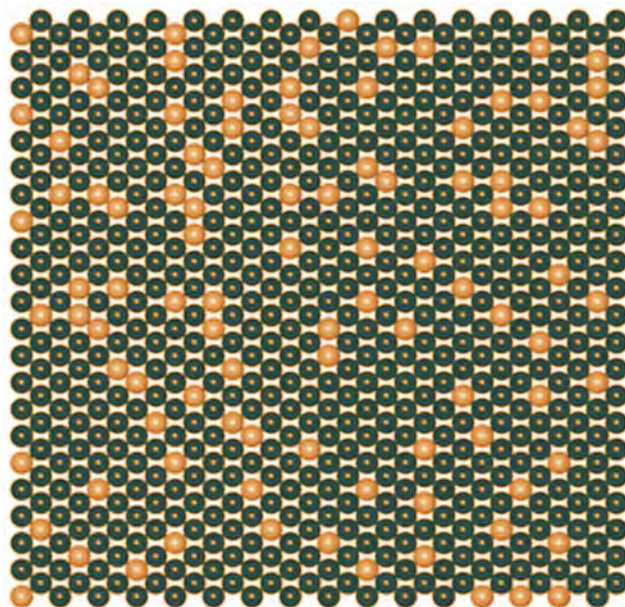


Figure 3.5: Arrangement of the oxygen atoms at a β -cristobalite (1 0 1) surface, where the minimum oxygen-oxygen distance is about 4.4 \AA . In the present case, the coverage is $\Gamma = 4.5 \text{ nm}^{-2}$ and therefore smaller than the superficial density of oxygen atoms, which is 5.52 nm^{-2} . Oxygen atoms represented by dark bullets are bonded to an alkylsilane molecule, whereas light bullets correspond to unsubstituted oxygen atoms.

The OPLS all-atom force field [193] was used for describing the interatomic interactions here, with additional potential parameters and partial charges for modelling the silica bulk [194]. LJ potentials were truncated at a cutoff radius of 1.5 nm , and the long-range contribution of the electrostatic interactions to the interatomic forces was computed with the particle-mesh Ewald method. In the OPLS potential, the LJ interaction between unlike atoms is defined by

a geometric combination rule in the σ parameter, i.e. by using the combination rule

$$\sigma_{ij} = \sqrt{\sigma_i \sigma_j}, \quad (3.9)$$

instead of Eq. (1.7). For the ϵ parameter, the modified Berthelot rule was used, cf. Eq. (1.8). The binary interaction parameter ξ was generally equal to 1, except in a series of simulations in which that factor was varied for the interaction between substituent and substrate atoms.

The initial system configuration was first subjected to an energy minimization using the conjugated gradient method. Subsequently, the system was equilibrated over 11 ns, and production runs were performed for 10 ns. Geometric properties that are commonly used to characterize silane SAMs were determined by post-processing the MD trajectories from the production runs. This includes the thickness, the roughness, and further morphological aspects. Thereby, the relative value of a property is defined as its actual value divided by the maximum value that it can take. The carbon beads of the alkylsilane molecules are numbered consecutively here such that bead 1 is the carbon atom directly bonded to the substrate, and beads 12 and 18 are the terminal carbon atoms of DTS and OTS, respectively. The roughness is defined as the standard deviation of the thickness [195], and the definitions of the tilt angle θ , the twist angle ψ , and the orientation angle ϕ , are illustrated in Fig. 3.6.

Error bars were determined as simple standard deviations, using block analysis. In simulations of large, complex systems like the present one, the relaxation time may become extremely long. However, system properties were calculated here over different time intervals, accounting for a simulation time of at least 40 ns. The values changed only slowly with time, and usually only within the error bars. The deviation between the conformations reached in the present simulations and the thermodynamic equilibrium state was thus found to be insignificant.

The SAM layer thickness ℓ is a property that is available from ellipsometry analysis as well as other experimental methods. However, X-ray reflectivity and infrared spectroscopy yield contradicting values in the measured layer thickness [196]. There is some discussion on how to interpret the experimental layer thickness from an atomistic point of view. Typically, it is defined as the average distance between the oxygen atom of the substrate bonded to the alkylsilane molecule and the topmost atom of its hydrocarbon tail, projected in the direction normal to the surface.

With this definition, the maximum layer thickness possible with the model used in this work is 1.77 nm for DTS and 2.54 nm for OTS. Experimental studies at high coverage report layer thicknesses between 2.4 and 2.7 nm for OTS, while for DTS, the layer thickness is reported to be about 1.4 nm [197, 198].

It is also possible to measure the thickness of the hydrocarbon chain of the molecules, or tail thickness. The tail thickness ℓ^t is equal to the average distance normal to the surface between

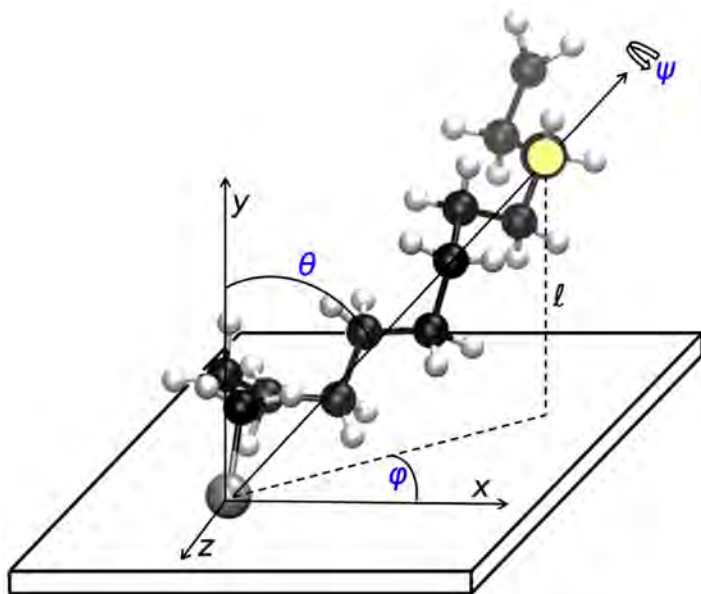


Figure 3.6: Geometric parameters describing the orientation of an alkylsilane molecule attached to a surface normal to the y axis, measured as a function of a selected carbon atom. The selected atom, i.e. the tenth carbon atom of a DTS substituent here, is marked by a yellow bullet. The molecular axis for the selected atom is defined as the axis joining that atom with the silicon atom of the molecule. Black, carbon atoms; light grey, hydrogen atoms; dark grey, silicon atom. ℓ , distance to the surface (see text for different possible definitions of the thickness); θ , tilt angle between the molecular axis and the y axis; ψ , twist angle: rotational angle around the axis of the alkylsilane molecule, which is equal to zero when the distance of the first carbon bead to the surface is maximal; ϕ , orientational angle between the projection of the molecular axis on the surface and the x axis. By convention, all angles are defined counterclockwise, looking down from the substituents to the substrate.

the silicon atom of the alkylsilane molecule, and the topmost atom of its hydrocarbon tail. With this definition, ℓ^t is always smaller than the layer thickness ℓ . In the OPLS model, the maximum tail thickness ℓ_{\max}^t is 1.49 nm for DTS and 2.25 nm for OTS.

Fig. 3.7 compares the relative tail thickness ℓ^t/ℓ_{\max}^t from simulation with experimental data, as a function of coverage Γ , for both DTS and OTS SAMs. Corroborating the experimental results [198], with increasing coverage, the thickness is found to increase monotonically in the present simulations as well. At equal coverage, the relative tail thickness is the same for DTS and OTS. It is well represented by the quadratic correlation

$$\frac{\ell^t}{\ell_{\max}^t} = -0.031 \left(\frac{\Gamma}{\text{nm}^{-2}} \right)^2 + 0.370 \frac{\Gamma}{\text{nm}^{-2}} - 0.117, \quad (3.10)$$

except in the case of very low coverage, i.e. $\Gamma \leq 1 \text{ nm}^{-2}$, which is not the focus of the present study, however. The OTS roughness is always larger than the roughness of DTS except at very high coverage. As OTS is a longer molecule than DTS, the differences in local thickness can

be larger. The roughness has a maximum at intermediate coverage, and the OTS maximum occurs at lower coverage than for DTS. Since the tail thickness is a property which is easier to measure than the coverage, Eq. (3.10) can be used to estimate the coverage of a given sample from experimental data on the tail thickness of the SAM.

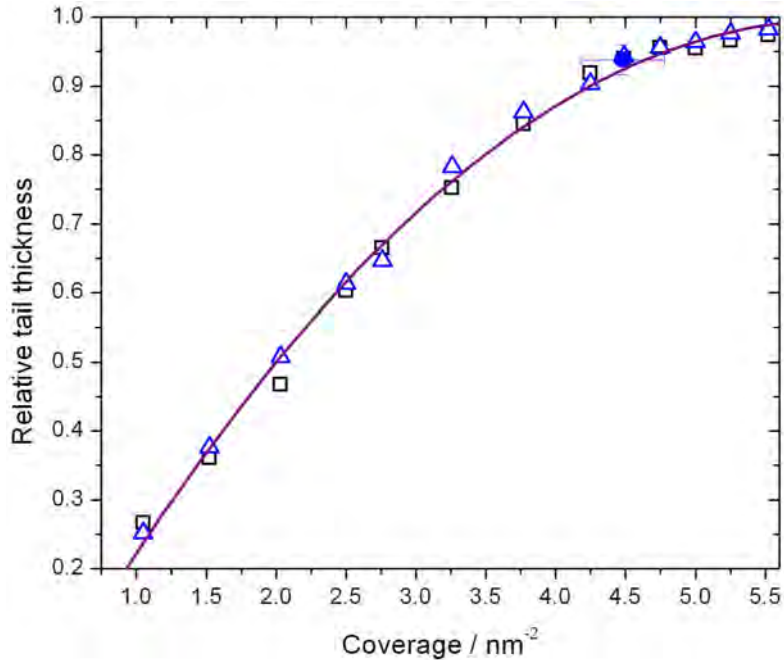


Figure 3.7: Relative tail thickness as a function of coverage: Present molecular simulation results for DTS (squares) and OTS (triangles), and experimental data for OTS (bullet), cf. Tidswell *et al.* [199]; line, quadratic fit, cf. Eq. (3.10). Error bars for simulation data are within symbol size.

Experimentally, the tilt angle θ is usually indirectly determined from the relative thickness of the monolayer. This method is not very precise, especially at the small angles found at large coverage [200]. It is clear that the tilt angle must be related to the coverage, and there have been attempts to find an explicit relationship between these properties [201, 202]. Fig. 3.8 contains the present simulation results, which shows a quadratic dependence of the tilt angle on the coverage,

$$\theta = 1.86^\circ \left(\frac{\Gamma}{\text{nm}^{-2}} \right)^2 - 29.5^\circ \frac{\Gamma}{\text{nm}^{-2}} + 108^\circ. \quad (3.11)$$

Similar to Eq. (3.10), this equation describes how an morphological property of the SAM, in this case the tilt angle, does not depend on the length of the alkylsilane molecule. Therefore, differences in the tilt angle between DTS and OTS substituents in experiments, performed at similar conditions, point to differences in coverage. As above, Eq. (3.11) is only valid for $\Gamma > 1 \text{ nm}^{-2}$. Experimental data at high coverage indicate a tilt angle lower than 20° for OTS, in good agreement with the simulation results, cf. Fig. 3.8. In particular, the simulated tilt angle is lower than 15° at the highest coverage, corroborating the work of Tillman *et al.* [203].

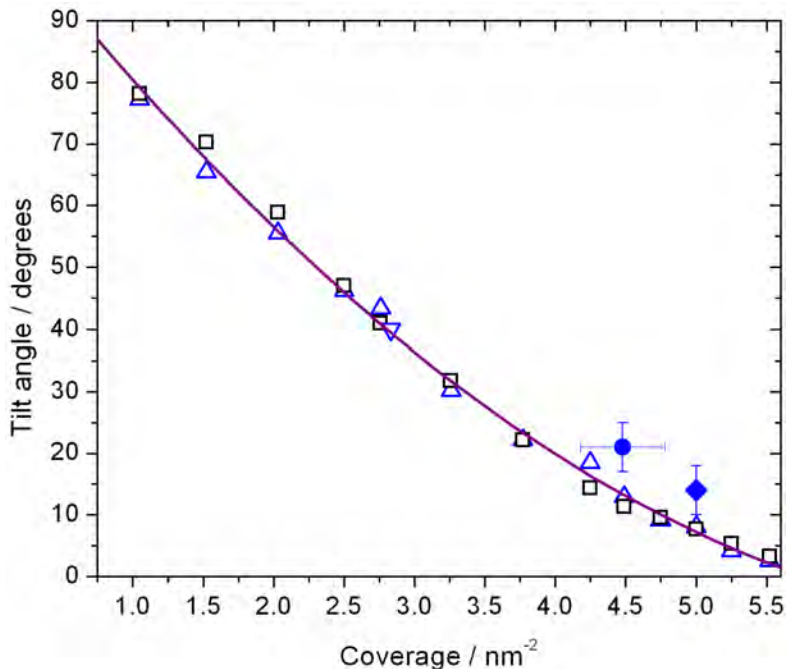


Figure 3.8: Tilt angle θ as a function of coverage: Present molecular simulation results for DTS (squares) and OTS (triangles); line, quadratic fit, cf. Eq. (3.11). Error bars are within symbol size. Experimental data (closed symbols) and simulation results from the literature (open symbols) for OTS are also shown: Bullet, Tidswell *et al.* [199]; diamond, Tillman *et al.* [203]; triangle down, Kaushik and Clancy [204].

A quadratic relationship is also found between the relative tail thickness and the tilt angle

$$\theta = -37.8^\circ \left(\frac{\ell^t}{\ell_{\max}^t} \right)^2 - 51.9^\circ \frac{\ell^t}{\ell_{\max}^t} + 92.6^\circ, \quad (3.12)$$

cf. Fig. 3.9. If the alkylsilane chains were completely rigid, the curve describing this relationship should instead be given by the arccosine function. Most of the experimental data from the literature appear to confirm an arccosine-like dependency. In these cases, however, chain rigidity is used as an assumption underlying the interpretation of the measurements, e.g. when the tilt angle is calculated from the tail thickness determined by ellipsometry. This also explains the deviation (of the order of 10°) found between experimental and simulated tilt angles here.

A further series of simulations was performed in which the binary interaction parameter ξ from the modified Berthelot rule, cf. Eq. (1.8), was varied between 0.1 and 1.4 for the interactions between the alkylsilane molecules and the substrate. In Fig. 3.10, the results for the layer thickness are plotted as a function of ξ at low and high coverage. At high coverage, there is hardly any influence of the unlike interaction on the layer thickness, as the molecules arrange approximately perpendicular to the substrate and interact weakly with it.

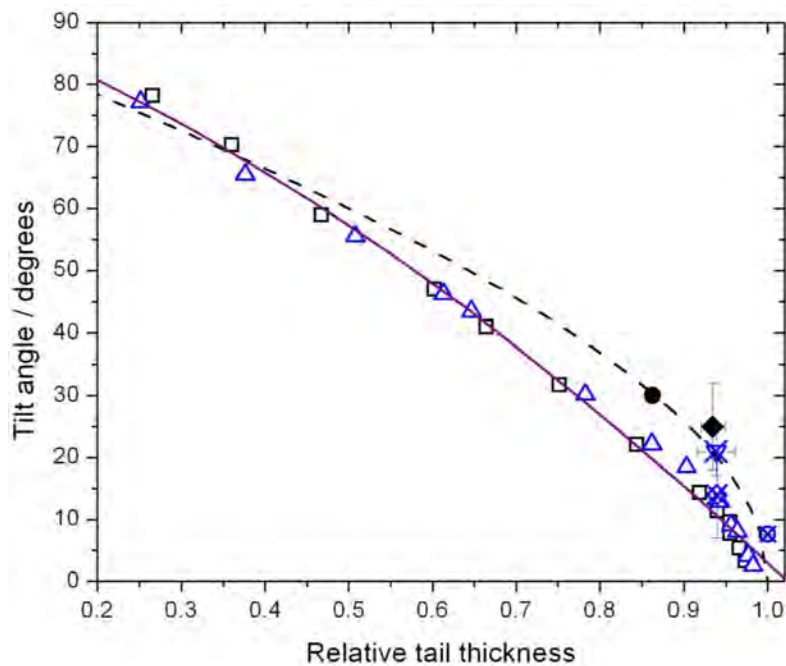


Figure 3.9: Tilt angle θ as a function of the relative tail thickness ℓ^t/ℓ_{\max}^t . Present simulation results for DTS (squares) and OTS (triangles); dashed line, arccosine function; solid line, quadratic fit, cf. Eq. (3.12); experimental data for DTS (closed symbols) and OTS (crossed symbols) by Gutfreund *et al.* [188] (circle), Lessel *et al.* [185] (diamond), and Tidswell *et al.* [199] (triangle down).

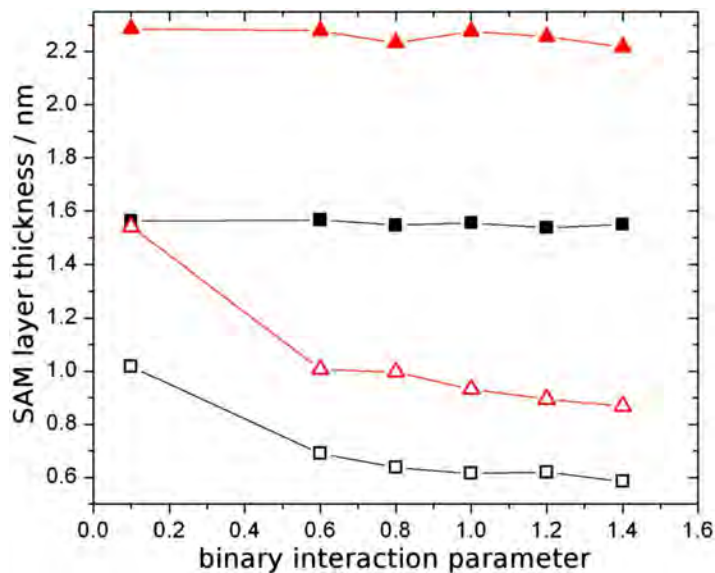


Figure 3.10: SAM layer thickness as a function of the binary interaction parameter of the modified Berthelot rule, cf. Eq. (1.8), for the substituent-substrate LJ potential. Results for DTS (squares) and OTS (triangles) at a coverage of $\Gamma = 1.5$ (open symbols) and 4.5 nm^{-2} (closed symbols). Error bars are within symbol size in all cases.

Even at low coverage, the influence of the binary interaction parameter on the layer thickness remains insignificant, except for extreme parameter choices, i.e. when ξ deviates from unity by more than 50 %. However, typical binary interaction coefficients, which were e.g. adjusted to experimental VLE data, are rarely smaller than 0.9 or greater than 1.1. It can thus be concluded that the inter-chain interactions determine the geometrical properties of the monolayer. The precise value of ξ is of minor importance here and cannot be adjusted to experimental data on the tilt angle or the SAM layer thickness.

4 Scalable molecular simulation software

4.1 Large systems in molecular dynamics

For the development of MD codes, as for any software, there are trade-offs between generality and optimization for a single purpose, which no particular implementation can completely evade.¹ Several popular MD simulation environments are tailored for studying biologically relevant systems, with typical application scenarios including conformational sampling of macromolecules in aqueous solution. The relaxation processes of such systems are often several orders of magnitude slower than for simple fluids, requiring an emphasis on sampling techniques and long simulation times, but not necessarily on large systems.

The *AMBER* package [206], for instance, scales well for systems containing up to 400 000 molecules, facilitating MD simulations that reach the microsecond time scale [51]. Similarly, *GROMACS* [191] and *NAMD* [26], which also have a focus on biosystems, have been shown to perform efficiently on modern HPC architectures. *Tinker* was optimized for biosystems with polarizable force fields [207], whereas *CHARMM*, which was co-developed by Nobel prize winner Martin Karplus, is suitable for coupling classical MD simulation of macromolecules with quantum mechanics [208].

A different tendency is represented by codes such as *DL_POLY* [23] or *LAMMPS* [209], which scale well for homogeneous fluid systems with up to tens of millions of molecules, or *ESPResSo*, which emphasizes its versatility and covers both molecular and mesoscopic simulation approaches [30]. These are highly performant codes which aim at a high degree of generality, including many classes of pair potentials and methods. The *IMD* code, which has held the MD simulation world record in terms of system size previously [28], has a focus on multi-body potentials for solids.

The novel MD simulation code *ls1 mardyn* (large systems 1: molecular dynamics) expands the temporal and spatial range of scales accessible to molecular simulation, with a focus on inhomogeneous systems (e.g. at interfaces) and non-equilibrium thermodynamics. In many relevant cases, such as those involving vapour-liquid coexistence, the molecule distribution may be very heterogeneous and change over time in an unpredictable way (e.g. during phase

¹This section is based on Horsch *et al.* [2] and Niethammer *et al.* [205].

decomposition or multi-phase flow). The design of *ls1 mardyn* is oriented towards three major objectives: Modularity of the structure, interdisciplinary collaboration within the development process, and transferability of the code base to diverse and heterogeneous HPC architectures.

Beside the LJ potential, *ls1 mardyn* supports point charges and higher-order point polarities up to second order (i.e. dipoles and quadrupoles), modelling electrostatic interactions in terms of a multipole expansion [210]. Furthermore, the Tersoff potential [211] can be used for a variety of solid materials [212]. The latter, as a multi-body potential, is computationally more expensive than the pair potentials for fluids. In each integration time step, the intermolecular interactions are evaluated, from which the resulting force and torque acting on each molecule is obtained by summation. Newton's equations of motion are solved numerically for all molecules to obtain the configuration in the next time step. For this purpose, *ls1 mardyn* employs the leapfrog method, which is algebraically equivalent to the Verlet method but more accurate numerically, cf. Section 1.2.

Any system of units can be used in *ls1 mardyn* as long as it is algebraically consistent and includes the Boltzmann constant as well as the Coulomb constant among its basic units. Thereby, expressions for quantities related to temperature and the electrostatic interactions are simplified. The units of size, energy and charge are related (by Coulomb's law and the Coulomb constant unit) and cannot be specified independently of each other. The system of units is then expanded algebraically; for an example, see Tab. 4.1.

Table 4.1: A consistent set of atomic units (used by *ls1 mardyn* scenario generators).

Boltzmann constant	$k_B = 1.38065 \times 10^{23} \text{ J/K} = 1$
Coulomb constant	$(4\pi\epsilon)^{-1} = 8.98755 \times 10^9 \text{ Jm/C}^2$
Unit length	$\ell_1 = 1 R^B$ (Bohr's radius) $= 5.29177 \times 10^{-11} \text{ m}$
Elementary charge	$q_1 = 1 e = 9.64854 \times 10^9 \text{ C/mol}$
Unit mass	$m_1 = 1 \text{ kg/mol}$
Unit density	$\rho_1 = 1/\ell_1^3 = 11\,205.9 \text{ mol/l}$
Unit temperature	$T_1 = q_1^2/(4\pi\epsilon\ell_1) = 315\,775 \text{ K}$
Unit pressure	$p_1 = \rho_1 T_1 = 2.94211 \times 10^{13} \text{ Pa}$
Unit time	$t_1 = \ell_1 \sqrt{m_1/T_1} = 3.26585 \times 10^{-14} \text{ s}$
Unit velocity	$v_1 = \ell_1/t_1 = 1620.35 \text{ m/s}$
Unit dipole moment	$D_1 = \ell_1 q_1 = 2.54176 \text{ D}$
Unit quadrupole moment	$Q_1 = \ell_1^2 q_1 = 1.34505 \text{ D}\text{\AA}$

Calculating short range interactions in dynamic systems requires an efficient algorithm for finding neighbours. For this purpose, *ls1 mardyn* employs an adaptive linked-cell algorithm [213]. The basic linked-cell algorithm divides the simulation volume into a grid of equally sized cubic cells, which have an edge length equal to the cutoff radius r^c . This ensures that all interaction partners for any given molecule are situated either within the cell of the molecule

itself or the 26 surrounding cells. Nonetheless, these cells still contain numerous molecules which are beyond the cutoff radius. The volume covered by 27 cells is $27 (r^c)^3$, whereas the relevant volume containing the interaction partners is a sphere with a radius r^c , corresponding to $4\pi(r^c)^3/3 \approx 4.2 (r^c)^3$. Thus, in case of a homogeneous configuration, only 16% of all pairs for which the distance is computed are actually considered for intermolecular interactions.

For fluids with computationally inexpensive pair potentials, e.g. molecules modeled by a single LJ site, the distance evaluation requires approximately the same computational effort as the force calculation. Reducing the volume which is examined for interaction partners can therefore significantly reduce the overall runtime. This can be achieved by using smaller cells with an edge length of e.g. $r^c/2$, which reduces the considered volume from $27 (r^c)^3$ to $15.6 (r^c)^3$, so that for a homogeneous configuration, 27% of the computed distances are smaller than the cut-off radius. However, smaller cells also carry an overhead effort, since 125 instead of 27 cells have to be traversed. This is only beneficial for regions with high density, where the cost of cell traversal is small compared to the cost of distance calculation. Many applications of molecular dynamics, such as processes at interfaces, are characterized by a heterogeneous distribution of the molecules and thus by a varying density throughout the domain. To account for this, adaptive cell sizes depending on the local density [213] are (optionally) used by *lsI mardyn* as illustrated by Fig. 4.1.

Molecular simulations with system dimensions that far exceed the cut-off radius, beyond which a mean-field approach is employed for the intermolecular interactions, are most efficiently parallelized by space decomposition schemes. Thereby, the simulation volume is subdivided into smaller subvolumes (one for each process) that ideally carry the same load [214]. Finding an optimal balance requires a method that estimates the load corresponding to the possible decompositions on the fly, since the particle density distribution can vary significantly over simulation time. In *lsI mardyn*, an interface class for the domain decomposition scheme permits the generic implementation of different load balancing strategies operating on spatial subdomains.

On the basis of the computational cost for each of the cells, load balancing algorithms can group the linked cells together such that n^p subvolumes with approximately equal load are created, where n^p is the number of processing units. A hierarchical tree-based approach (similar to k -dimensional trees) turned out to be the most adequate dynamic load balancing method; this concept was previously known to be suitable for parallelizing particle-based simulations with short-range interactions [214]. Thereby, the simulation volume is recursively bisected by planes with alternating orientation (normal to the x , y , z , x , \dots axes). This process is repeated until each process is assigned one cuboid subdomain. The implementation in *lsI mardyn* requires each subvolume to cover at least two cells in each spatial dimension.

In a typical simulation, the largest part of the computational cost is caused by the force and distance calculations. If N_k and N_l denote the number of molecules in cells k and l , respec-

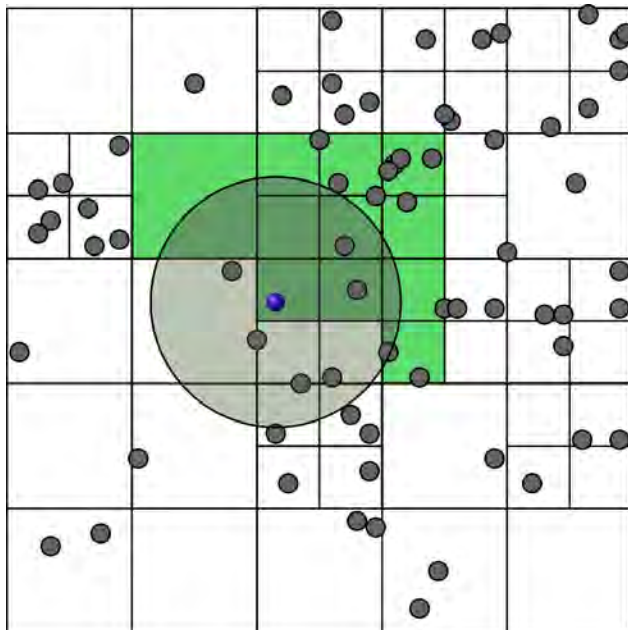


Figure 4.1: Adaptive cell sizes for an inhomogeneous molecule distribution. Cells that contain significantly more molecules than others are divided into smaller subcells. According to Newton’s third law, i.e. *action equals reaction*, two interacting molecules experience the same force (in opposite directions) due to their mutual interaction, so that a suitable enumeration scheme can be employed to reduce the amount of cell pairs that are taken into account. Following such a scheme, it is sufficient to compute the force exerted by the highlighted molecule on molecules from the highlighted cells [213].

tively, the number of distance calculations $n_r(k)$ for cell k can be estimated by

$$n_r(k) \approx \frac{N_k}{2} \left(N_k + \sum_{l \in \mathbb{V}(k)} N_l \right). \quad (4.1)$$

The first term in Eq. (4.1), i.e. $N_k^2/2$, corresponds to the distance calculations within cell k . The second term represents the calculation of distances between molecules in cell k and one of the cells $l \in \mathbb{V}(k)$ in the vicinity of k .

While Eq. (4.1) can be evaluated with little effort, it is far more demanding to predict the number of force calculations. Furthermore, communication and computation costs at the boundary between adjacent subdomains allocated to different process can be significant. They depend on many factors, in particular on the molecule density at the boundary. Therefore, even if the load on all compute nodes is uniform and remains constant, the location of the subvolume boundaries has an influence on the overall performance. For a discussion of detailed models for the respective computational costs, the reader is referred to Buchholz [213]. In the present version of *ls1 mardyn*, the computational costs are estimated on the basis of the number of necessary distance calculations per cell, approximated by Eq. (4.1).

With this technique, an excellent scalability was obtained even for heterogeneous scenarios on up to 10^5 processing units of the *hermit* supercomputer at the High Performance Computing Centre Stuttgart (HLRS), cf. Figs. 4.2 and 4.3. The following scenarios, cf. Fig. 4.2, using the internal scenario generators of *ls1 mardyn*, were scaled up by varying the number of molecules N , and simulated over 1 000 time steps with disengaged final input/output:

- **Bulk:** Homogeneous liquid ethylene oxide at a density of $\rho = 16.9$ mol/l and a temperature of $T = 375$ K. The molecular model for ethylene oxide consists of three LJ sites and one point dipole [14].
- **Droplet:** Simulation scenario containing a LJTS nanodroplet surrounded by supersaturated vapour at a temperature of $T = 0.95 \epsilon$.
- **Planar:** Simulation of a planar vapour-liquid interface of the LJTS fluid at a temperature of $T = 0.95 \epsilon$.

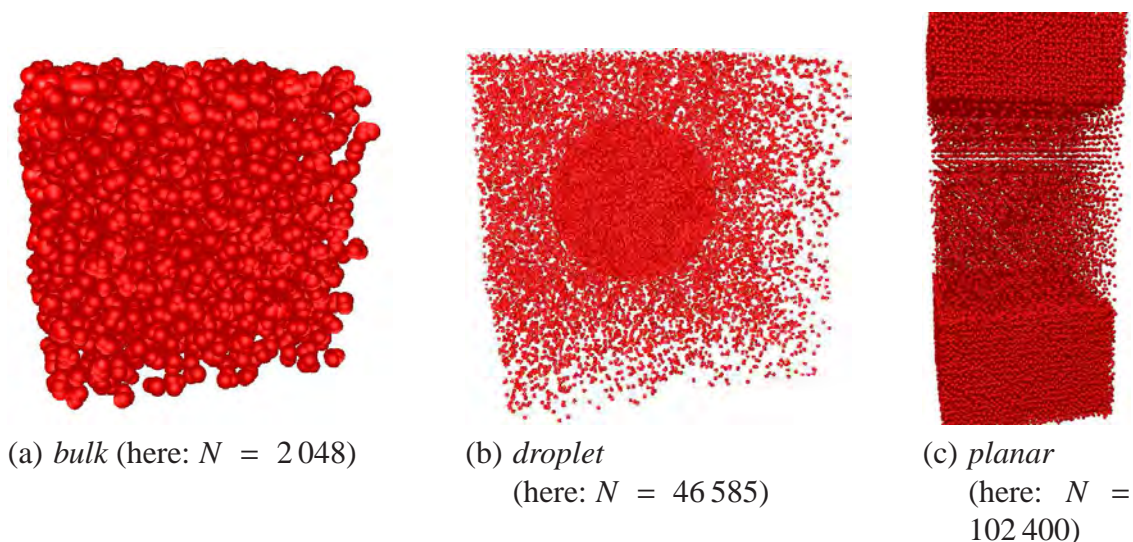


Figure 4.2: Scenarios used during the performance evaluation of *ls1 mardyn*.

Parallelization is associated with additional complexity due to communication and synchronization between the different execution paths of the program. In comparison with sequential execution on a single processing unit, this introduces an overhead. To determine the magnitude of this overhead for *ls1 mardyn*, the *planar* scenario with $N = 102\,400$ LJ sites was executed on *hermit*, both with the sequential and the MPI parallel version of the code, using only a single process in each case. Execution of the sequential program took 530.9 s, while the MPI parallel version took 543.4 s. This indicates that the overhead due to imperfect concurrency amounts to around 2% only.

In addition to comparing the run times, the effectiveness of the dynamic load balancing implementation in *ls1 mardyn* is supported by traces revealing the load distribution between the processes. Fig. 4.4 shows such traces, generated with *vampirtrace*, for 15 processes of a

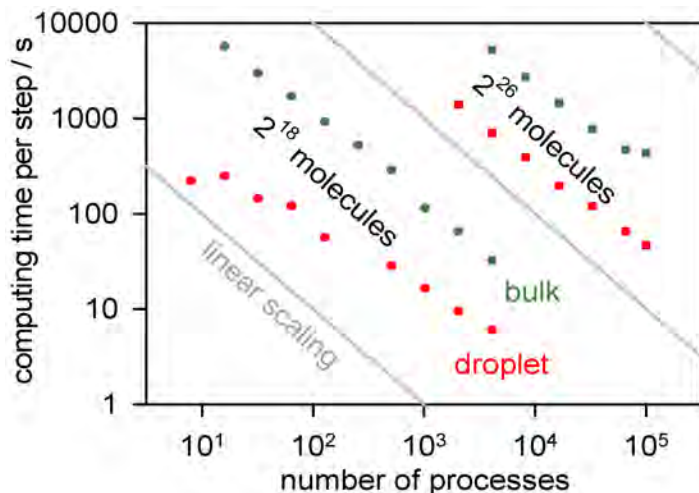


Figure 4.3: Strong scaling of the *ls1 mardyn* program on the *hermit* supercomputer for homogeneous (bulk) and heterogeneous (droplet) scenarios.

droplet scenario simulation on the *hermit* supercomputer. For a trivial domain decomposition, where all processes are assigned equal volumes, 12 out of 15 processes are waiting in MPI routines most of the time, while the remaining three processes have to carry the bulk of the actual computation. In contrast, the present tree-based decomposition exhibits a more balanced distribution of computation and communication.

It can therefore be summarized that *ls1 mardyn*, which is publicly available as free software,² represents the state of the art in MD simulation. It can be recommended for large-scale applications, and particularly for processes at fluid interfaces, where highly heterogeneous and time-dependent density distributions may occur. Due to the modularity of its code base, future work can adjust *ls1 mardyn* to newly emerging HPC architectures and further extend the range of available molecular modelling approaches and simulation methods.

4.2 Scalable multi-trillion molecule MD simulation

Despite the development of molecular simulation for over half a century, scientists still strive for ever larger and longer simulation runs to cover processes on greater length and time scales.³ Due to the massive parallelism that large-scale MD typically exhibits, it is a pre-eminent task for high-performance computing. To enable a simulation breaking the MD world record, the code *ls1 mardyn* was optimized for the SuperMUC cluster at the Leibniz Supercomputing Centre. Based on the further development of the memory optimization described by Eckhardt and Neckel [216], an extremely low memory requirement of only 32 bytes per molecule was achieved.

²<http://www.ls1-mardyn.de/>

³This section is based on Eckhardt *et al.* [215].



(a) Equivoluminar domain decomposition



(b) Tree-based domain decomposition

Figure 4.4: Traces for the *droplet* scenario on *hermit*, generated with *vampirtrace*. The program state over two time steps is shown for 15 parallel processes. Computation is indicated by blue colour, communication by red colour. Vertical lines indicate message passing between processes.

The present work continues a series of efforts towards extreme-scale MD simulation. In 2000, Roth *et al.* [28] performed a simulation of 5×10^9 molecules, the largest simulation ever at that time. Kadau *et al.* [217] as well as Germann and Kadau [218] followed up, establishing the world record at $N = 10^{12}$ molecules. These simulations demonstrated the state of the art on the one hand, and showed the scalability and performance of the respective codes. Subsequently, Kabadshow *et al.* [219] evaluated the intermolecular forces for a configuration containing 3×10^{12} molecules, however, without integrating the equations of motion.

In accordance with preceding large-scale simulations [218], single-precision variables are used here for the computation. For each molecule, only its position (3×4 bytes), velocity (3×4 bytes), and an identifier (8 bytes) are stored, i.e. 32 bytes in total. All molecule data are stored in dynamic arrays, i.e. contiguous memory blocks, assigned to the respective linked cells, to avoid additional memory for pointers. Thus, the organization of the linked-cells data structure causes only a small overhead. The force vector does not need to be stored permanently, because the time integration of the equations of motion is carried out on the fly, as detailed in Section 1.2.

The *ls1 mardyn* code was optimized on the micro-architecture level for a specific processor: The Intel Sandy Bridge EP, and in particular the SuperMUC cluster operated by the Leibniz Supercomputing Centre in Garching. This system features 147 456 cores with a theoretical double precision peak performance of more than 3 PFLOPS, and at the time when the simulations were carried out (in 2013), it was the biggest x86 system worldwide. The system was assembled by IBM and features a highly efficient hot-water cooling solution. In contrast to supercomputers offered by Cray, SGI or even IBM's own BlueGene, the machine is based on a high-performance network: A FDR-10 infiniband pruned-tree topology by Mellanox. Each of the 18 leafs, or islands, consists of 512 nodes with 16 cores at 2.7 GHz clock speed (turbo mode is disabled) sharing 32GB of main memory. Within one island, all nodes can communicate at full FDR-10 data-rate. In case of inter-island communication, four nodes share one uplink to the spine switch. Since the machine is operated without hard disks, a significant fraction of the node memory has to be reserved for the operation environment.

The main innovation of the Intel Sandy Bridge EP processor, introduced in January 2012, is the advanced vector extensions (AVX) instruction set. In order to execute code with high performance and to increase the number of instructions per clock, major changes were applied to the previous core micro-architecture, which was called Nehalem by Intel internally. The changes are highlighted by italic characters in Fig. 4.5. Since the vector-instruction width has been doubled with AVX (which is available with two vector widths: AVX128 and AVX256), also the load port (i.e. port 2) width needs to be doubled. However, doubling a load port width would impose tremendous changes on the entire chip architecture. In order to avoid this, Intel changed two ports by additionally implementing in each port the other port's functionality as shown for ports 2 and 3. Through this trick, the load bandwidth has been doubled from 16 bytes to 32 bytes per cycle at the price of reduced instruction-level parallelism.

Changes to the ALUs were straightforward: Ports 0, 1 and 5 were simply doubled, and they provide the classical SSE functionality for AVX instructions and extensions for blend and mask operations. However, this bandwidth improvement still does not allow for an efficient exploitation of AVX256 instructions, as this would require a load of 64 bytes per cycle and a bandwidth of 32 bytes per cycle. (This increase will be implemented with the up-coming Haswell micro-architecture.) Due to these boundary conditions, AVX128 codes can often yield the same performance as AVX256 on Sandy Bridge, while they are much better than SSE4.2 on an equally clocked Nehalem chip. This can also be attributed to the fact that 16-byte load instructions have a three times higher throughput (0.33 cycles) than 32-byte load instructions (here, ports 2 and 3 have to be paired and cannot be used independently).

With AVX, a register allocation in each compute unit of the core would be too expensive in terms of transistors required, and therefore, a *register file* was implemented: Register contents are stored in a central directory. Shadow registers and pointers allow for an efficient out-of-order execution. Furthermore, a general performance enhancement was added to the

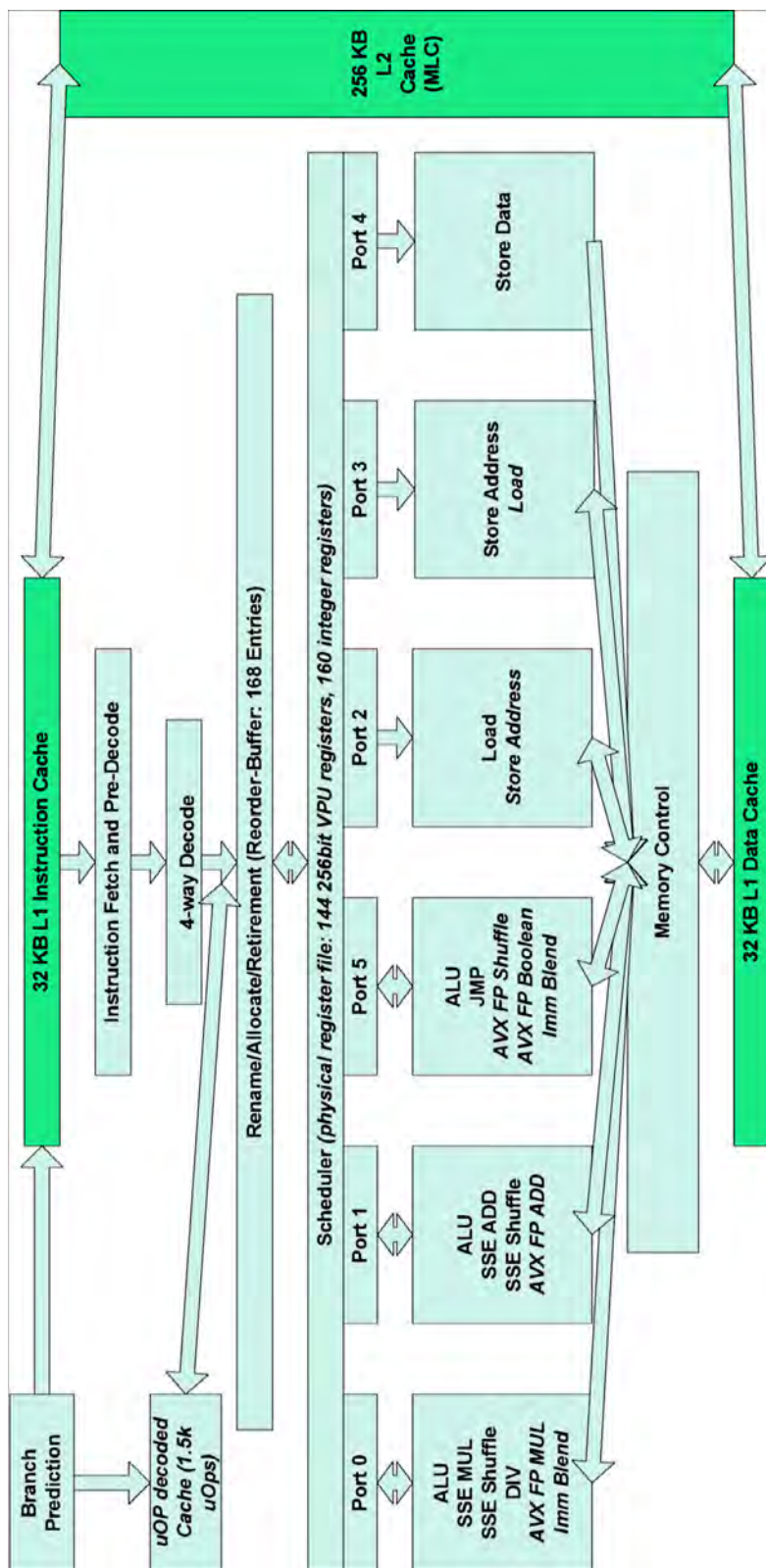


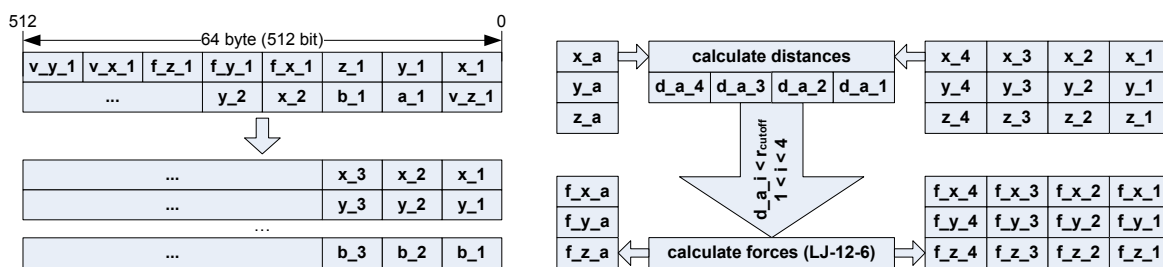
Figure 4.5: The Intel Sandy Bridge architecture. Changes with respect to the Intel Nehalem architecture are highlighted by italic characters: Trace cache for decoded instructions, AVX support, and physical register file.

Sandy Bridge architecture: A cache for decoded instructions, boosting the performance of kernels with small loop bodies, such as the force calculation in MD. Furthermore, the Sandy Bridge EP cores feature Intel’s hyperthreading technology which helps to increase the core’s utilization in workload scenarios where the instruction mix is not optimal or the application is suffering from high memory latencies.

Since *ls1 mardyn* is written in C++ and therefore applies standard object-oriented design principles, with cells, molecules, etc. as objects, the approach developed by Eckhardt and Heinecke [220] is followed concerning memory organization and vectorization: By using a simple proxy application and not the entire *ls1 mardyn* code base, the LJ-12-6 force calculation inside a linked cell algorithm can be vectorized on x86 processors. For the present work, the previous implementation was extended by the potential energy and the virial.

The object-oriented memory layout is cache-efficient by design, because molecules belonging to a cell are stored closely together. However, implementing molecules in a cell as an *array of structures* (AoS) forbids easy vectorization, at least without gather and scatter operations, which are not available on Intel Sandy Bridge. Only in simple cases (such as updating a single molecule) this drawback does not matter, because prefetch logic inside the hardware loads only cache-lines containing data which actually have to be modified.

Implementing the LJ force calculation on arrays of structures poses major challenges: The upper part of Fig. 4.6(a) shows elements scattered across several cache-lines. Taking into account that only a small portion of the members is needed for the force calculation, a temporary *structure of arrays* (SoA) can be constructed to reduce cache-line pollution and increase vectorization opportunities, as illustrated in the lower part of Fig. 4.6(a). Fig. 4.6(b) sketches the vectorization applied to the LJ potential: In contrast to other methods, which vectorize across the spatial coordinates [221, 222], the present approach can exploit vector units of arbitrary length.



(a) *AoS to SoA conversion*: In order to allow for efficient vectorization, corresponding elements have to be stored for data streaming access.

(b) *Kernel vectorization*: The vectorization of the LJ force calculation is optimized by duplicating one molecule and streaming four other molecules.

Figure 4.6: Optimizing LJ force calculation by an SoA storage scheme and vectorization.

In this work, single-precision AVX128 instructions are employed. The calculation is per-

formed on pairs of molecules, therefore the required data of one molecule are broadcast-loaded in the first register, and the second register is filled with data from four other molecules. Dealing with four molecule pairs at once reduces the number of operations by a factor of four, theoretically. Since the force calculation may be required for all, some or none of the pairs in the vector register, pre- and post-processing is required, which is performed by regular logical operations: It has to be determined whether for at least one molecule pair, the distance is smaller than r^c (pre-processing), because only then the force calculation has to be executed. If the force calculation has been executed, the calculated results need to be zeroed by a mask for all molecule pairs whose distance is larger than r^c (post-processing). Intrinsic are used to ensure a vectorization of the kernel. Due to the cutoff-radius *if* condition inside the innermost loop, current compilers (*gcc* and *icc*) deny to vectorize the loop structure iterating over molecules in cell pairs. For the chosen simulation scenario with a cutoff radius of $r^c = 3.5 \sigma$, a speedup of three is possible on a single core by using the proposed SoA structure and vectorization.

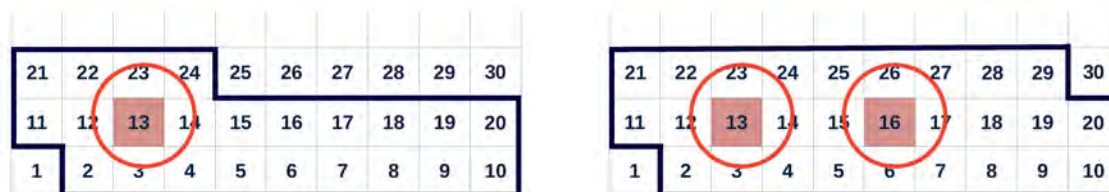
With increasing vector length, this masking technique becomes a major bottleneck. It can then occur that more elements are being masked than computed. Therefore, moving to a wider vector-instruction set may result in more instructions being executed. However, if the vector-instruction set features *gather* and *scatter* instructions, this issue can be overcome because only the molecule pairs taking part in the interaction are processed, which has been successfully demonstrated by Rapaport with the layered-linked-cell algorithm [223].

A different issue inhibiting the efficient usage of the Sandy Bridge core is the lack of instruction-level parallelism in the compute kernel. The evaluation of distances, pair potentials, and forces requires significantly more multiplications than additions, so that the ADD unit cannot be fully utilized. Even worse, the calculation of the repulsive term of the LJ potential requires a sequence of dependent multiplications. Therefore, the superscalarity of a Sandy Bridge core cannot be exploited optimally. The behaviour is improved here, however, by using the hyperthreading technology.

We restricted ourselves to AVX128 instructions for several reasons. Firstly, the Intel Sandy Bridge architecture is not able to handle AVX256 instructions at full speed, and as discussed by Eckhardt and Heinecke [220], AVX256 instructions are only beneficial when the cutoff radius becomes very large. Moreover, AMD Interlagos also plays an important role, since this chip is used as processor in most Cray supercomputers. AMD Interlagos features two 128bit FPUs shared between two integer units. Therefore, an AVX128 code is essential for a good performance on Interlagos. With present code base, only slight changes are required for migrating to an Interlagos machine.

To reduce the memory requirement to only 32 bytes per molecule, the linked-cells algorithm is implemented with a *sliding window*, following the approach of Eckhardt and Neckel [216], which is based on the observation that the access pattern of the cells can be described by a

sliding window that moves through the domain. After a cell has been searched for interacting molecules for the first time in a time step, its data will be required for several successive force calculations with molecules in neighbouring cells. If the force calculation proceeds according to the cell index as depicted in Fig. 4.7, these data accesses happen within a short time period, until the interactions with all neighbours have been computed. While the cells in the window are accessed several times, they naturally move in and out of the window in FIFO order.



- (a) Sliding window in 2D (cells inside the bold frame). Molecules in cells in the window will be accessed several times, cells 2 through 24 are covered by the window in FIFO order. For the force calculation for the molecules in cell 13, cell 24 is searched for interacting molecules for the first time in this iteration. The molecules in cell 2 are checked for the last time for interactions.
- (b) Extension of the sliding window for multi-threading. By increasing the window by five cells, two threads can independently work on three cells each: thread 1 works on cells 13, 14, 15; thread 2 works on cells 16, 17, 18. To avoid that multiple threads work on the same cells simultaneously, a barrier is required after each thread has finished its first cell.

Figure 4.7: Illustration of the sliding-window algorithm and its extension for multi-threading.

Molecule data outside the the sliding window are stored in form of C++ objects in an AoS arrangement, containing only the position, the velocity, and an identifier. In each cell, *Molecule* objects are stored in dynamic arrays. When the sliding window is shifted further and covers a new cell, the positions and velocities of the molecules in that cell are converted to SoA form. Additionally, arrays for the forces have to be allocated. The force calculation is now performed on the molecules as described above. When a cell has been considered for the last time during an iteration, its molecules are converted back to the AoS layout. Therefore, the calculation of forces, potential energy and virial pressure can be performed efficiently using SoA data structures, while the remaining parts of the simulation code can be kept unchanged according to their object-oriented layout. To avoid the overhead of repeated memory (de)allocations when molecule data in a cell are converted, dynamic arrays are allocated initially, leaving enough space for a maximum number of molecules per cell (which can be estimated heuristically from the pair potential). This memory is then reused as the sliding window moves through the subdomain of a single MPI process. Since the sliding window covers three layers of cells, these buffers consume a comparably small amount of memory, while the vast majority of the molecules is stored memory-efficiently. At this point, it becomes apparent that the traversal order imposed by the sliding window also supports cache reuse: When

molecule data are converted to the SoA representation, these data are placed in the cache and will be reused several times soon after.

To reduce the memory requirement to 32 bytes per molecule and to further improve the hardware utilization, two further revisions are necessary: The time integration has to be performed on the fly, and opportunity for multi-threading needs to be created. Since the forces are not stored with the molecule objects, the time integration has to be performed during that conversion, i.e. new velocities have to be computed at that moment. The correct traversal of the molecules is ensured, because cells that have been converted are not required for the force calculation during this time step any more, and the update of the linked-cell data structure, i.e. the assignment of molecules to cells, takes place only between time steps.

To make use of hyperthreading, a lightweight shared-memory parallelization was implemented: By extending the size of the sliding window as shown in Fig. 4.7, two threads can perform calculations concurrently on three independent cells. While exploiting Newton's third law and considering each cell pair only once, it is avoided that threads work on directly neighbouring cells simultaneously. Therefore, a barrier, causing comparably little overhead on a hyperthreading core, is required after each thread has processed a cell. This allows the execution of one MPI rank per core with two OpenMP threads to create sufficient instruction level parallelism, leading to a 12% performance improvement.

To evaluate the present optimized version of *ls1 mardyn*, single-centre LJ molecules were distributed on a regular grid on a body-centered cubic lattice with a density of $\rho = 0.78 \sigma^{-3}$, and the cutoff radius was specified to be $r^c = 3.5 \sigma$. The integration time step was set to $t_\delta = 1$ fs. For the MPI parallelization, an equivoluminar spatial domain decomposition was employed, which is appropriate for a homogeneous fluid scenario.

Multiple series of test simulations were carried out on the SuperMUC supercomputer. With respect to strong scaling behaviour, a scenario with $N = 4.8 \times 10^9$ molecules is considered, which perfectly fits onto 8 nodes; 18 GB per node are needed for molecule data. Fig. 4.8 shows that a very good scaling was achieved for up to 146 016 cores using 292 032 threads at a parallel efficiency of 42 % (comparing 128 to 146 016 cores).

In this case, less than 20 MB (5.2×10^5 molecules) of main memory were used per node, which fits well into the cache of the individual processors. The excellent scaling behaviour of *ls1 mardyn* can be explained by analysing Fig. 4.9. Therein, results are shown concerning the achievable GFLOPS, depending on the number of molecules, from simulations on eight nodes. Already for $N = 3 \times 10^8$ molecules, occupying approximately 8 % of the available memory, a performance of roughly 550 GFLOPS is reached. The same performance is also obtained for $N = 4.8 \times 10^9$ molecules.

The present weak-scaling analysis, cf. Fig. 4.8, also includes the multi-trillion test case, breaking the MD world record. Thereby, due to MPI buffers on all nodes, the number of molecules

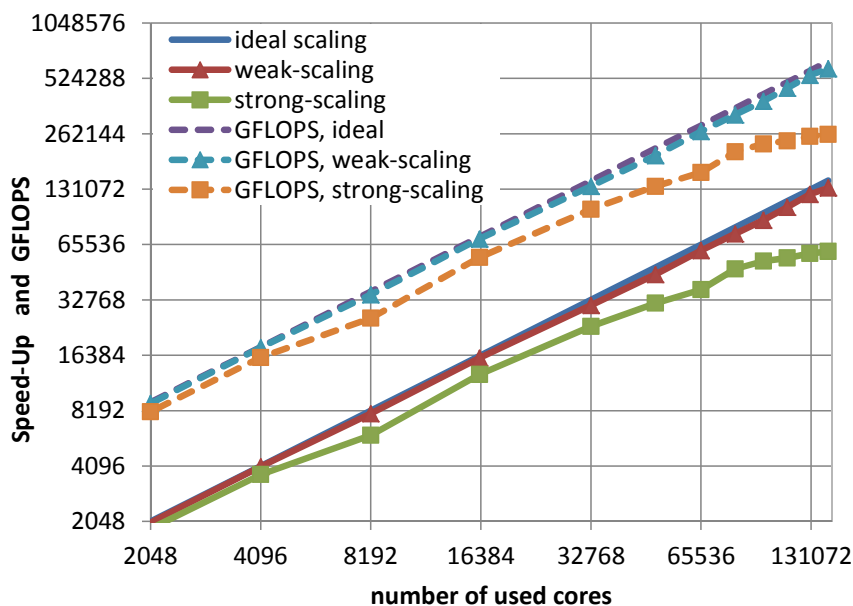


Figure 4.8: Weak and strong scaling for 2 048 to 146 016 cores on SuperMUC. An approximately ideal scaling was achieved in case of weak scaling, whereas a parallel efficiency of 42 % was reached in the strong scaling tests. The present diagram is cut off at 2 048 cores, where a parallel efficiency of 91.1 % in case of strong scaling (compared to 128 cores) and 98.6 % in case of weak scaling (compared to one core) was obtained.

per node was specified as 4.52×10^8 . Roughly 1 GB per node had to be reserved for the buffers, using one MPI rank per core. However, this slight overhead does not have a significant impact on the overall performance: On 146 016 cores of SuperMUC, a simulation of $N = 4.125 \times 10^{12}$ molecules was carried out with an execution time of roughly 40 seconds per MD integration time step. For this scenario, a speedup of 133 183 (compared to a single core) was achieved with an absolute performance of 591.2 TFLOPS. This corresponds to 9.4 % peak performance efficiency.

4.3 Molecular simulation of thermodynamic properties

With the advance of computing power, the scope of application scenarios for molecular simulation is widening, both in terms of complexity of a given simulation and in terms of high throughput.⁴ Nowadays, the predictive simulation of entire phase diagrams has become feasible. To rely on the simulation results, the methodology needs to be sound and the implementation must be thoroughly verified. The present section discusses the most recent release, i.e. version 2.0, of the *ms2* program (molecular simulation: second generation). Results from *ms2* have been verified, and the implementation was found to be robust and efficient.

⁴This section is based on Glass *et al.* [224] and Reiser *et al.* [225].

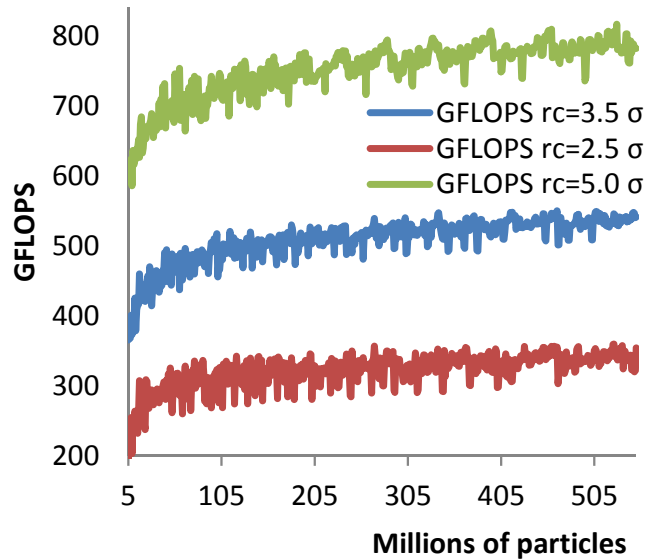


Figure 4.9: GFLOPS depending on the number of molecules and the cutoff for simulations with the present optimized version of *ls1 mardyn* on 128 cores of the SuperMUC supercomputer.

The *ms2* code is openly available⁵ for academic users. In version 2.0 of *ms2*, the MPI parallelization of the MD simulation is hybridized with OpenMP, leading to an excellent performance on multi-core processors. On this basis, a wide scope of thermodynamic bulk properties becomes accessible for homogeneous systems. The focus of *ms2* is on vapour-liquid equilibria by Grand Equilibrium simulation [8] as well as thermodynamic properties of homogeneous bulk fluids [10]. The considered molecular models are the same as for *ls1 mardyn*, i.e. rigid models with LJ sites, point multipoles, and point charges. In its present version, *ms2* features evaluating free energy derivatives in a systematic manner. This augments the range of sampled properties significantly, and it allows to straightforwardly develop competitive fundamental equations of state from a combination of experimental VLE data and molecular simulation results [226].

This approach is based on the fact that the fundamental equation of state contains the complete thermodynamic information about a system, which can be expressed in terms of various thermodynamic potentials [227], e.g. internal energy $E(N, V, S)$, enthalpy $H(N, p, S)$, Helmholtz free energy $\mathcal{A}(N, V, T)$, or Gibbs free energy $G(N, p, T)$. These representations are equivalent in the sense that any other thermodynamic property can be expressed using partial derivatives of the fundamental quantity. The form

$$\mathcal{A}\beta = \Phi(N, V, \beta), \quad (4.2)$$

known as the Massieu potential, is preferable for practical reasons, as outlined by Lustig [6, 228]. Therein, $\beta = 1/T$ is the inverse temperature. The statistical-mechanical formalism

⁵<http://www.ms-2.de/>

derived by Lustig [6, 228, 229] allows for the simultaneous sampling of multiple normalized derivatives of the Massieu potential

$$\Phi_{kl} = \beta^k \rho^l \frac{\partial^{k+l} \Phi}{\partial \beta^k \partial \rho^l} = \Phi_{kl}^{\text{id}} + \Phi_{kl}^{\text{res}}, \quad (4.3)$$

from a single simulation in the canonical ensemble, separating Φ_{kl} into an ideal part Φ_{kl}^{id} and a residual part Φ_{kl}^{res} . The computation of the residual part is the target of molecular simulation. In *ms2*, the derivatives Φ_{10}^{res} , Φ_{01}^{res} , Φ_{20}^{res} , Φ_{11}^{res} , Φ_{02}^{res} , Φ_{30}^{res} , Φ_{21}^{res} , and Φ_{12}^{res} are implemented for the canonical ensemble. The ideal part can be obtained by independent methods, e.g. from spectroscopic data or ab-initio calculations. However, it can be shown that for any Massieu potential derivative Φ_{kl} with $l > 0$, the ideal part is either zero or depends exclusively on the density, so that it is precisely known [228]. From five of these derivatives (i.e. Φ_{10} , Φ_{01} , Φ_{20} , Φ_{11} , and Φ_{02}), every measurable thermodynamic property can be expressed [226], with the exception of phase equilibria.

The calculation of the derivatives of to the order of $l \leq 2$ requires the explicit evaluation of $\partial E^{\text{pot}}/\partial V$ and $\partial^2 E^{\text{pot}}/\partial V^2$. For this purpose, the second-order virial, which is analogous to the virial but based on the second derivative $d^2 u_{ij}/dr_{ij}^2$ of the pair potential $u_{ij}(r_{ij})$, has to be determined [6, 228, 229]. For common molecular force fields of the LJ + point charge and multipole type supported by *ms2*, these derivatives can be computed straightforwardly. Thereby, in many cases, a long-range correction contribution needs to be considered, even though the simulated systems are homogeneous. The mathematical form of the LRC depends on the molecular interaction potential and the cutoff mode, i.e. based on the individual interaction sites or on the molecular centre of mass, cf. Section 1.4. In *ms2*, both the reaction-field method and Ewald summation are implemented, with the reaction field as default [10].

Transport properties are determined by equilibrium MD simulation, employing the Green-Kubo formalism [230]. This approach offers a direct relationship between transport coefficients and the time integral over the autocorrelation function of the corresponding fluxes. An extended time step is introduced to evaluate the fluxes, the autocorrelation functions, and their integrals. The extended time step is n_t times longer than the specified MD time step, where n_t is a user defined variable. The autocorrelation functions are then evaluated in one out of n_t MD integration time steps. As a consequence, the memory demand for the autocorrelation functions can be tuned, and the size of the restart files, which contain the current state of the autocorrelation functions and time integrals, can be limited. In particular, this approach is applied here to the electric conductivity of aqueous electrolyte solutions.

The evaluation of the electric conductivity κ is a measure for the mobility of ions in solution. The Green-Kubo formalism offers a direct relationship between κ and the time-autocorrelation

function of the electric current flux $\mathbf{J}^e(t)$ [231]

$$\kappa = \frac{1}{3VT} \int_0^\infty \langle \mathbf{J}^e(t) \mathbf{J}^e(0) \rangle dt. \quad (4.4)$$

Note that only the ions in the solution have to be considered here, not the electro-neutral molecules. In this way, the temperature dependence of the density and the electric conductivity of aqueous alkali halide salt solutions is investigated here for solutions containing all soluble combinations of alkali cations (Li^+ , Na^+ , K^+ , Rb^+ , and Cs^+) with halide anions (F^- , Cl^- , Br^- , and I^-) using the *ms2* program.

The force fields of the ions, which consist of one LJ site and a point charge, are taken from Reiser *et al.* [232]. They were adjusted to data of the density of the solutions, the self-diffusion coefficient of the ions in solution and the position of the first maximum of the radial distribution function of water around the ions [232, 233]. Water is modelled with the SPC/E force field [234], and the Lorentz-Berthelot combining rule is employed, cf. Eqs. (1.7) and (1.8). This choice is discussed in detail by Reiser *et al.* [232].

In a series of isothermal-isobaric MC simulations, the liquid density of aqueous alkali halide salt solutions was determined at $p = 1$ bar, for various temperatures and compositions. Depending on the composition, the simulation volume contained 10, 30, or 50 anions and cations, respectively. The total particle number $N = 1\,000$ was the same for all of these simulations. To compute the electric conductivities, additional canonical MD simulations were carried out with $N = 4\,500$ particles, using the density determined from the first series of simulations. The sampling length of the velocity and the electric current autocorrelation functions was set to 11 ps and the separation between the origins of two autocorrelation functions was 0.2 ps.

As Moucka *et al.* [235] observes, when the SPC/E water model is used, the force fields for the sodium cation and the chloride anion from Deublein *et al.* [233] as well as Smith and Dang [236] give the best results, among the available SPC/E compatible force fields, for the density of relatively dilute aqueous NaCl solutions at 293.15 K and 1 bar. For the Reiser *et al.* [232] potential parameters, which constitute a minor modification of those given by Deublein *et al.* [233], a good agreement with experimental data concerning the density can therefore be expected. The present simulation results confirm this expectation. Fig. 4.10 compares experimental and simulation data for the normalized density $\tilde{\rho} = \rho/\rho_p$ of aqueous alkali halide salt solutions, which is defined as the ratio of the density ρ of the electrolyte solution and the density ρ_p of the pure solvent, i.e. the density of real water (for experimental data) or the SPC/E model (for simulation results).

The temperature dependence of the electric conductivity κ of aqueous NaCl salt solutions was investigated for ion mole fractions up to 0.018 mol/mol in the temperature range from 293.15 to 333.15 K. This specific salt was chosen because experimental data are available over the entire investigated temperature range [237]. As shown in Fig. 4.11, the electric conductivity

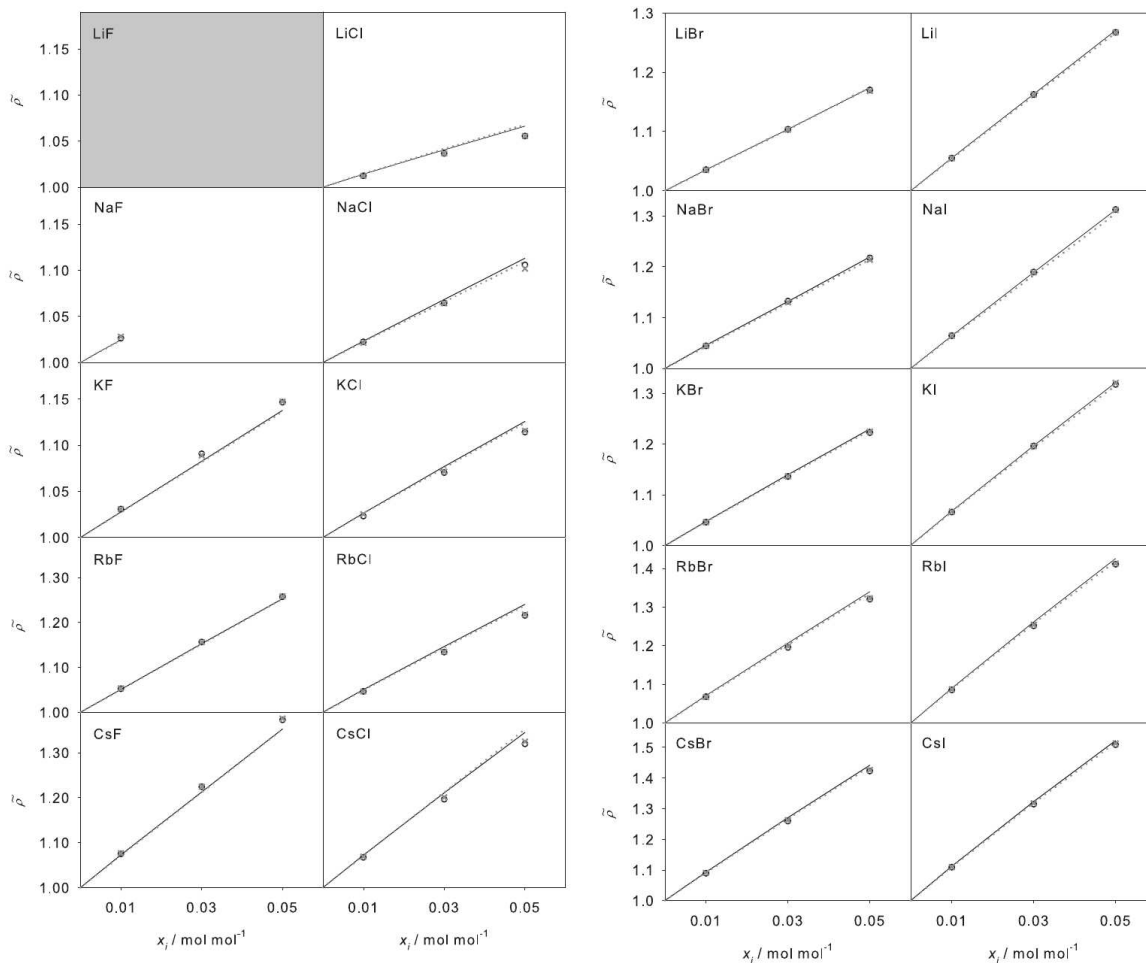


Figure 4.10: Normalized density of aqueous alkali halide salt solutions as a function of the ion mole fraction at 1 bar. Present simulation results (symbols), using the *ms2* program, are compared with correlations of experimental data (lines), cf. Reiser *et al.* [225], for $T = 293.15$ (\circ , —) and 333.15 K (\times , \cdots). In several cases, the respective values are so close to each other that they cannot be distinguished visually in the present representation. LiF is only soluble in trace amounts; hence, no data for LiF are shown here.

predicted at 293.15 K is in excellent agreement with the experimental data. The deviations are below 6 % over the entire concentration range; the dependence of κ on the salt concentration at constant temperature was discussed earlier by Reiser *et al.* [232]. The increase of the electric conductivity with increasing temperature is reproduced by the simulation qualitatively, but the quantitative deviation between experimental data and simulation results increases. The greatest deviation (reached at 333.15 K) is 17 %, for an ion mole fraction of 0.018 mol/mol. Over the entire investigated composition range, the electric conductivity of the NaCl solution is increasingly underestimated with increasing temperature. This deviation can be attributed to the underestimation of the self-diffusion coefficients of the ions by the present force field.

Furthermore, the computation of the thermal conductivity λ , implemented for pure fluids by Deublein *et al.* [10], was extended to mixtures for *ms2* version 2.0. The thermal conduc-

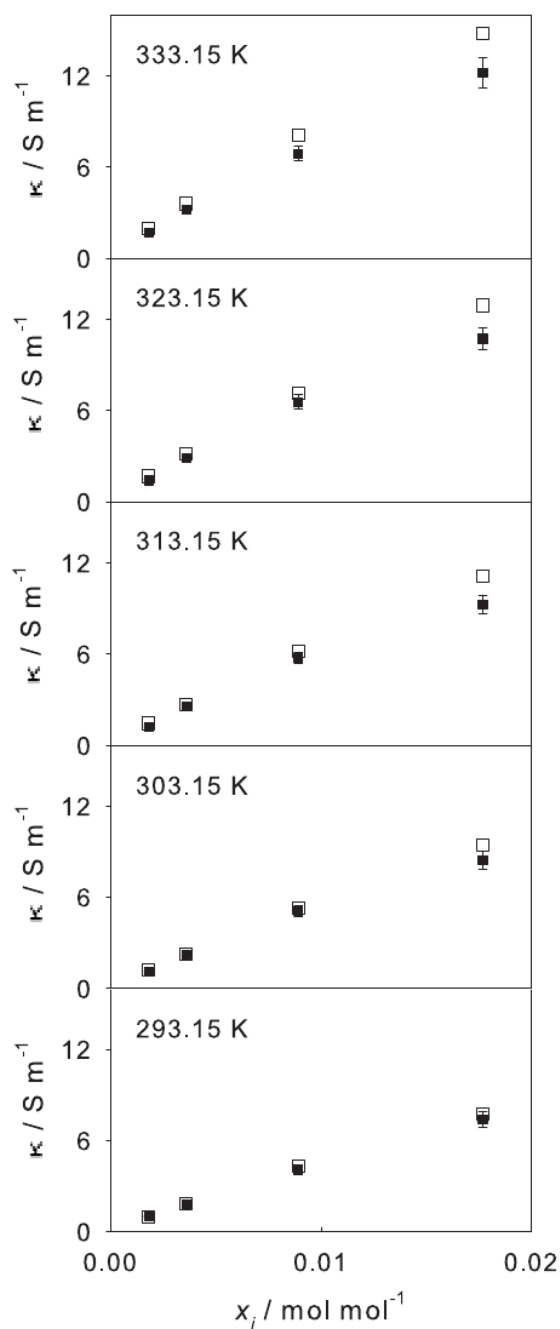


Figure 4.11: Electric conductivity of aqueous NaCl salt solutions as a function of the ion mole fraction at 1 bar. Simulation results (solid symbols) are compared to experimental data (empty symbols), cf. Lobo [237]. The statistical simulation uncertainties of the electric conductivities were found to be about $\pm 8\%$ for all investigated concentrations at all temperatures.

tivity is determined from the autocorrelation function of the microscopic heat flux \mathbf{J}^h . This relationship is given by

$$\lambda = \frac{1}{3VT^2} \int_0^\infty \langle \mathbf{J}^h(t) \mathbf{J}^h(0) \rangle dt. \quad (4.5)$$

In mixtures, energy transport and diffusion are coupled, and the heat flux for a mixture of n components is [238]

$$\begin{aligned} \mathbf{J}^h = & \frac{1}{2} \sum_{k=1}^n \sum_{i=1}^{N_k} \left[m_k v_i^2 + \underline{\omega}_i \mathbf{I}_k \underline{\omega}_i + \sum_{l=1}^n \sum_{j=1}^{N_l} u_{kl}(r_{ij}) \right] \mathbf{v}_i \\ & - \frac{1}{2} \sum_{1 \leq k, l \leq n} \sum_{i=1}^{N_k} \sum_{j=1}^{N_l} \mathbf{r}_{ij} \left(\mathbf{v}_i \frac{\partial u_{kl}(r_{ij})}{\partial r_{ij}} + \underline{\omega}_i \mathbf{M}_{ij} \right) - \sum_{k=1}^n h_k \sum_{i=1}^{N_k} \mathbf{v}_i, \end{aligned} \quad (4.6)$$

where h_k is the partial molar enthalpy of component k , $\underline{\omega}_i$ is the angular velocity vector of molecule i , \mathbf{I}_i is its inertial tensor, and \mathbf{M}_{ij} is the torque due to the interaction of the molecules i and j . The partial molar enthalpy is accessible with *ms2* by isothermal-isobaric simulations.



Figure 4.12: Speedup of hybrid MPI/OpenMP vs. pure MPI for *ms2* on the *hermit* supercomputer, using 2048 cores with a varying number of threads per MPI process, regarding systems containing 1024 (empty triangles), 2048 (solid triangles), 4096 (circles), and 8192 water molecules (bullets).

Systems investigated with *ms2* typically contain of the order of 1000 molecules. While for MC simulations, a perfect scaling behaviour up to large numbers of cores can be trivially achieved, MD domain decomposition – the de facto standard for highly scalable MD – is not feasible for such system sizes, because the cutoff radius is in the same range as half the edge length of the simulation volume. This excludes domain decomposition and limits the scalability of the MPI parallelization.

The present release of *ms2* features an OpenMP parallelization, which was hybridized with

MPI. At the point where MPI communication becomes a bottleneck, a single process still has enough load to distribute to multiple threads, improving the scalability. Three parts of *ms2* were parallelized with OpenMP: the interaction partner search, the energy computation and the force computation. All OpenMP-parallel regions rely on loop parallelism, as the computationally intensive parts of the algorithm all feature a loop over the molecules.

Table 4.2: Run-time performance results with *ms2* version 2.0 for MD simulations of pure water at $T = 298.15$ K and $\rho = 55.345$ mol/l. The number of time steps was 100 000 for every simulation, and the cutoff radius was identical for simulations with the same number of molecules. All simulations were performed in the same computing environment.

cores	threads	N	run time [s]
8	8 MPI	500	416
8	8 MPI	1 000	874
8	8 MPI	2 000	4 461
16	16 MPI	500	233
16	16 MPI	1 000	477
16	16 MPI	2 000	2 298
32	32 MPI	500	152
32	32 MPI	1 000	296
32	32 MPI	2 000	1 286
64	64 MPI	500	119
64	64 MPI	1 000	228
64	64 MPI	2 000	814
128	128 MPI	500	105
128	128 MPI	1 000	197
128	128 MPI	2 000	557
8	1 MPI · 8 OMP/MPI	500	483
8	1 MPI · 8 OMP/MPI	1 000	975
8	1 MPI · 8 OMP/MPI	2 000	4 831
16	2 MPI · 8 OMP/MPI	500	253
16	2 MPI · 8 OMP/MPI	1 000	517
16	2 MPI · 8 OMP/MPI	2 000	2 514
32	4 MPI · 8 OMP/MPI	500	167
32	4 MPI · 8 OMP/MPI	1 000	316
32	4 MPI · 8 OMP/MPI	2 000	1 362
64	8 MPI · 8 OMP/MPI	500	119
64	8 MPI · 8 OMP/MPI	1 000	217
64	8 MPI · 8 OMP/MPI	2 000	785
128	16 MPI · 8 OMP/MPI	500	101
128	16 MPI · 8 OMP/MPI	1 000	172
128	16 MPI · 8 OMP/MPI	2 000	496

In the force calculation, race conditions need to be considered, because every calculated force is written to both interacting molecules. Introducing atomic updates or critical sections leads to massive overheads. Instead, it is more efficient to assign forces from individual interactions

to the elements of a list (or an array) which is subsequently summed up. The same approach is followed for computing the rotational torques.

In Fig. 4.12, the speedup of *ms2* with hybrid MPI/OpenMP parallelization (compared to pure MPI) is shown for 2 048 cores on the *hermit* supercomputer, varying the number of OpenMP threads per MPI process as well as the number of molecules in the simulation volume. It can be seen that using two to four threads per MPI process delivers a speedup of around 20 % for 2 048 cores. Additional run-time performance comparisons are given in Tab. 4.2.

5 Conclusion

Molecular modelling is a reliable method for describing and predicting thermodynamic properties.¹ Moreover, massively-parallel MD simulation of large heterogeneous systems can contribute to elucidating the molecular effects that underlie transport processes at interfaces. Reaching quantitative agreement with real fluid properties, this constitutes a promising approach for optimizing engineering processes, in particular, if solid surfaces and their contact with the fluid are represented realistically.

In nanosystems, many relationships known from macroscopic systems break down due to the predominance of surface over bulk effects as well as the interference between continuous variations of thermodynamic properties and the discrete structure of matter at the molecular level. In Section 1.3, it was shown that for systems on an extremely small scale, the Gibbs adsorption equation does not hold strictly. For systems interacting by Lennard-Jones (and LJTS) potentials, finite-size effects on the vapour-liquid surface tension were investigated systematically in Chapter 2. In particular, it was addressed that without knowing γ precisely, e.g. because it is a quantity that is not given in advance but needs to be determined, the Laplace radius $R_L = 2\gamma/\Delta p$ is not accessible directly. Instead, in Section 2.1, Tolman's theory of spherical interfaces was reformulated in terms of the capillarity radius $R_\kappa = 2\gamma_0/\Delta p$, on the basis of the known surface tension of a macroscopic planar vapour-liquid interface.

Thereby, it was shown that the curvature dependence (to first order in $1/R$) of the surface tension of nanodroplets is relatively weak, corresponding to a small Tolman length δ . On the other hand, the presence of a curvature-independent size effect was proven for the surface tension of thin liquid films in Section 2.2, an effect which is expected to be at least similarly strong for spherical interfaces as the first-order curvature effect from Tolman's law. In this light, Tolman's law cannot be upheld any longer. In Section 2.3, it was shown for nanobubbles how curvature-dependent and curvature-independent size effects interfere. For bubbles with an intermediate size, the vapour density at the centre of a bubble in equilibrium, e.g., is much smaller than the dew density corresponding to a macroscopic saturated vapour over a planar vapour-liquid phase boundary at the same temperature. Extremely small bubbles, however, exhibit an increased density which cannot be ascribed to the influence of curvature and the increased pressure, following the Laplace equation, but only to the small volume available

¹This chapter is partly based on Horsch and Hasse [239].

to the dispersed phase. The crossover between both regimes was found to occur at a bubble radius of 9σ , i.e. about 3 nm.

A particular challenge for molecular methods consists in reaching quantitative reliability for modelling adsorption, cf. Chapter 3. Beside the force field for the fluid, this also requires a representation of the solid phase and the interaction between fluid molecules and the adsorber surface. Moreover, the substrate can possess regular and irregular structures that combine to form a complex morphology [240]. Developments in this direction are promising, and they profit from various advantages of molecular simulation over purely empirical methods. On the basis of validated molecular models, multiple adsorbed layers can be predicted without resorting to overly simplified approximations from phenomenological thermodynamics [240, 241].

Wetting of a solid by a fluid can be considered by simulating the three-phase contact between a vapour-liquid interface and the surface of a solid substrate, cf. Section 3.1. In such simulations, multiple ordered adsorbed layers from the liquid phase and a single adsorbed layer from the gas phase can be discerned, cf. Fig. 3.2. This linear order interferes in a non-trivial way with the approximately spherical shape of the droplet and yields a molecular structure that cannot be uncovered experimentally and can hence only be revealed by molecular simulation. Contact angles from the simulation can be compared to experimental data to parameterize the fluid-wall interaction [240], assuming that the structure of the experimentally considered system is realistically modelled, accounting for surface roughness, irregularities, and other imperfections of the surface, such as residual adsorbed matter.

Furthermore, transport properties such as thermal conductivities, viscosities, and diffusion coefficients are experimentally accessible and highly relevant for numerous applications in process engineering. As commented in Section 1.1, *processes at interfaces* are a particularly promising application of molecular methods, where Computational Molecular Engineering is close to achieving significant breakthroughs. In heterogeneous systems, e.g. at a wall or close to a phase boundary, the dissipation occurring by heat, momentum, and mass transfer is often non-linear or characterized by complex boundary conditions [242], which have to be understood to accurately describe mass transfer through nanoporous materials [243–245]. Molecular simulation can help to understand these boundary conditions and non-linear phenomena [246–248].

There are numerous applications in micro- and nanofluidics simulation [243], e.g. concerning flow through nanoporous membranes [244, 245]. Collective diffusion coefficients of fluids in contact with a nanostructured solid substrate can be computed by NEMD with Ható's daemon [249] or Avendaño's daemon [244], which acts on a part of simulation volume to accelerate differently labelled, but otherwise identical molecules in opposite directions. Analogous simulation methods can capture the local shear viscosity of the fluid and the pressure drop in a nanofluidics scenario. Thereby, molecular simulation can reproduce entrance and exit

effects, cf. Fig. 5.1, which can be particularly relevant for filtration. The main advantage of non-equilibrium over equilibrium MD simulation is that it also applies to transport processes in the non-linear regime, e.g. for non-Newtonian fluids or extreme driving forces.

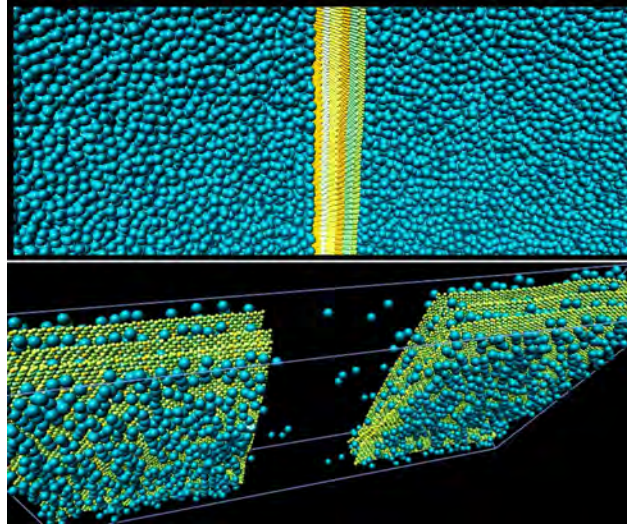


Figure 5.1: Visualization of configurations from NEMD simulations of pressure-gradient driven Poiseuille flow of water through nanoporous carbon, represented here by a planar slit pore.

Due to its molecular resolution, MD simulation is particularly suitable for investigating coupled heat and mass transfer during a phase transition such as vaporization by pool boiling or condensation in a supersaturated vapour. These processes are activated, starting from a metastable state, and are initialized by the formation of dispersed nanoscopic nuclei of the phase that is thermodynamically stable under the respective conditions. The first step of the process is nucleation, by which supercritical nuclei emerge after a free energy barrier has been overcome. Even though nucleation, as an activated process, is more complex than spontaneous relaxation processes, it can also be simulated directly. In this case, a single MD simulation can reproduce the whole phase transition. A related NEMD approach consists in simulating the pseudo-grand canonical ensemble with McDonald's daemon: This Maxwellian daemon removes large nuclei of the emerging dispersed phase, and the nucleation rate can be determined from the frequency of these interventions [246].

By massively-parallel high performance computing, e.g. using the *ls1 mardyn* program,² molecular simulation becomes an experiment *in silico*. Due to their heterogeneous structure, systems with a phase boundary have stronger long-range interactions which also need to be taken into account, cf. Section 1.4. As shown in Sections 4.1 and 4.2, load balancing by recursive bisection of the simulation volume, using an adaptive linked-cell data structure, significantly improves the scalability of the code. In this way, supercomputers with a large number of cores can be used efficiently both for homogeneous and heterogeneous systems.

²<http://www.ls1-mardyn.de/>

In Section 4.3, the *ms2* program³ for molecular simulations of homogeneous fluid systems was presented, which is presently available in its second release. By building a consistent tool kit for molecular modelling and simulation on the basis of these two highly performant engines, computational molecular engineering and its applications in the chemical industry will be further advanced in the coming years.

³<http://www.ms-2.de/>

Bibliography

- [1] M. P. Allen, D. J. Tildesley: *Computer Simulation of Liquids*, Oxford University Press, 1989.
- [2] M. Horsch, C. Niethammer, J. Vrabec, H. Hasse: Computational molecular engineering as an emerging technology in process engineering, *Information Technology* 55 (2013) 97–101.
- [3] J. E. Stone, D. J. Hardyn, I. S. Ufimtsev, K. Schulten: GPU-accelerated molecular modeling coming of age, *Journal of Molecular Graphics and Modelling* 29 (2010) 116–125.
- [4] G. Guevara Carrión, H. Hasse, J. Vrabec: Thermodynamic properties for applications in chemical industry via classical force fields, in: *Multiscale Molecular Methods in Applied Chemistry*, number 307 in *Topics in Current Chemistry*, Springer, Heidelberg, 2012, pp. 201–249.
- [5] P. Ungerer, C. Nieto Draghi, B. Rousseau, G. Ahunbay, V. Lachet: Molecular simulation of the thermophysical properties of fluids: From understanding toward quantitative predictions, *Journal of Molecular Liquids* 134 (2007) 71–89.
- [6] R. Lustig: Direct molecular NVT simulation of the isobaric heat capacity, speed of sound, and Joule-Thomson coefficient, *Molecular Simulation* 37 (2011) 457–465.
- [7] F. Rösch, H.-R. Trebin: Crack front propagation by kink formation, *Europhysics Letters* 87 (2009) 66004.
- [8] J. Vrabec, H. Hasse: Grand Equilibrium: Vapour-liquid equilibria by a new molecular simulation method, *Molecular Physics* 100 (2002) 3375–3383.
- [9] A. Z. Panagiotopoulos: Direct determination of phase coexistence properties of fluids by Monte Carlo simulation in a new ensemble, *Molecular Physics* 61 (1987) 813–826.
- [10] S. Deublein, B. Eckl, J. Stoll, S. V. Lishchuk, G. Guevara Carrión, C. W. Glass, T. Merker, M. F. Bernreuther, H. Hasse, J. Vrabec: ms2: A molecular simulation tool for thermodynamic properties, *Computer Physics Communications* 182 (2011) 2350–2367.

- [11] K. Binder: Applications of Monte Carlo methods to statistical physics, *Reports on Progress in Physics* 60 (1997) 487–559.
- [12] C. Holm, W. Janke: Finite-size scaling study of the three-dimensional classical Heisenberg model, *Physica A* 173 (1993) 8–12.
- [13] B. Eckl, J. Vrabec, H. Hasse: Set of molecular models based on quantum mechanical ab initio calculations and thermodynamic data, *Journal of Physical Chemistry B* 112 (2008) 12710–12721.
- [14] B. Eckl, J. Vrabec, H. Hasse: On the application of force fields for predicting a wide variety of properties: Ethylene oxide as an example, *Fluid Phase Equilibria* 274 (2008) 16–26.
- [15] S. Toxvaerd: Molecular dynamics calculation of the equation of state of alkanes, *Journal of Chemical Physics* 93 (1990) 4290–4295.
- [16] M. G. Martin, J. I. Siepmann: Novel configurational-bias Monte Carlo method for branched molecules. Transferable potentials for phase equilibria. 2. United-atom description of branched alkanes, *Journal of Physical Chemistry B* 103 (1999) 4508–4517.
- [17] P. Ungerer, C. Beauvais, J. Delhommelle, A. Boutin, B. Rousseau, A. H. Fuchs: Optimization of the anisotropic united atoms intermolecular potential for n-alkanes, *Journal of Chemical Physics* 112 (2000) 5499–5510.
- [18] E. Forte, A. J. Haslam, G. Jackson, E. A. Müller: Effective coarse-grained solid-fluid potentials and their application to model adsorption of fluids on heterogeneous surfaces, *Physical Chemistry Chemical Physics* 16 (2014) 19165–19180.
- [19] M. Horsch, J. Vrabec, M. Bernreuther, H. Hasse: Poiseuille flow of liquid methane in nanoscopic graphite channels by molecular dynamics simulation, in: K. Hanjalić, Y. Nagano, S. Jakirlić (Eds.), *Proceedings of the 6th International Symposium on Turbulence, Heat and Mass Transfer*, Begell House, New York, 2009, pp. 89–92.
- [20] T. Schnabel, J. Vrabec, H. Hasse: Unlike Lennard-Jones parameters for vapor-liquid equilibria, *Journal of Molecular Liquids* 135 (2007) 170–178.
- [21] J. Vrabec, Y.-L. Huang, H. Hasse: Molecular models for 267 binary mixtures validated by vapor-liquid equilibria: A systematic approach, *Fluid Phase Equilibria* 279 (2009) 120–135.
- [22] Y.-L. Huang, T. Merker, M. Heilig, H. Hasse, J. Vrabec: Molecular modeling and simulation of vapor-liquid equilibria of ethylene oxide, ethylene glycol, and water as well as their binary mixtures, *Industrial & Engineering Chemistry Research* 51 (2012) 7428–7440.

- [23] I. T. Todorov, W. Smith, K. Trachenko, M. T. Dove: DL_POLY_3: New dimensions in molecular dynamics simulations via massive parallelism, *Journal of Materials Chemistry* 16 (2006) 1911–1918.
- [24] M. J. Chorley, D. W. Walker: Performance analysis of a hybrid MPI/OpenMP application on multi-core clusters, *Journal of Computational Science* 1 (2010) 168–174.
- [25] J. A. Purton, J. C. Crabtree, S. C. Parker: DL_MONTE: A general purpose program for parallel Monte Carlo simulation, *Molecular Simulation* 39 (2013) 1240–1252.
- [26] J. C. Phillips, R. Braun, W. Wang, J. Gumbart, E. Tajkhorshid, E. Villa, C. Chipot, R. D. Skeel, L. Kale, K. Schulten: Scalable molecular dynamics with NAMD, *Journal of Computational Chemistry* 26 (2005) 1781–1802.
- [27] S. Plimpton: Fast parallel algorithms for short-range molecular dynamics, *Journal of Computational Physics* 117 (1995) 1–19.
- [28] J. Roth, F. Gähler, H.-R. Trebin: A molecular dynamics run with 5 180 116 000 particles, *International Journal of Modern Physics C* 11 (2000) 317–322.
- [29] S. Sonntag, C. Triched Paredes, J. Roth, H.-R. Trebin: Molecular dynamics simulations of cluster distribution from femtosecond laser ablation in aluminum, *Applied Physics A* 104 (2011) 559–565.
- [30] H.-J. Limbach, A. Arnold, B. A. Mann, C. Holm: ESPResSo - An extensible simulation package for research on soft matter systems, *Computer Physics Communications* 174 (2006) 704–727.
- [31] J. D. Halverson, T. Brandes, O. Lenz, A. Arnold, S. Bevc, V. Starchenko, K. Kremer, T. Stuehn, D. Reith: ESPResSo++: A modern multiscale simulation package for soft matter systems, *Computer Physics Communications* 184 (2013) 1129–1149.
- [32] W. G. Chapman, K. E. Gubbins, G. Jackson, M. Radosz: New reference equation of state for associating liquids, *Industrial & Engineering Chemistry Research* 29 (1990) 1709–1721.
- [33] J. Gross, G. Sadowski: Perturbed-Chain SAFT: An equation of state based on a perturbation theory for chain molecules, *Industrial & Engineering Chemistry Research* 40 (2001) 1244–1260.
- [34] A. Lymeriadis, C. S. Adjiman, A. Galindo, G. Jackson: A group contribution method for associating chain molecules based on the statistical associating fluid theory (SAFT- γ), *Journal of Chemical Physics* 127 (2007) 234903.

- [35] T. Lafitte, A. Apostolakou, C. Avendaño, A. Galindo, C. S. Adjiman, E. A. Müller, G. Jackson: Accurate statistical associating fluid theory for chain molecules formed from Mie segments, *Journal of Chemical Physics* 139 (2013) 154504.
- [36] H. Kahl, S. Enders: Interfacial properties of binary mixtures, *Physical Chemistry Chemical Physics* 4 (2002) 931–936.
- [37] G. J. Gloor, G. Jackson, F. J. Blas, E. Martín del Río, E. de Miguel: An accurate density functional theory for the vapor-liquid interface of associating chain molecules based on the statistical associating fluid theory for potentials of variable range, *Journal of Chemical Physics* 121 (2004) 12740–12759.
- [38] J. Gross: A density functional theory for vapor-liquid interfaces using the PCP-SAFT equation of state, *Journal of Chemical Physics* 131 (2009) 204705.
- [39] E. A. Müller, A. Mejía: Interfacial properties of selected binary mixtures containing *n*-alkanes, *Fluid Phase Equilibria* 282 (2009) 68–81.
- [40] L. D. Landau, E. M. Lifshitz: *Статистическая физика*, ГИИТЛ, 1951. Курс теоретической физики, том V, часть 1.
- [41] C. A. de Coulomb: Premier mémoire sur l'électricité et le magnétisme: Construction et usage d'une balance électrique, fondée sur la propriété qu'ont les fils de métal, d'avoir une force de réaction de torsion proportionnelle à l'angle de torsion, *Mémoires de l'Académie Royale des Sciences* 88 (1785) 569–577.
- [42] C. A. de Coulomb: Second mémoire sur l'électricité et le magnétisme, où l'on détermine, suivant quelles lois le fluide magnétique, ainsi que le fluide électrique, agissent, soit par répulsion, soit par attraction, avec 1 planche, *Mémoires de l'Académie Royale des Sciences* 88 (1785) 578–611.
- [43] F. London: Über einige Eigenschaften und Anwendungen der Molekularkräfte, *Zeitschrift für physikalische Chemie* 11 (1930) 222–251.
- [44] J. E. Jones: On the determination of molecular fields, *Proceedings of the Royal Society A* 106 (1924) 441–477.
- [45] Y.-L. Huang, J. Vrabec, H. Hasse: Prediction of ternary vapor-liquid equilibria for 33 systems by molecular simulation, *Fluid Phase Equilibria* 287 (2009) 62–69.
- [46] L. Onsager: Electric moments of molecules in liquids, *Journal of the American Chemical Society* 58 (1936) 1486–1493.
- [47] B. Saager, J. Fischer, M. Neumann: Reaction field simulations of monatomic and diatomic dipolar fluids, *Molecular Simulation* 6 (1991) 27–49.

- [48] A. Arnold, C. Holm: Efficient methods to compute long-range interactions for soft matter systems, *Advances in Polymer Science* 185 (2005) 59–109.
- [49] A. Arnold, F. Fahrenberger, C. Holm, O. Lenz, M. Bolten, H. Dachsel, R. Halver, I. Kabadshow, F. Gähler, F. Heber, J. Iseringhausen, M. Hofmann, M. Pippig, D. Potts, G. Sutmann: Comparison of scalable fast methods for long-range interactions, *Physical Review E* 88 (2013) 063308.
- [50] M. Deserno, C. Holm: How to mesh up Ewald sums. I. A theoretical and numerical comparison of various particle mesh routines, *Journal of Chemical Physics* 109 (1998) 7678–7693.
- [51] R. Salomon Ferrer, A. W. Götz, D. Poole, S. Le Grand, R. C. Walker: Routine microsecond molecular dynamics simulations with AMBER on GPUs. 2. Explicit solvent particle mesh Ewald, *Journal of Chemical Theory and Computation* 9 (2013) 3878–3888.
- [52] S. Samin, Y. Tsori, C. Holm: Vapor-liquid coexistence of the Stockmayer fluid in nonuniform external fields, *Physical Review E* 87 (2013) 052128.
- [53] K. N. Kudin, G. E. Scuseria: Analytic stress tensor with the periodic fast multipole method, *Physical Review B* 61 (2000) 5141–5146.
- [54] L. Verlet: Computer «experiments» on classical fluids. I. Thermodynamical properties of Lennard-Jones molecules, *Physical Review* 159 (1967) 98–103.
- [55] M. Horsch, H. Hasse: Molecular simulation of nano-dispersed fluid phases, *Chemical Engineering Science* 107 (2014) 235–244.
- [56] M. Horsch, H. Hasse, A. K. Shchekin, A. Agarwal, S. Eckelsbach, J. Vrabec, E. A. Müller, G. Jackson: Excess equimolar radius of liquid drops, *Physical Review E* 85 (2012) 031605.
- [57] E. de Miguel: Computation of surface tensions using expanded ensemble simulations, *Journal of Physical Chemistry B* 112 (2008) 4674–4679.
- [58] K. Binder: Monte Carlo calculation of the surface tension for two- and three-dimensional lattice-gas models, *Physical Review A* 25 (1982) 1699–1709.
- [59] M. Schrader, P. Virnau, D. Winter, T. Zykova-Timan, K. Binder: Methods to extract interfacial free energies of flat and curved interfaces from computer simulations, *European Physical Journal Special Topics* 177 (2009) 103–127.
- [60] G. Bakker: Kapillarität und Oberflächenspannung, number 6 in *Handbuch der Experimentalphysik*, Akademische Verlagsgesellschaft, Leipzig, 1928.

- [61] E. Salomons, M. Mareschal: Surface tension, adsorption and surface entropy of liquid-vapour systems by atomistic simulation, *Journal of Physics: Condensed Matter* 3 (1991) 3645–3661.
- [62] J. P. R. B. Walton, D. J. Tildesley, J. S. Rowlinson, J. R. Henderson: The pressure tensor at the planar surface of a liquid, *Molecular Physics* 48 (1983) 1357–1368.
- [63] J. Vrabec, G. K. Kedia, G. Fuchs, H. Hasse: Comprehensive study on vapour-liquid co-existence of the truncated and shifted Lennard-Jones fluid including planar and spherical interface properties, *Molecular Physics* 104 (2006) 1509–1527.
- [64] G. V. Lau, I. J. Ford, P. A. Hunt, E. A. Müller, G. Jackson: Surface thermodynamics of planar, cylindrical and spherical vapour-liquid interfaces, *Journal of Chemical Physics* 142 (2015) 114701.
- [65] P.-S. de Laplace: *Traité de Mécanique Céleste*, volume 3, Bachelier, Paris, 1806.
- [66] F. P. Buff: Spherical interface. I. Thermodynamics, *Journal of Chemical Physics* 19 (1951) 1591–1594.
- [67] F. P. Buff: Spherical interface. II. Molecular theory, *Journal of Chemical Physics* 23 (1955) 419–427.
- [68] S. Kondo: Thermodynamical fundamental equation for spherical interface, *Journal of Chemical Physics* 25 (1956) 662–669.
- [69] A. Harasima: Statistical mechanics of surface tension, *Journal of the Physical Society of Japan* 8 (1953) 343–347.
- [70] S. M. Thompson, K. E. Gubbins, J. P. R. B. Walton, R. A. R. Chantry, J. S. Rowlinson: A molecular dynamics study of liquid drops, *Journal of Chemical Physics* 81 (1984) 530–542.
- [71] V. G. Baidakov, G. S. Boltachev: Curvature dependence of the surface tension of liquid and vapor nuclei, *Physical Review E* 59 (1999) 469–475.
- [72] J. H. Irving, J. G. Kirkwood: The statistical mechanical theory of transport processes. IV. The equations of hydrodynamics, *Journal of Chemical Physics* 18 (1950) 817–829.
- [73] A. E. van Giessen, E. M. Blokhuis: Direct determination of the Tolman length from the bulk pressures of liquid drops via molecular dynamics simulations, *Journal of Chemical Physics* 131 (2009) 164705.
- [74] E. M. Blokhuis, D. Bedeaux: Pressure tensor of a spherical interface, *Journal of Chemical Physics* 97 (1992) 3576–3586.

- [75] J. R. Henderson, J. Lekner: Surface oscillations and the surface thickness of classical and quantum droplets, *Molecular Physics* 36 (1978) 781–789.
- [76] P. Schofield, J. R. Henderson: Statistical mechanics of inhomogeneous fluids, *Proceedings of the Royal Society A* 379 (1982) 231–246.
- [77] J. R. Henderson: *Statistical mechanics of spherical surfaces*, Wiley, New York, 1986, pp. 555–605.
- [78] A. Ghoufi, P. Malfreyt: Local pressure components and surface tension of spherical interfaces. Thermodynamic versus mechanical definitions. I – A mesoscale modeling of droplets, *Journal of Chemical Physics* 135 (2011) 104105.
- [79] A. Ghoufi, F. Goujon, V. Lachet, P. Malfreyt: Expressions for local contributions to the surface tension from the virial route, *Physical Review E* 77 (2008) 031601.
- [80] C. H. Bennett: Efficient estimation of free-energy differences from Monte-Carlo data, *Journal of Computational Physics* 22 (1976) 245–268.
- [81] G. J. Gloor, G. Jackson, F. J. Blas, E. de Miguel: Test-area simulation method for the direct determination of the interfacial tension of systems with continuous or discontinuous potentials, *Journal of Chemical Physics* 123 (2005) 134703.
- [82] R. W. Zwanzig: High-temperature equation of state by a perturbation method. I. Non-polar gases, *Journal of Chemical Physics* 22 (1954) 1420–1426.
- [83] J. G. Sampayo, A. Malijeviský, E. A. Müller, E. de Miguel, G. Jackson: Evidence for the role of fluctuations in the thermodynamics of nanoscale drops and the implications in computations of the surface tension, *Journal of Chemical Physics* 132 (2010) 141101.
- [84] R. C. Tolman: Consideration of the Gibbs theory of surface tension, *Journal of Chemical Physics* 16 (1948) 758–774.
- [85] J. G. Sampayo Hernández: Determination of interfacial properties for planar and spherical surfaces of pure fluids by molecular simulation, Ph.D. thesis, 2010.
- [86] J. G. Kirkwood, F. P. Buff: The statistical mechanical theory of surface tension, *Journal of Chemical Physics* 17 (1949) 338–343.
- [87] J. Lekner, J. R. Henderson: Surface tension and energy of a classical liquid-vapour interface, *Molecular Physics* 34 (1977) 333–359.
- [88] J. K. Percus, L. A. Pozhar, K. E. Gubbins: Local thermodynamics of inhomogeneous fluids at equilibrium, *Physical Review E* 51 (1995) 261–265.

- [89] J. W. Gibbs: On the equilibrium of heterogeneous substances, *Transactions of the Connecticut Academy of Arts and Sciences* 3 (1878) 343–524.
- [90] T. L. Hill: *Thermodynamics of Small Systems*, W. A. Benjamin, New York, 1964.
- [91] M. P. Gelfand, M. E. Fisher: Finite-size effects in fluid interfaces, *Physica A* 166 (1990) 1–74.
- [92] R. A. Alberty: On the derivation of the Gibbs adsorption equation, *Langmuir* 11 (1995) 3598–3600.
- [93] S. Werth, G. Rutkai, J. Vrabec, M. Horsch, H. Hasse: Long-range correction for multi-site Lennard-Jones models and planar interfaces, *Molecular Physics* 112 (2014) 2227–2234.
- [94] M. Neumann: The dielectric constant of water. Computer simulations with the MCY potential, *Journal of Chemical Physics* 82 (1985) 5663–5672.
- [95] J. Janeček: Long range corrections in inhomogeneous simulations, *Journal of Physical Chemistry B* 110 (2006) 6264–6269.
- [96] V. K. Shen, R. D. Mountain, J. R. Errington: Comparative study on the effect of tail corrections on surface tension determined by molecular simulation, *Journal of Physical Chemistry B* 111 (2007) 6198–6207.
- [97] A. Trokhymchuk, J. Alejandre: Computer simulations of liquid/vapor interface in Lennard-Jones fluids: Some questions and answers, *Journal of Chemical Physics* 111 (1999) 8510–8523.
- [98] R. Lustig: Angle-average for the powers of the distance between two separated vectors, *Molecular Physics* 65 (1988) 175–179.
- [99] J. A. Barker, R. O. Watts: Monte Carlo studies of the dielectric properties of water-like models, *Molecular Physics* 26 (1973) 789–792.
- [100] R. Yokota, J. P. Bardhan, M. G. Knepley, L. A. Barba, T. Hamada: Biomolecular electrostatics using a fast multipole BEM on up to 512 GPUs and a billion unknowns, *Computer Physics Communications* 182 (2011) 1272–1283.
- [101] A. Lotfi, J. Vrabec, J. Fischer: Orthobaric densities from simulations of the liquid vapour interface, *Molecular Simulation* 5 (1990) 233–243.
- [102] M. Guo, B. C.-Y. Lu: Long range corrections to thermodynamic properties of inhomogeneous systems with planar interfaces, *Journal of Chemical Physics* 106 (1997) 3688–3695.

- [103] M. Mecke, J. Winkelmann, J. Fischer: Molecular dynamics simulation of the liquid–vapor interface: The Lennard-Jones fluid, *Journal of Chemical Physics* 107 (1997) 9264–9270.
- [104] R. Sperb: An alternative to Ewald sums. Part I: Identities for sums, *Molecular Simulation* 20 (1998) 179–200.
- [105] A. Arnold, C. Holm: MMM2D: A fast and accurate summation method for electrostatic interactions in 2D slab geometries, *Computer Physics Communications* 148 (2002) 327–348.
- [106] A. Arnold, J. de Joannis, C. Holm: Electrostatics in periodic slab geometries. I., *Journal of Chemical Physics* 117 (2002) 2496–2502.
- [107] P. J. in 't Veld, A. E. Ismail, G. S. Grest: Application of Ewald summations to long-range dispersion forces, *Journal of Chemical Physics* 127 (2007) 144711.
- [108] R. Isele-Holder, W. Mitchell, J. R. Hammond, A. Kohlmeyer, A. E. Ismail: Reconsidering dispersion potentials: Reduced cutoffs in mesh-based Ewald solvers can be faster than truncation, *Journal of Chemical Theory and Computation* 9 (2013) 5412–5420.
- [109] R. E. Isele-Holder, W. Mitchell, A. E. Ismail: Development and application of a particle-particle particle-mesh Ewald method for dispersion interactions, *Journal of Chemical Physics* 137 (2012) 174107.
- [110] J. Janeček, H. Krienke, G. Schmeer: Interfacial properties of cyclic hydrocarbons: A Monte Carlo study, *Journal of Physical Chemistry B* 110 (2006) 6916–6923.
- [111] F. Siperstein, A. L. Myers, O. Talu: Long range corrections for computer simulations of adsorption, *Molecular Physics* 100 (2002) 2025–2030.
- [112] J. Stoll, J. Vrabec, H. Hasse: Comprehensive study of the vapour-liquid equilibria of the two-centre Lennard-Jones plus pointdipole fluid, *Fluid Phase Equilibria* 209 (2003) 29–53.
- [113] T. Merker, C. Engin, J. Vrabec, H. Hasse: Molecular model for carbon dioxide optimized to vapor-liquid equilibria, *Journal of Chemical Physics* 132 (2010) 234512.
- [114] T. Merker, J. Vrabec, H. Hasse: Molecular simulation study on the solubility of carbon dioxide in mixtures of cyclohexane + cyclohexanone, *Fluid Phase Equilibria* 315 (2012) 77–83.
- [115] P. Orea, J. López Lemus, J. Alexandre: Oscillatory surface tension due to finite-size effects, *Journal of Chemical Physics* 123 (2005) 114702.

- [116] A. Werner, F. Schmid, M. Müller, K. Binder: Anomalous size-dependence of interfacial profiles between coexisting phases of polymer mixtures in thin-film geometry: A Monte Carlo simulation, *Journal of Chemical Physics* 107 (1997) 8175–8188.
- [117] B. Quentrec, C. Brot: New method for searching for neighbors in molecular dynamics computations, *Journal of Computational Physics* 13 (1973) 430–432.
- [118] T. Young: An essay on the cohesion of fluids, *Philosophical Transactions of the Royal Society of London* 95 (1805) 65–87.
- [119] R. C. Tolman: The superficial density of matter at a liquid-vapor boundary, *Journal of Chemical Physics* 17 (1949) 118–127.
- [120] R. C. Tolman: The effect of droplet size on surface tension, *Journal of Chemical Physics* 17 (1949) 333–337.
- [121] B. J. Block, S. K. Das, M. Oettel, P. Virnau, K. Binder: Curvature dependence of surface free energy of liquid drops and bubbles: A simulation study, *Journal of Chemical Physics* 133 (2010) 154702.
- [122] Ø. Wilhelmsen, D. Bedeaux, D. Reguera: Tolman length and rigidity constants of the Lennard-Jones fluid, *Journal of Chemical Physics* 142 (2015) 064706.
- [123] M. J. P. Nijmeijer, C. Bruin, A. B. van Woerkom, A. F. Bakker, J. M. J. van Leeuwen: Molecular dynamics of the surface tension of a drop, *Journal of Chemical Physics* 96 (1991) 565–576.
- [124] J. A. van Meel, A. J. Page, R. P. Sear, D. Frenkel: Two-step vapor-crystal nucleation close below triple point, *Journal of Chemical Physics* 129 (2008) 204505.
- [125] I. Napari, J. Julin, H. Vehkamäki: Performance of some nucleation theories with a nonsharp droplet-vapor interface, *Journal of Chemical Physics* 133 (2010) 154503.
- [126] P. G. Bolhuis, D. Chandler: Transition path sampling of cavitation between molecular scale solvophobic surfaces, *Journal of Chemical Physics* 113 (2000) 8154–8160.
- [127] S. Toxvaerd: Molecular dynamics simulation of prewetting, *Journal of Physical Chemistry C* 111 (2007) 15620–15624.
- [128] T. Bieker, S. Dietrich: Wetting of curved surfaces, *Physica A* 252 (1998) 85–137. Erratum: *Physica A* 259(3–4): 466–467 (1998).
- [129] D. Zhou, M. Zeng, J. Mi, C. Zhong: Theoretical study of phase transition, surface tension, and nucleation rate predictions for argon, *Journal of Physical Chemistry B* 115 (2011) 57–63.

- [130] H. Yaguchi, T. Yano, S. Fujikawa: Molecular dynamics study of vapor-liquid equilibrium state of an argon nanodroplet and its vapor, *Journal of Fluid Science and Technology* 5 (2010) 180–191.
- [131] S. J. Hemingway, J. R. Henderson, J. S. Rowlinson: The density profile and surface tension of a drop, *Faraday Symposia of the Chemical Society* 16 (1981) 33–43.
- [132] P. Bryk, R. Roth, K. R. Mecke, S. Dietrich: Hard-sphere fluids in contact with curved substrates, *Physical Review E* 68 (2003) 031602.
- [133] K. Koga, X. C. Zeng, A. K. Shchekin: Validity of Tolman’s equation: How large should a droplet be?, *Journal of Chemical Physics* 109 (1998) 4063–4070.
- [134] J. Julin, I. Napari, J. Merikanto, H. Vehkamäki: A thermodynamically consistent determination of surface tension of small Lennard-Jones clusters from simulation and theory, *Journal of Chemical Physics* 133 (2010) 044704.
- [135] M. Mareschal, M. Baus, R. Lovett: The local pressure in a cylindrical liquid-vapor interface: A simulation study, *Journal of Chemical Physics* 106 (1997) 645–654.
- [136] M. J. Haye, C. Bruin: Molecular dynamics study of the curvature correction to the surface tension, *Journal of Chemical Physics* 100 (1994) 556–559.
- [137] S. Maruyama, S. Matsumoto, M. Shoji, A. Ogita: A molecular dynamics study of interface phenomena of a liquid droplet, in: G. F. Hewitt (Ed.), *Proc. X. International Heat Transfer Conference*, volume 2, Institute of Chemical Engineers, Rugby, England, 1994, pp. 409–414.
- [138] S. Werth, S. V. Lishchuk, M. Horsch, H. Hasse: The influence of the liquid slab thickness on the planar vapor-liquid interfacial tension, *Physica A* 392 (2013) 2359–2367.
- [139] A. Tröster, M. Oettel, B. Block, P. Virnau, K. Binder: Numerical approaches to determine the interface tension of curved interfaces from free energy calculations, *Journal of Chemical Physics* 136 (2012) 064709.
- [140] R. Lovett: Describing phase coexistence in systems with small phases, *Reports on Progress in Physics* 70 (2007) 195–218.
- [141] G. Chkonia, J. Wölk, R. Strey, J. Wedekind, D. Reguera: Evaluating nucleation rates in direct simulations, *Journal of Chemical Physics* 130 (2009) 064505.
- [142] T. S. van Erp, D. Moroni, P. G. Bolhuis: A novel path sampling method for the calculation of rate constants, *Journal of Chemical Physics* 118 (2003) 7762–7774.

- [143] D. J. McGinty: Molecular dynamics studies of the properties of small clusters of argon atoms, *Journal of Chemical Physics* 58 (1973) 4733–4742.
- [144] J. Janeček: Effect of the interfacial area on the equilibrium properties of Lennard-Jones fluid, *Journal of Chemical Physics* 131 (2009) 124513.
- [145] J. V. Sengers, J. M. J. van Leeuwen: Capillary waves of a vapor-liquid interface near the critical temperature, *Physical Review A* 39 (1989) 6346–6355.
- [146] J.-G. Weng, S. Park, J. R. Lukes, C.-L. Tien: Molecular dynamics investigation of thickness effect on liquid films, *Journal of Chemical Physics* 113 (2000) 5917–5923.
- [147] Y. Hamada, K. Koga, H. Tanaka: Phase behavior and fluid-solid surface tension of argon in slit pores and carbon nanotubes, *Physica A* 388 (2009) 2289–2298.
- [148] H. Watanabe, N. Ito, C.-K. Hu: Phase diagram and universality of the Lennard-Jones gas-liquid system, *Journal of Chemical Physics* 136 (2012) 204102.
- [149] T. W. Lion, R. J. Allen: Computing the local pressure in molecular dynamics simulations, *Journal of Physics: Condensed Matter* 24 (2012) 284133.
- [150] T. Kraska, F. Römer, A. Imre: The relation of interface properties and bulk phase stability, *Journal of Physical Chemistry B* 113 (2009) 4688–4697.
- [151] J. Alejandre, G. A. Chapela: The surface tension of TIP4P/2005 water model using the Ewald sums for the dispersion interactions, *Journal of Chemical Physics* 132 (2010) 014701.
- [152] D. Fincham: Leapfrog rotational algorithms, *Molecular Simulation* 8 (1992) 165–178.
- [153] J. Pérez Pellitero, P. Ungerer, G. Orkoulas, A. D. Mackie: Critical point estimation of the Lennard-Jones pure fluid and binary mixtures, *Journal of Chemical Physics* 125 (2006) 054515.
- [154] C. D. Holcomb, P. Clancy, J. A. Zollweg: A critical study of the simulation of the liquid-vapour interface of a Lennard-Jones fluid, *Molecular Physics* 78 (1993) 437–459.
- [155] J. J. Potoff, A. Z. Panagiotopoulos: Surface tension of the three-dimensional Lennard-Jones fluid from histogram-reweighting Monte Carlo simulations, *Journal of Chemical Physics* 112 (2000) 6411–6415.
- [156] J. López Lemus, J. Alejandre: Thermodynamic and transport properties of simple fluids using lattice sums: bulk phases and liquid-vapour interface, *Molecular Physics* 100 (2002) 2983–2992.

- [157] J. Vrabec, J. Stoll, H. Hasse: A set of molecular models for symmetric quadrupolar fluids, *Journal of Physical Chemistry B* 105 (2001) 12126–12133.
- [158] A. Malijevský, G. Jackson: A perspective on the interfacial properties of nanoscopic liquid drops, *Journal of Physics: Condensed Matter* 24 (2012) 464121.
- [159] P. G. Debenedetti: *Metastable Liquids – Concepts and Principles*, Princeton University Press, 1996.
- [160] M. T. Horsch, S. K. Miroshnichenko, J. Vrabec, C. W. Glass, C. Niethammer, M. F. Bernreuther, E. A. Müller, G. Jackson: Static and dynamic properties of curved vapour-liquid interfaces by massively parallel molecular dynamics simulation, in: C. Bischof, H.-G. Hegering, W. E. Nagel, G. Wittum (Eds.), *Competence in High Performance Computing*, Springer, Berlin – Heidelberg, 2012, pp. 73–84.
- [161] M. P. A. Fisher, M. Wortis: Curvature corrections to the surface tension of fluid drops: Landau theory and a scaling hypothesis, *Physical Review B* 29 (1984) 6252–6260.
- [162] D. Reguera, R. K. Bowles, Y. Djikaev, H. Reiss: Phase transitions in systems small enough to be clusters, *Journal of Chemical Physics* 118 (2003) 340–353.
- [163] S. Eichelbaum, G. Scheuermann, M. Hlawitschka: PointAO – Improved ambient occlusion for point-based visualization, in: *Proceedings of the Eurographics Conference on Visualization (EuroVis)*, Eurographics Association, 2013, p. SP148.
- [164] A. Tröster, K. Binder: Positive Tolman length in a lattice gas with three-body interactions, *Physical Review Letters* 107 (2011).
- [165] S. Becker, H. M. Urbassek, M. Horsch, H. Hasse: Contact angle of sessile drops in Lennard-Jones systems, *Langmuir* 30 (2014) 13606–13614.
- [166] J. H. Sikkenk, J. O. Indekeu, J. M. J. van Leeuwen, E. O. Vossnack: Molecular-dynamics simulation of wetting and drying at solid-fluid interfaces, *Physical Review Letters* 59 (1987) 98–101.
- [167] M. Nijmeijer, C. Bruin, A. Bakker, J. van Leeuwen: A visual measurement of contact angles in a molecular-dynamics simulation, *Physica A* 160 (1989) 166–180.
- [168] M. Nijmeijer, C. Bruin, A. Bakker, J. van Leeuwen: Molecular dynamics of the wetting and drying of a wall with a long-ranged wall-fluid interaction, *Journal of Physics: Condensed Matter* 4 (1992) 15–31.
- [169] T. D. Blake, A. Clarke, J. De Coninck, M. J. de Ruijter: Contact angle relaxation during droplet spreading: Comparison between molecular kinetic theory and molecular dynamics, *Langmuir* 13 (1997) 2164–2166.

- [170] T. Werder, J. H. Walther, R. L. Jaffe, T. Halicioğlu, P. Koumoutsakos: On the water-carbon interaction for use in molecular dynamics simulations of graphite and carbon nanotubes, *Journal of Physical Chemistry B* 107 (2003) 1345–1352.
- [171] E. M. Grzelak, V. K. Shen, J. R. Errington: Molecular simulation study of anisotropic wetting, *Langmuir* 26 (2010) 8274–8281.
- [172] K. S. Rane, V. Kumar, J. R. Errington: Monte Carlo simulation methods for computing the wetting and drying properties of model systems, *Journal of Chemical Physics* 135 (2011) 234102.
- [173] J. H. Weijs, A. Marchand, B. Andreotti, D. Lohse, J. H. Snoeijer: Origin of line tension for a Lennard-Jones nanodroplet, *Physics of Fluids* 23 (2011) 022001.
- [174] M. J. P. Nijmeijer, C. Bruin, A. F. Bakker, J. M. J. van Leeuwen: Wetting and drying of an inert wall by a fluid in a molecular-dynamics simulation, *Physical Review A* 42 (1990) 6052–6059.
- [175] J. Z. Tang, J. G. Harris: Fluid wetting on molecularly rough surfaces, *Journal of Chemical Physics* 103 (1995) 8201–8208.
- [176] T. Ingebrigtsen, S. Toxvaerd: Contact angles of Lennard-Jones liquids and droplets on planar surfaces, *Journal of Physical Chemistry C* 111 (2007) 8518–8523.
- [177] A. Oleinikova, I. Brovchenko, A. Geiger: Behavior of a wetting phase near a solid boundary: Vapor near a weakly attractive surface, *European Physics Journal B* 52 (2006) 507–519.
- [178] J. H. Sikkenk, J. O. Indekeu, J. M. J. van Leeuwen, E. O. Vossnack, A. F. Bakker: Simulation of wetting and drying at solid-fluid interfaces on the Delft molecular dynamics processor, *Journal of Statistical Physics* 52 (1988) 23–44.
- [179] W. Humphrey, A. Dalke, K. Schulten: VMD – Visual molecular dynamics, *Journal of Molecular Graphics* 14 (1996) 33–38.
- [180] M. Horsch, M. Heitzig, C. Dan, J. Harting, H. Hasse, J. Vrabec: Contact angle dependence on the fluid–wall dispersive energy, *Langmuir* 26 (2010) 10913–10917.
- [181] P. A. Monson: Contact angles, pore condensation, and hysteresis: Insights from a simple molecular model, *Langmuir* 24 (2008) 12295–12302.
- [182] A. Shahraz, A. Borhan, K. A. Fichthorn: A theory for the morphological dependence of wetting on a physically patterned solid surface, *Langmuir* 28 (2012) 14227–14237.

- [183] J. M. Castillo, M. Klos, K. Jacobs, M. Horsch, H. Hasse: Characterization of alkylsilane self-assembled monolayers by molecular simulation, *Langmuir* 31 (2015) 2630–2638.
- [184] W. C. Bigelow, D. L. Pickett, W. A. Zisman: Oleophobic monolayers. 1. Films adsorbed from solution in non-polar liquids, *Journal of Colloid Science* 1 (1946) 513–538.
- [185] M. Lessel, O. Bäumchen, M. Klos, H. Hähl, R. Fetzer, M. Paulus, R. Seemann, K. Jacobs: Self-assembled silane monolayers: An efficient step-by-step recipe for high-quality, low energy surfaces, *Surface and Interface Analysis* 47 (2015) 557–564.
- [186] F. Eisert, M. Gurka, A. Legant, M. Buck, M. Grunze: Detection of molecular alignment in confined films, *Science* 287 (2000) 468–470.
- [187] M. K. Chaudhury, G. M. Whitesides: Correlation between surface free-energy and surface constitution, *Science* 255 (1992) 1230–1232.
- [188] P. Gutfreund, O. Baeumchen, R. Fetzer, D. van der Grinten, M. Maccarini, K. Jacobs, H. Zabel, M. Wolff: Solid surface structure affects liquid order at the polystyrene-self-assembled-monolayer interface, *Physical Review E* 87 (2013) 012306.
- [189] J. Barriga, B. Coto, B. Fernández: Molecular dynamics study of optimal packing structure of OTS self-assembled monolayers on SiO₂ surfaces, *Tribology International* 40 (2007) 960–966.
- [190] D. J. Barlow, A. M. Muslim, J. R. P. Webster, J. Penfold, C. M. Hollinshead, M. J. Lawrence: Molecular modelling of surfactant monolayers under constraints derived from neutron reflectance measurements, *Physical Chemistry Chemical Physics* 2 (2000) 5208–5213.
- [191] S. Pronk, P. Szilárd, R. Schulz, P. Larsson, P. Bjelkmar, R. Apostolov, M. R. Shirts, J. C. Smith, P. M. Kasson, D. van der Spoel, B. Hess, E. Lindahl: GROMACS 4.5: A high-throughput and highly parallel open source molecular simulation toolkit, *Bioinformatics* 29 (2013) 845–854.
- [192] K. Kojio, S. R. Ge, A. Takahara, T. Kajiyama: Molecular aggregation state of n-octadecyltrichlorosilane monolayer prepared at an air/water interface, *Langmuir* 14 (1998) 971–974.
- [193] W. L. Jorgensen, D. S. Maxwell, J. Tirado Rives: Development and testing of the OPLS all-atom force field on conformational energetics and properties of organic liquids, *Journal of the American Chemical Society* 118 (1996) 11225–11236.

- [194] C. D. Lorenz, E. B. Webb, M. J. Stevens, M. Chandross, G. S. Grest: Frictional dynamics of perfluorinated self-assembled monolayers on amorphous SiO₂, *Tribology Letters* 19 (2005) 93–99.
- [195] Z. Kong, Q. Wang, E. Chen, T. Wu: Study on preparation method for short-chain alkylsiloxane self-assembled monolayers and the diffusion behavior of copper on silica surfaces, *Applied Surface Science* 279 (2013) 171–179.
- [196] M. R. Linford, P. Fenter, P. M. Eisenberger, C. E. D. Chidsey: Alkyl monolayers on silicon prepared from 1-alkenes and hydrogen-terminated silicon, *Journal of the American Chemical Society* 117 (1995) 3145–3155.
- [197] A. M. Cione, O. A. Mazyar, B. D. Booth, C. McCabe, G. K. Jennings: Deposition and wettability of [bmim][triflate] on self-assembled monolayers, *Journal of Physical Chemistry C* 113 (2009) 2384–2392.
- [198] B. D. Booth, S. G. Vilt, J. Ben Lewis, J. L. Rivera, E. A. Buehler, C. McCabe, G. K. Jennings: Tribological durability of silane monolayers on silicon, *Langmuir* 27 (2011) 5909–5917.
- [199] I. M. Tidswell, T. A. Rabedeau, P. S. Pershan, S. D. Kosowsky, J. P. Folkers, G. M. Whitesides: X-ray grazing-incidence diffraction from alkylsiloxane monolayers on silicon-wafers, *Journal of Chemical Physics* 95 (1991) 2854–2861.
- [200] F. Schreiber: Structure and growth of self-assembling monolayers, *Progress in Surface Science* 65 (2000) 151–256.
- [201] K. Bierbaum, M. Grunze, A. A. Baski, L. F. Chi, W. Schrepp, H. Fuchs: Growth of self-assembled n-alkyltrichlorosilane films on Si(100) investigated by atomic-force microscopy, *Langmuir* 11 (1995) 2143–2150.
- [202] T. Vallant, J. Kattner, H. Brunner, U. Mayer, H. Hoffmann: Investigation of the formation and structure of self-assembled alkylsiloxane monolayers on silicon using in situ attenuated total reflection infrared spectroscopy, *Langmuir* 15 (1999) 5339–5346.
- [203] N. Tillman, A. Ulman, J. S. Schildkraut, T. L. Penner: Incorporation of phenoxy groups in self-assembled monolayers of trichlorosilane derivatives – effects on film thickness, wettability, and molecular-orientation, *Journal of the American Chemical Society* 110 (1988) 6136–6144.
- [204] A. P. Kaushik, P. Clancy: Trapping dynamics of diindenoperylene (DIP) in self-assembled monolayers using molecular simulation, *Surface Science* 605 (2011) 1185–1196.

- [205] C. Niethammer, S. Becker, M. Bernreuther, M. Buchholz, W. Eckhardt, A. Heinecke, S. Werth, H.-J. Bungartz, C. W. Glass, H. Hasse, J. Vrabec, M. Horsch: ls1 mardyn: The massively parallel molecular dynamics code for large systems, *Journal of Chemical Theory and Computation* 10 (2014) 4455–4464.
- [206] D. A. Case, T. E. Cheatham, III, T. Darden, H. Gohlke, R. Luo, K. M. Merz, jr., A. Onufriev, C. Simmerling, B. Wang, R. Woods: The Amber biomolecular simulation programs, *Journal of Computational Chemistry* 26 (2005) 1668–1688.
- [207] P. Ren, C. Wu, J. W. Ponder: Polarizable atomic multipole-based molecular mechanics for organic molecules, *Journal of Chemical Theory and Computation* 7 (2011) 3143–3461.
- [208] B. R. Brooks, C. L. Brooks (III.), A. D. Mackerell (jr.), L. Nilsson, R. J. Petrella, B. Roux, Y. Won, G. Archontis, C. Bartels, S. Boresch, A. Caffisch, L. Caves, Q. Cui, A. R. Dinner, M. Feig, S. Fischer, J. Gao, M. Hodoscek, W. Im, K. Kuczera, T. Lazaridis, J. Ma, V. Ovchinnikov, E. Paci, R. W. Pastor, C. B. Post, J. Z. Pu, M. Schaefer, B. Tidor, R. M. Venable, H. L. Woodcock, X. Wu, W. Yang, D. M. York, M. Karplus: CHARMM: The biomolecular simulation program, *Journal of Computational Chemistry* 30 (2009) 1545–1614.
- [209] S. J. Plimpton, A. P. Thompson: Computational aspects of many-body potentials, *MRS Bulletin* 37 (2012) 513–521.
- [210] C. G. Gray, K. E. Gubbins: *Theory of Molecular Fluids, volume 1: Fundamentals*, Oxford University Press, 1984.
- [211] J. Tersoff: Empiric interatomic potential for carbon, with applications to amorphous carbon, *Physical Review Letters* 61 (1988) 2879–2882.
- [212] L. M. Ghiringhelli, C. Valeriani, J. H. Los, E. J. Meijer, A. Fasolino, D. Frenkel: State-of-the-art models for the phase diagram of carbon and diamond nucleation, *Molecular Physics* 106 (2008) 2011–2038.
- [213] M. Buchholz: *Framework zur Parallelisierung von Molekulardynamiksimulationen in verfahrenstechnischen Anwendungen*, Dissertation, Technische Universität München, 2010.
- [214] P.-E. Bernard, T. Gautier, D. Trystram: Large scale simulation of parallel molecular dynamics, in: R. Sitaraman (Ed.), *13th International Parallel Processing Symposium and 10th Symposium on Parallel and Distributed Processing*, IEEE Computer Society, Los Alamitos, CA, USA, 1999, pp. 638–644.

- [215] W. Eckhardt, A. Heinecke, R. Bader, M. Brehm, N. Hammer, H. Huber, H.-G. Kleinhenz, J. Vrabec, H. Hasse, M. Horsch, M. Bernreuther, C. W. Glass, C. Niethammer, A. Bode, J. Bungartz: 591 TFLOPS multi-trillion particles simulation on SuperMUC, in: *Supercomputing – 28th International Supercomputing Conference (ISC 2013)*, number 7905 in *Lecture Notes in Computer Science*, Springer, Heidelberg, 2013, pp. 1–12.
- [216] W. Eckhardt, T. Neckel: Memory-efficient implementation of a rigid-body molecular dynamics simulation, in: *Proceedings of the XI. International Symposium on Parallel and Distributed Computing – ISPDC 2012*, IEEE, München, 2012, pp. 103–110.
- [217] K. Kadau, T. C. Germann, P. S. Lomdahl: Molecular dynamics comes of age: 320 billion atom simulation on BlueGene/L, *International Journal of Modern Physics C* 17 (2006) 1755–1761.
- [218] T. C. Germann, K. Kadau: Trillion-atom molecular dynamics becomes a reality, *International Journal of Modern Physics C* 19 (2008) 1315–1319.
- [219] I. Kabadshow, H. Dachsel, J. Hammond: Passing the three trillion particle limit with an error-controlled fast multipole method, in: *Companion on High Performance Computing Networking, Storage and Analysis*, ACM, New York, 2011, pp. 73–74.
- [220] W. Eckhardt, A. Heinecke: An efficient vectorization of linked-cell particle simulations, in: *ACM International Conference on Computing Frontiers*, Cagliari, 2012, pp. 241–243.
- [221] E. Lindahl, B. Hess, D. van der Spoel: GROMACS 3.0: A package for molecular simulation and trajectory analysis, *Journal of Molecular Modeling* 7 (2001) 306–317.
- [222] L. Peng, M. Kunaseth, H. Dursun, K.-i. Nomura, W. Wang, R. Kalia, A. Nakano, P. Vashishta: Exploiting hierarchical parallelisms for molecular dynamics simulation on multicore clusters, *Journal of Supercomputing* 57 (2011) 20–33.
- [223] D. C. Rapaport: Multibillion-atom molecular dynamics simulation: Design considerations for vector-parallel processing, *Computer Physics Communications* 174 (2006) 521–529.
- [224] C. W. Glass, S. Reiser, G. Rutkai, S. Deublein, A. Köster, G. Guevara Carrión, A. Wafai, M. Horsch, M. Bernreuther, T. Windmann, H. Hasse, J. Vrabec: ms2: A molecular simulation tool for thermodynamic properties, new version release, *Computer Physics Communications* 185 (2014) 3302–3306.

- [225] S. Reiser, M. Horsch, H. Hasse: Temperature dependence of the density of aqueous alkali halide salt solutions by experiment and molecular simulation, *Journal of Chemical & Engineering Data* 59 (2014) 3434–3448.
- [226] G. Rutkai, M. Thol, R. Lustig, R. Span, J. Vrabec: Fundamental equation of state correlation with hybrid data sets, *Journal of Chemical Physics* 139 (2013) 041102.
- [227] H. W. Graben, J. R. Ray: Eight physical systems of thermodynamics, statistical mechanics, and computer simulations, *Molecular Physics* 50 (1993) 1183–1193.
- [228] R. Lustig: Statistical analogues for fundamental equation of state derivatives, *Molecular Physics* 110 (2012) 3041–3052.
- [229] R. Lustig: Statistical thermodynamics in the classical molecular dynamics ensemble. II. Application to computer simulation, *Journal of Chemical Physics* 100 (1994) 3060–3067.
- [230] R. Kubo: The fluctuation-dissipation theorem, *Reports on Progress in Physics* 29 (1966) 255–284.
- [231] J. P. Hansen, I. R. McDonald: *Theory of Simple Liquids*, Academic, New York, 1986.
- [232] S. Reiser, S. Deublein, J. Vrabec, H. Hasse: Molecular dispersion energy parameters for alkali and halide ions in aqueous solution, *Journal of Chemical Physics* 140 (2014) 044504.
- [233] S. Deublein, J. Vrabec, H. Hasse: A set of molecular models for alkali and halide ions in aqueous solution, *Journal of Chemical Physics* 136 (2012) 084501.
- [234] H. J. C. Berendsen, J. R. Grigera, T. P. Straatsma: The missing term in effective pair potentials, *Journal of Physical Chemistry* 91 (1987) 6269–6271.
- [235] F. Moucka, I. Nezbeda, W. R. Smith: Molecular force fields for aqueous electrolytes: SPC/E-compatible charged LJ sphere models and their limitations, *Journal of Chemical Physics* 138 (2013) 154102.
- [236] D. E. Smith, L. X. Dang: Computer simulations of NaCl association in polarizable water, *Journal of Chemical Physics* 100 (1994) 3757–3766.
- [237] V. M. Lobo: *Electrolyte Solutions: Literature Data on Thermodynamic and Transport Properties*, volume 1, University of Coimbra, Portugal, 1984.
- [238] D. J. Evans, W. B. Streett: Transport properties of homonuclear diatomics. 2. Dense fluids, *Molecular Physics* 36 (1978) 161–176.

- [239] M. Horsch, H. Hasse: Molecular modelling and simulation in fluid process engineering, *ChemBioEng Reviews* 2 (2015) 303–310.
- [240] V. Kumar, S. Sridhar, J. D. Errington: Monte Carlo simulation strategies for computing the wetting properties of fluids at geometrically rough surfaces, *Journal of Chemical Physics* 135 (2011) 184702.
- [241] J. S. Rowlinson, B. Widom: *Molecular Theory of Capillarity*, Clarendon, Oxford, 1982.
- [242] S. Kjelstrup, D. Bedeaux, E. Johannessen, J. Groß: *Non-Equilibrium Thermodynamics for Engineers*, World Scientific, Singapore, 2010.
- [243] G. Karniadakis, A. Beskok, N. Aluru: *Microflows and Nanoflows: Fundamentals and Simulation*, Springer, New York, 2005.
- [244] H. Frentrup, C. Avendaño, M. Horsch, A. Salih, E. A. Müller: Transport diffusivities of fluids in nanopores by non-equilibrium molecular dynamics simulation, *Molecular Simulation* 38 (2012) 540–553.
- [245] J. Kärger, D. M. Ruthven, D. N. Theodorou: *Diffusion in Nanoporous Materials*, Wiley-VCH, Weinheim, 2012.
- [246] M. Horsch, J. Vrabec: Grand canonical steady-state simulation of nucleation, *Journal of Chemical Physics* 131 (2009) 184104.
- [247] D. Wales: *Energy Landscapes: Applications to Clusters, Biomolecules and Glasses*, Cambridge University Press, 2004.
- [248] P. L. Freddolino, C. B. Harrison, Y. Liu, K. Schulten: Challenges in protein-folding simulations, *Nature Physics* 6 (2010) 751–758.
- [249] Z. Ható, Á. Kaviczki, T. Kristóf: A simple method for the simulation of steady-state diffusion through membranes: Pressure-tuned, boundary driven molecular dynamics, *Molecular Simulation* 42 (2016) 71–80.

Statement on authorship

This habilitation thesis contains material that has previously been published. In the following, these publications are listed together with a statement clarifying the contributions of the present author:

- M. Horsch, H. Hasse, A. K. Shchekin, A. Agarwal, S. Eckelsbach, J. Vrabec, E. A. Müller, G. Jackson: Excess equimolar radius of liquid drops, *Physical Review E* 85 (2012) 031605, used for Sections 1.3 and 2.1.

The theoretical results presented in this publication were obtained by M. Horsch and J. Vrabec. The molecular simulations were carried out by A. Agarwal and M. Horsch and analysed by M. Horsch with scientific supervision by G. Jackson and E. A. Müller. Following discussions between the co-authors, the text of the article was drafted by M. Horsch and revised by H. Hasse, G. Jackson, E. A. Müller, and J. Vrabec. Corresponding author: M. Horsch.

- W. Eckhardt, A. Heinecke, R. Bader, M. Brehm, N. Hammer, H. Huber, H.-G. Kleinhenz, J. Vrabec, H. Hasse, M. Horsch, M. F. Bernreuther, C. W. Glass, C. Niethammer, A. Bode, H.-J. Bungartz: 591 TFLOPS multi-trillion particles simulation on SuperMUC, in J. M. Kunkel, T. Ludwig, H. W. Meuer (eds.): *Supercomputing – Proceedings of the XXVIII. International Supercomputing Conference (ISC 2013)*, Lecture Notes in Computer Science 7905, Springer: Heidelberg (2013) 1–12, used for Section 4.2.

The software modifications discussed in this publications were implemented by W. Eckhardt and A. Heinecke, as a contribution to a software development project coordinated by M. Horsch. The molecular simulations were carried out and analysed by W. Eckhardt and A. Heinecke with scientific supervision by H.-J. Bungartz. Following discussions between the co-authors, the text of the article was drafted by W. Eckhardt and revised by H.-J. Bungartz, M. Horsch, and J. Vrabec. Corresponding author: H.-J. Bungartz.

- M. Horsch, C. Niethammer, J. Vrabec, H. Hasse: Computational molecular engineering as an emerging technology in process engineering, *Information Technology* 55 (2013) 97–101, used for Sections 1.1 and 4.1.

Following discussions between the co-authors, the text of this article was drafted by M. Horsch and revised by H. Hasse. Corresponding author: M. Horsch.

- S. Werth, S. V. Lishchuk, M. Horsch, H. Hasse: The influence of the liquid slab thickness on the planar vapor-liquid interfacial tension, *Physica A* 392 (2013) 2359–2367, used for Section 2.2.

The molecular simulations discussed in this publication were conducted and analysed by S. Werth with scientific supervision by H. Hasse and M. Horsch. Following discus-

sions between the co-authors, the text of the article was drafted by S. Werth and revised by H. Hasse and M. Horsch. Corresponding author: M. Horsch.

- S. Becker, H. M. Urbassek, M. Horsch, H. Hasse: Contact angle of sessile drops in Lennard-Jones systems, *Langmuir* 30 (2014) 13606–13614, used for Section 3.1.

The molecular simulations discussed in this publication were conducted and analysed by S. Becker with scientific supervision by H. Hasse and M. Horsch. Following discussions between the co-authors, the text of the article was drafted by S. Becker and revised by H. Hasse and M. Horsch. Corresponding author: M. Horsch.

- C. W. Glass, S. Reiser, G. Rutkai, S. Deublein, A. Köster, G. Guevara Carrión, A. Wafai, M. Horsch, M. Bernreuther, T. Windmann, H. Hasse, J. Vrabec: ms2 – A molecular simulation tool for thermodynamic properties, new version release, *Computer Physics Communications* 185 (2014) 3302–3306, used for Section 4.3.

The software presented in this publication was developed by a team of over twenty persons coordinated by J. Vrabec. Following discussions between the co-authors, the text of the article was drafted by C. W. Glass and G. Rutkai and revised by H. Hasse, M. Horsch, and J. Vrabec. Corresponding author: J. Vrabec.

- M. Horsch, H. Hasse: Molecular simulation of nano-dispersed fluid phases, *Chemical Engineering Science* 107 (2014) 235–244, used for Sections 1.3 and 2.3.

The molecular simulations discussed in this publication were conducted by A. Bedhotiya and M. Horsch and evaluated by M. Horsch. Following discussions between the co-authors, the text of the article was drafted by M. Horsch and revised by H. Hasse. Corresponding author: M. Horsch.

- C. Niethammer, S. Becker, M. Bernreuther, M. Buchholz, W. Eckhardt, A. Heinecke, S. Werth, H.-J. Bungartz, C. W. Glass, H. Hasse, J. Vrabec, M. Horsch: ls1 mardyn – The massively parallel molecular dynamics code for large systems, *Journal of Chemical Theory and Computation* 10 (2014) 4455–4464, used for Section 4.1.

The software presented in this publication was developed by a team of over twenty persons coordinated by M. Horsch. Following discussions between the co-authors, a first draft of the article was written by M. Buchholz. A second draft was written by C. Niethammer and revised by H.-J. Bungartz, W. Eckhardt, C. W. Glass, H. Hasse, M. Horsch, and J. Vrabec. Corresponding author: M. Horsch.

- S. Reiser, M. Horsch, H. Hasse: Temperature dependence of the density of aqueous alkali halide salt solutions by experiment and molecular simulation, *Journal of Chemical & Engineering Data* 59 (2014) 3434–3448, used for Section 4.3.

The experiments and molecular simulations discussed in this publication were conducted and analysed by S. Reiser with scientific supervision by H. Hasse and M. Horsch.

Following discussions between the co-authors, the text of the article was drafted by S. Reiser and revised by H. Hasse and M. Horsch. Corresponding author: M. Horsch.

- S. Werth, G. Rutkai, J. Vrabec, M. Horsch, H. Hasse: Long-range correction for multi-site LJ models and planar interfaces, *Molecular Physics* 112 (2014) 2227–2234, used for Section 1.4.

The theoretical results presented in this publication were obtained by S. Werth. The molecular simulations were carried out and analysed by S. Werth with scientific supervision by H. Hasse and M. Horsch. Following discussions between the co-authors, the text of the article was drafted by S. Werth and revised by H. Hasse, M. Horsch, and J. Vrabec. Corresponding author: M. Horsch.

- J. M. Castillo, M. Klos, K. Jacobs, M. Horsch, H. Hasse: Characterization of alkylsilane self-assembled monolayers by molecular simulation, *Langmuir* 31 (2015) 2630–2638, used for Section 3.2.

The molecular simulations discussed in this publication were conducted and analysed by J. M. Castillo with scientific supervision by H. Hasse and M. Horsch. Following discussions between the co-authors, the text of the article was drafted by J. M. Castillo and revised by H. Hasse, M. Horsch, and K. Jacobs. Corresponding author: M. Horsch.

- M. Horsch, H. Hasse: Molecular modelling and simulation in fluid process engineering, *ChemBioEng Reviews* 2 (2015) 303–310, used for the Abstract and Chapter 5.

Following discussions between the co-authors, a first draft of the article (in German) was written by M. Horsch, revised by H. Hasse, and accepted for publication by *Chemie Ingenieur Technik (Molekulare Modellierung und Simulation in der Fluidverfahrenstechnik)*, see below. Following a request from *ChemBioEng Reviews*, the article was translated by M. Horsch and resubmitted. Corresponding author: M. Horsch.

Curriculum vitae

Name	Martin Thomas Horsch
Date of birth	13th August 1982 in Stuttgart
Nationality	German

Academic career	
Interval	1st April 2011 – present
Institution	University of Kaiserslautern Laboratory of Engineering Thermodynamics
Position	Head of Group, Computational Molecular Engineering Junior Professor (since 15th June 2011)
Interval	1st October 2010 – 31st March 2011
Institution	Imperial College London Department of Chemical Engineering
Position	DAAD Research Fellow
Qualification	
Date	10th September 2010
Institution	University of Paderborn
Degree	Doktor-Ingenieur (Dr.-Ing.)
Grade	1,0 – mit Auszeichnung (summa cum laude)
Date	13th July 2006
Institution	University of Stuttgart
Degree	Diplom-Informatiker (Dipl.-Inf.)
Grade	1,0 – mit Auszeichnung (summa cum laude)
Date	27th June 2000
Institution	Karls gymnasium Stuttgart
Degree	Abitur
Grade	1,0 – sehr gut (summa cum laude)

ISSN 2195-7606
ISBN 978-3-944433-18-9